Inkjet Printed Radio Frequency Passive Components

Dissertation/Thesis by

Garret McKerricher

In Partial Fulfillment of the Requirements

For the Degree of

Doctor of Philosophy/ Master of Science

King Abdullah University of Science and Technology

Thuwal, Kingdom of Saudi Arabia

December 2015

EXAMINATION COMMITTEE APPROVALS FORM

The dissertation/thesis of Garret McKerricher is approved by the examination committee.

Committee Chairperson [Atif Shamim]

Committee Member [Husam Alshareef]

Committee Member [Jurgen Kosel]

Committee Member [Vivek Subramanian]

3

ABSTRACT

Inkjet Printed Radio Frequency Passive Components

Garret McKerricher

Inkjet printing is a mature technique for colourful graphic arts. It excels at customized, large area, high resolution, and small volume production. With the developments in conductive, and dielectric inks, there is potential for large area inkjet electronics fabrication. Passive radio frequency devices can benefit greatly from a printing process, since the size of these devices is defined by the frequency of operation. The large size of radio frequency passives means that they either take up expensive space "on chip" or that they are fabricated on a separate lower cost substrate and somehow bonded to the chips. This has hindered cost-sensitive high volume applications such as radio frequency identification tags. Substantial work has been undertaken on inkjet-printed conductors for passive antennas on microwave substrates and even paper, yet there has been little work on the printing of the dielectric materials aimed at radio frequency passives. Both the conductor and dielectric need to be integrated to create a multilayer inkjet printing process that is capable of making quality passives such as capacitors and inductors.

Three inkjet printed dielectrics are investigated in this thesis: a ceramic (alumina), a thermal-cured polymer (poly 4 vinyl phenol), and a UV-cured polymer (acrylic based). For the conductor, both a silver nanoparticle ink as well as a custom in-house formulated particle-free silver ink are explored. The focus is on passives, mainly capacitors and inductors. Compared to low frequency electronics, radio frequency components have additional sensitivity regarding skin depth of the conductor and surface roughness, as

well as dielectric constant and loss tangent of the dielectric. These concerns are

investigated with the aim of making the highest quality components possible and to

understand the current limitations of inkjet-fabricated radio frequency devices. An inkjet-

printed alumina dielectric that provides quality factors of 200 and high density

capacitors of 400 pF/mm^2 with self-resonant frequencies into the GHz regime is

developed in this thesis. A multilayer fully printed process is demonstrated using PVP

dielectric and dissolving type vias, giving better than 0.1 ohm resistance. In the

multilayer process, capacitors and inductors have self-resonant frequencies around

1GHz. These fully printed devices have quality factors less than 10. Finally, 3D inkjet-

printed UV-cured material is utilized with a novel silver organo-complex ink at 80°C

providing conductivity of 1x10^7 S/m. A lumped element filter is demonstrated with an

insertion loss of only 0.8 dB at 1GHz. The combination of inkjet printing 3D polymer and

conductive metal together allows for complex shapes. A fully printed antenna with 81%

radiation efficiency is shown. With these promising results and future advances in

conductive inks and low-loss dielectrics, the performance of inkjet passives could one day

overcome conventional fabrication methods.

ACKNOWLEDGEMENTS

TABLE OF CONTENTS

LIST OF ABBREVIATIONS

AFM	Atomic Force Microscopy
ALD	Atomic Layer Deposition
AOC	Silver-Organocomplex
a-Si	Amorphous Silicon
Dk	Dielectric Constant
Df	Dissipation factor
E-Beam	Electron Beam
EDX	Energy Dispersive X-Ray Spectroscopy
EM	Electromagnetic
IR	Infrared
MIM	Metal Insulator Metal
MSDS	Material Safety Data Sheet
PVP	Poly (4-vinyl phenol)
PZT	Lead (Pb) Zirconia (Zr) Titanate (Ti)

RF   Radio Frequency

RMS   Root Mean Square

SEM   Scanning Electron Microscopy

TEM   Transmission Electron Spectroscopy

TGA   Thermal Gravimetric Analysis

UV   Ultra Violet

XPS   X-Ray Photoelectron Spectroscopy

LIST OF ILLUSTRATIONS

LIST OF TABLES

Chapter 1 - Introduction

Inkjet printing is already commonplace for reproducing graphics in our offices and homes; the technology is now being applied to fabricate 3D objects. While dye- and pigment-based inks and inkjet printers are commercially mature, the fabrication of mechanical and electrical components is in its infancy. This thesis tackles the printing of dielectric materials and both nanoparticle and new particle-free silver inks. There are some key parameters that make radio frequency (RF) fabrication unique; these include sensitivity to metal conductivity due to the skin effect at high frequency, dielectric constants, and loss tangent concerns that are all addressed in this thesis.

1.1 Motivation

The fabrication of tens of millions of tiny electronic components on a chip area the size of a fingernail is one of the crowning achievements of the last century, which has been dubbed the *"silicon age".* The sophistication involved in shrinking component size has lowered costs to a point where electronics are everywhere. While the scaling process continues towards ever smaller, cheaper, and faster devices, applications that simply cannot be scaled remain. Electronics such as lighting, displays, solar cells, and RF passives are inherently large in area. Radio frequency passives have dimensions that are defined by the frequency of operation, and they appear in all wireless devices from cell phones to FM radios. When placed "on chip", the RF passives take up expensive real estate as a result of their size and have performance limitations due to their material and size constraints. For this reason, RF components are typically not placed on silicon

chips but fabricated on lower cost substrates and then bonded to the chips. This is more

complex and costly process that has hindered cost-sensitive high volume applications

such as RF identification tags. By fully printing RF circuits, there is potential to

dramatically reduce the number of fabrication steps, time, and costs that are associated

with RF electronics. Just as multilayer and multi-material processes are common "on

chip" or with circuit boards, the same is possible for inkjet-printed electronics. While

much research has been undertaken to date on conductive inks, little work has been

done on printed dielectrics. Both the conductor and dielectric need to be integrated in

order to create a multilayer inkjet printing process that is capable of making quality

passives such as capacitors and inductors. New materials and printing processes must

be established to enable the creation of such a process.

1.2   Objectives

The overall aim of this study is to investigate the current state of the art in materials

suitable for the inkjet printing of RF passives. Special attention is given to problems

specific to RF devices, including the loss tangent of the dielectric and extreme sensitivity

to conductivity and metal thickness at high frequencies due to the skin effect. The

quality factors of fabricated inductors and capacitors are used to gauge the

performance of the devices. The specific objectives of this work are as follows:

- Develop a high-K and low loss dielectric ink and process and demonstrate high
  energy density RF MIM capacitors, with high quality factors and GHz operation;
- Develop a multilayer inkjet printing process using a printed dielectric combined
  with a conductor and printed vias for RF passives; and

- Integrate 3D inkjet dielectric material with a printed conductor to demonstrate complex shapes and truly 3D fully inkjet-printed RF passives.

1.3 Challenges

- Many of the best RF dielectrics are based on ceramics such as alumina; however, printing a ceramic material can be problematic for inkjet deposition. Particle inks tend to agglomerate and cause nozzle blockage, along with a final deposition of thick and rough films that is not ideal for electronics.

- Thin dielectrics are important for high energy density in capacitors; however, pinholes and non-uniformity are major concerns during the printing process.

- Thermal compatibility is expected to be an issue between printing a metal conductor and a polymer/ceramic dielectric. For example, the high heat sintering of a metal conductor may damage a polymer dielectric.

- In order to have a flexible process, vias connecting the layers would be ideal. Making low resistance and consistent vias within an all-inkjet multilayer process is expected to be difficult.

- Several micro-meter thick printed conductors with high conductivity are necessary for high quality RF components. Inkjet printed nanoparticle based conductors tend to be thin <500nm per layer with lower conductivity than bulk metals.

1.4 Organization

The structure of the thesis is outlined below:

Chapter 2. Literature Review: The background of alumina capacitors and progress towards the printing of alumina material are presented first. A literature review is completed on what has been done in fully inkjet-printed RF devices, which is followed by a look at previous work on 3D inkjet printing of passives.

Chapter 3. Fundamentals of Inkjet: Jetting as well as ink/substrate interaction are discussed in this chapter. Background information on functional ink design and methods used in the thesis are also presented.

Chapter 4. Inkjet Alumina MIM Capacitors: Alumina dielectric is commonly used in RF applications. A custom particle-free aluminum dioxide ink is investigated. High-density metal insulator metal capacitors are demonstrated with thin (~100nm) printed films and GHz operation.

Chapter 5. Fully Printed Multilayer Capacitors and Inductors: A thermally cross-linked Poly-(4-vinyl phenol) insulator material and silver nanoparticle ink are utilized to demonstrate a fully inkjet-printed RF passive process. Capacitors and inductors with inkjet printed vias capable of connecting the layers are presented.

Chapter 6. 3D Inkjet-printed RF Passives: Utilizing 3D inkjet printing technology with a UV-cured polymer dielectric, a custom silver particle-free ink is characterized with superior performance to nanoparticle ink. It has excellent jetting characteristics and stability and provides higher conductivity at lower temperature. A filter is demonstrated with low insertion loss, as well as an antenna with high efficiency and a complex 3D printed structure.

Chapter 7. Future Work: A summary of the work undertaken in conjunction with this thesis and insights into possible future directions of printed RF electronics are presented.

1.5   Contributions

- A well-characterized inkjet-printed sol-gel based high-K alumina dielectric with thin ~100nm layers has been developed;

- An Inkjet/photolithography-based process to create alumina MIM capacitors with airbridges has been established;

- A fully inkjet-printed multilayer process for making RF passives with vias has been created; and

- A 3D inkjet printing material has been integrated with an inkjet conductor to create fully 3D inkjet-printed passive components, demonstrating high conductivity at low processing temperature utilizing laser sintering.

Journals

1.   G. McKerricher, J. G. Perez, and A. Shamim, "*Fully Inkjet Printed RF Inductors and Capacitors Using Polymer Dielectric and Silver Conductive Ink With Through Vias*," IEEE Transactions on Electron Devices, vol. 62, no. 3, pp. 1002–1009, March 2015.

2.   G. McKerricher, D. Titterington, and A. Shamim, "*A Fully Inkjet Printed 3D Honeycomb Inspired Patch Antenna*," IEEE Antennas and Wireless Propagation Letters, pp. 1–4, July 2015.

3. V. Mohammed, G. McKerricher, and A. Shamim, "*Robust Design of a Particle Free Silver-Organo-Complex Ink with High Conductivity and Inkjet Stability for Flexible Electronics,*" Manuscript ID: am-2015-08125n, accepted with revisions, ACS Applied Materials & Interfaces (full paper), October 2015.

4. G. McKerricher, R. Maller, M. McLauchlan, and A. Shamim, "*Inkjet Printed Alumina for Radio Frequency MIM Capacitors,*" Wiley-VCH Small (full paper), under submission.

5. G. McKerricher, V. Mohammed, and A. Shamim, "*Fully 3D Inkjet Printed Lumped Element RF Filter,*" IEEE Microwave and Wireless Component Letters, under preparation.

Conferences

1. G. McKerricher, A. Nafe, and A. Shamim, "*Lightweight 3D Printed Microwave Waveguides and Waveguide Slot Antenna,*" IEEE International Symposium on Antennas and Propagation (AP-S/URSI), Vancouver, Canada, pp. 1-3, July 2015.

2. G. McKerricher D. Titterington, and A. Shamim, "*A 3D Printed Microstrip Patch Antenna,*" European Conference on Antennas and Propagation (EuCAP), Lisbon, Portugal, pp. 1-3, April 2015.

3. E. Arabi, G. McKerricher, and A. Shamim, "*Comparison of filters: Inkjet printed on PEN substrate versus a laser-etched on LCP substrate*," IEEE European Microwave Week (EUMCW), Rome, Italy, pp. 1226–1229, October 2014.

4. G. McKerricher, D. Conchouso, B. S. Cook, I. Foulds, and A. Shamim, "*Crude oil water-cut sensing with disposable laser ablated and inkjet printed RF microfluidics,*" IEEE International Microwave Symposium (IMS), Tampa, Florida, pp. 1–3, June 2014.

5. G. McKerricher, J. M. Gonzalez, and A. Shamim, "*All Inkjet Printed Microwave Capacitors and Inductors with Vias*," IEEE International Microwave Symposium (IMS), Seattle, Washington, pp. 1–3, June 2013.

Chapter 2 - Literature Review

Inkjet printing of RF passives requires both a dielectric material as well as a good conductor. While printed conductors have been investigated heavily and nanoparticle inks are available commercially, inkjet dielectrics are much less common. In addition, while several inkjet antennas have been fabricated with printed conductors, relatively little work has focused on other basic components such as inductors and capacitors. In this thesis, fully inkjet-printed passives are investigated, with a special focus on printed dielectrics. This literature review chapter is therefore organized as follows. First, a general overview of solution processed and inkjet-printed dielectrics is given. Second, literature concerning alumina dielectric, which is a common low loss dielectric for RF components, is reviewed. Next, literature related to fully printing RF passives (specifically inductors and capacitors) and creating a multilayer process with vias is explored. Finally, literature covering 3D inkjet printing related to RF passives is reviewed.

2.1 Printable dielectrics

Much of the work on printable dielectrics has been related to thin film transistors. Organic semiconductors have been intensely investigated over the past two decades, along with many soluble organic dielectrics for thin film transistors. This work has been driven by low frequency display applications. Most of these organic dielectrics have been printed, but they are commonly spin-coated to demonstrate devices [1],[2]. They exhibit dielectric constants typically in the range of 2.1 to 4. Some popular options for solution-processed dielectrics are poly (methyl methacrylate) PMMA, soluble

fluoropolymers such as Cytop and Teflon AF from DuPont, polystyrenes, Poly (4-vinyl

phenol) PVP, and polyamides. Soluble fluoropolymers have similar properties to PTFE

(which means low dielectric loss), but their extreme hydrophobic behaviour would make

them difficult to integrate into a multilayer inkjet printing process [3],[4]. While PMMA

has been inkjet printed [5] and successfully used as a thin dielectric [6] [7], even in bulk

form it generally has poor dielectric loss >0.03 [8]. The first work on multilayer passives

utilized polyimide; these passives were relatively thick films (3um) and rough. Another

prevalent dielectric, PVP, can handle temperatures greater than 180°C and has been

shown to inkjet print in [9],[10]. Recently, during the course of this thesis, PVP has also

been reported for inkjet-printed RF MIM capacitors [11], although without vias.

Since the first reports of high performance oxide semiconductors in 2004 [12], solution-

processed oxides have quickly outperformed their organic competitors (with the drive

again being thin film transistors for displays). The main dielectric contestants are SiO_2,

ZrO_2, HfO_2, Al_2O_3, TiO_2, Y_2O_3, and Ta_2O_5 [13]. These oxides have dielectric constants that

range from 3.9 (SiO_2) to greater than 60 for the non-linear dielectric TiO_2 [14]. Of these

dielectrics, ZrO_2 has been inkjet printed as a dielectric in a fully inkjet-printed transistor

[15]. However, zirconia has relatively poor RF performance due to its loss tangent of

0.05-0.1 [16]. To date, two studies of RF devices have reported using inkjet-printed

oxide particles, specifically alumina. These inkjet alumina studies are covered in the next

section.

2.2   Inkjet printing of alumina dielectric

The ceramic alumina is among the best and most common RF materials, which is why it has been selected for this inkjet printing investigation. Metal-insulator-metal capacitors are used to demonstrate the utility of inkjet alumina as well as to provide the means to gather material characterization data. To date, there has been considerable research showing the benefits of alumina for MIM capacitors but with fairly complex deposition tools. There has also been progress in solution processing this ceramic that leads us to a point where inkjet printing is attractive. It has several important properties that make it an ideal candidate for RF capacitors, including its low cost, high dielectric constant (Dk), decent dielectric temperature coefficient, good chemical stability, and high bandgap of 6.3 EV (which makes it a very good insulator). In its pure form, it is the material with the lowest known dielectric loss [17]. For RF applications, low loss is especially important for high quality capacitors and filter circuits with low insertion loss and low noise. Another important aspect for MIM capacitors is its high energy density, since this density enables the devices to be smaller and cheaper. High energy density can be achieved in two ways: shrinking the dielectric thickness or increasing the Dk. Alumina has a high dielectric constant of nine, and it has only electronic and ionic polarization mechanisms that respectively contribute 30% and 70% to the overall Dk. This means that alumina can provide a high energy density that is constant in the RF range. These properties are ideal for RF capacitors. Table 2-1 details some of the important properties of alumina [18], [19].

Table 2-1: Properties of alumina

Alumina	Melting Point	Band Gap	Resistivity	Dielectric Constant (Dk)	Dissipation Factor (Df)
α-Al_2O_3	2072°C	8.6 EV[1]	$1E^{13}$ Ω-m	9	0.0001

Alumina commonly refers to the crystalline α phase Al_2O_3 that forms the basis for many

gems, such as rubies and sapphires. However, when deposited as thin films for

electronics, it is normally amorphous. Amorphous films are desirable because

polycrystalline films have grain boundaries and volume change that degrade leakage

and breakdown performance [21]. Sputtered thin films of Al_2O_3 are found to be

amorphous even after sintering at 750°C [22]. With all of the superior properties of

Al_2O_3, SiO_2 is still the "go-to" insulating layer on silicon-based chips. The most significant

benefit of SiO_2 is that high quality films are easily grown on silicon wafer by thermal

oxidation, whereas alumina needs to be deposited.

2.2.1   Alumina MIM capacitors

Some of the first work on alumina deposition for use in electronics started in the 1960s

and involved E-beam evaporation of aluminum targets in an oxygen environment

[23],[24]. Early work also investigated anodic alumina grown thermally on aluminum

metal [25],[26]. These initial films did not have the best performance and had issues

with porosity, film stress, pinholes, positive ionic (Al ions) migration in porous layers,

and high dielectric loss. These are cautionary tales of the difficulties and control that is

---

[1] A transport bandgap of 8.7 EV is often quoted, although there are some variations in the literature. It is considered a direct bandgap insulator. Optical bandgap is ~6.3 EV [19],[20].

needed in processing alumina for electronics. Recent work has focused on RF sputtering and atomic layer deposition (ALD) to provide high performance MIMs. The table below highlights some recent alumina RF MIM capacitor results. Oddly, while the publications are geared toward RF MIMs, few report on the quality factor (which is why they are not reported in this table).

Table 2-2: RF MIM capacitor literature

Material	Bottom & Top Metal (nm)	Dk Thick-ness (nm)	Leakage (A/cm^2)	Break-down (MV/cm)	Energy Density $(fF/um^{2)})$	Quality Factor	Ref.
ALD Al_2O_3	20/500 Ti/Au 3um Cu	59	$3E^{-7}$ @20V	7	1.55	-	Yota 2013 (Skyworks)[27] & [28]
ALD Al_2O_3	Cu barrier	~35	$1E^{-8}$ @3.3V	-	3.0	-	Tu 2003 (TSMC) [29]
ALD - Al_2O_3	Ti/Au 20/400 Au 3um	100	-	-	0.78	40 @ 2GHz <2pF cap	Jiahui 2015 [30]
Sputter Al_2O_3	Al 200	300	-	>2.3	-	50 to 100@ 10KHz	Murray 2012 [31]
ALD Al_2O_3 HfO_2 Hybrid	TaN and Al	13	$7.45E^{-9}$ @2V	~4	12.8	-	Hu 2003 [21], [32]

From Table 2-2 it is clear that these films have excellent leakage current values ($3x10^{-7}$ A/cm up to 20V with a 59nm film) and that quality devices can be fabricated with alumina. Normally, thick metal layers (>500nm) are used as contacts. Quality RF components rely on thick and highly conductive metals. The metal used also has an effect on leakage current. In [33] it is shown experimentally that aluminum has the best characteristics, followed by gold; the worst is silver. The work correlated the lower leakage to metal contacts with higher ionization energy. This is useful information, as the same trends should be seen in an inkjet-printed alumina.

2.2.2   Solution-processed alumina

Recently, several groups have demonstrated solution-processed alumina as a dielectric layer with good results. This work is not directed towards RF MIMs but driven by thin film transistors, mostly for large area electronics (i.e. displays). Nevertheless, the spin-coated films show potential for being used for RF MIMs and also to be printed. Some notable work in this area is summarized in Table 2-3.

Table 2-3: Spin-coated alumina

Salt & Solvent	Bottom & Top Metal (nm)	Dk Thick-ness (nm)	Leakage (A/cm^2)	Break-down (MV/cm)	Dk & Df	Temp. ^oC	Ref.
$AlCl_3$ ACN/EG	Mo IZO	110	$6.3E^{-6}$	4	6.3 - @10KHz	300	Avis 2011 [34]
$AlCl_3$ ACN/EG	Mo 40 Mo/Au 3/50	120	$6.3E^{-6}$ 1MV/cm	4	7.2 -	300	Kim 2013 [35]
$AlCl_3$	p^+Si	95	~$3E^{-8}$	-	6.2 -	250-	Nayak 2013

ACN/EG	Al 80		@2V			500	[36]
AlN_3 Acetic Acid	Ti-Pt Ti-Pt/Au	~250	$10E^{-7}$ 0.1MV/cm	>1.5	6.5 -7.5 0.01 @1KHz	550	Hu 2013 [37]
AlAc 2-ME	Mo IZO	70	$6.3E^{-6}$	4	6.3 - @10KHz	150	Peng 2013 [38]

The spin-coated results in Table 2-3 show that the films are not ALD grade but that they do have low leakage current values and thickness ranges that make it attractive to move towards inkjet printing. Some sol-gel processed semiconductors have similarly moved from spin coating to inkjet, as well as zirconia oxide dielectric [39],[15]. The sol-gel inkjet work demonstrates that creating quality films and printed features is challenging but attainable.

2.2.3 Current inkjet printed alumina

The overall idea is to inkjet print alumina and demonstrate MIM capacitors. A depiction of the process is shown in Figure 2-1.
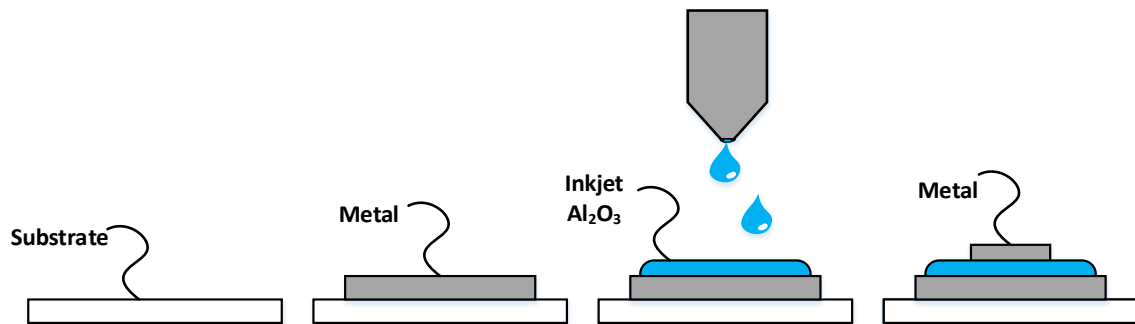
Figure 2-1: Inkjet printing of alumina dielectric for MIM capacitors

To date, only printed films have been shown with particle-based inks [40], [41]. Large particle based inks provide a rough and thick film (approximate thickness: 15um), where the use of binders affects the dielectric properties. However, they [41] were able to

demonstrate MIM capacitors with Qs of 400 at 1 MHz. Another approach is to use

nanoparticles of Al_2O_3, which has been investigated in [42] (although MIM devices were

not fabricated). Issues with nozzle clogging from the nanoparticles and difficulties

creating thin uniform films with these aqueous solutions both appear to be problematic.

It is likely that thin nanoparticle films would be inferior to the sol-gel approach due to

porosity and grain boundaries. Overall, there have been two demonstrations of inkjet

alumina MIM capacitors (low frequency), but non-particle based printing or thin-film

printing of alumina has never been reported to this author's knowledge. Furthermore,

RF MIM capacitors using printed alumina have never been demonstrated for GHz

operation.

2.3   Fully inkjet-printed RF passives

A multilayer inkjet printing process for electronics offers low cost, low material

consumption, reduced fabrication complexity, and a quick turnaround time. Although

these features are desirable for manufacturing, rapid prototyping is also of importance.

For the RF designer in particular, a quick turnaround is highly desirable during the

iterative process of creating passive matching circuits. In order to meet this challenge

and create an on-demand multilayer process, both a conductor and a dielectric need to

be printed together (as shown in Figure 2-2).
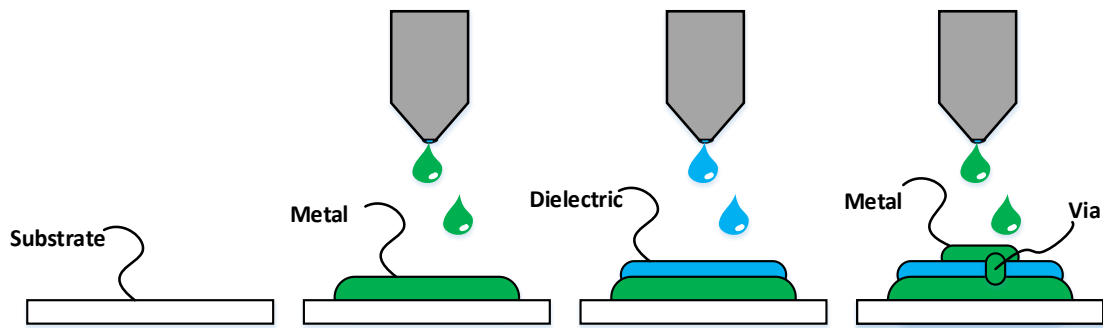
Figure 2-2: Full inkjet printing of RF components

While plenty of work has been undertaken on printing nanoparticles for antennas

[43],[44], little work has focused on inductors and capacitors – especially at higher

frequency. Pioneering work on inductors and capacitors utilizing both inkjet-printed

gold nanoparticles and printed dielectric polyimide layers is presented in [45],[46];

however, the demonstrated inductors have Qs of 0.5 and were characterized at low

MHz frequencies. More recently, inductors and capacitors utilizing printed dielectric

polymers were demonstrated in [47], but they were not characterized past 1MHz and

did not incorporate vias. Planar passives were demonstrated in [48], but without a

printed dielectric or high frequency device characterization. Recently, planar meander

inductors that were inkjet printed on a Kapton substrate operating at GHz frequencies

were shown in [49]. These planar inductors get around the problem of printing a

dielectric and multiple layers; however, this limits the flexibility of the process. While

MIM capacitors utilizing printed dielectric materials were presented in [11] and

measured at GHz frequencies, they do not incorporate vias. Vias created with a

conductive polymer are characterized in [50],[51]; they require the printing of a solvent

to create a hole and are used to make highly resistive interconnects for low frequency

transistors. In summary, there is already a wealth of reports on printing metals for RF

antennas, as well as some dielectrics and vias that have been developed for thin film

transistors. The goal of the current study is to integrate suitable materials and apply

them towards the fabrication of multilayer RF passives. Key factors to consider are the

temperature constraints of both the metal and dielectric, surface roughness,

conductivity, and dielectric loss.

2.4   Fully 3D inkjet-printed passives

The idea here is to take inkjet fabrication a step further and print a dielectric that allows

complex and thick 3D designs with integrated metal passives (see Figure 2-3). This is a

fully inkjet printing process where the dielectric is 3D printed and the metal can be

inkjet printed along with it.
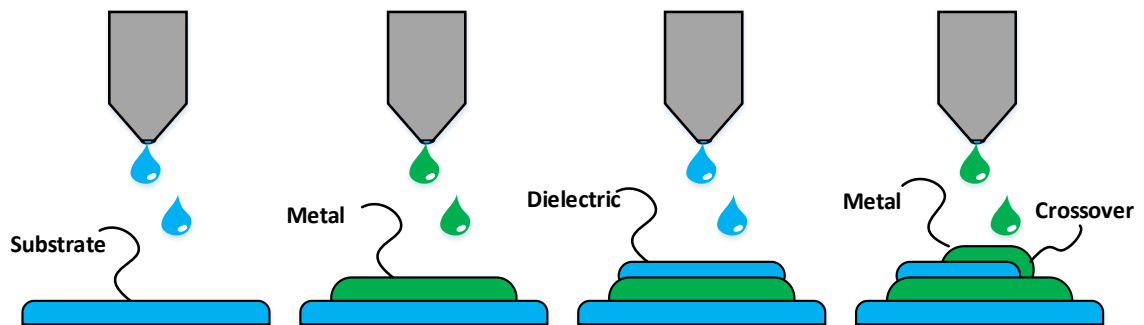
Figure 2-3: 3D inkjet printing of RF passive components

At the moment, UV-cured and wax materials are already being printed by industrial

print-heads to fabricate plastic parts. Materials are deposited drop by drop in a digitally

defined location to build a 3D object layer by layer. A major benefit is that no masks or

tooling are required. It is possible to stack or array inkjet print-heads in order to print

several materials within the same process or to increase the build speed. Industrial

print-heads can deposit kilograms of material per hour, potentially making the process

both fast and low cost. While several examples of physical objects fabricated by inkjet

are presented in [52], only a few 3D-printed passives at RF have been reported

[53],[54],[55]. These previous reports utilize common 3D printing techniques such as

fused deposition modelling and stereo-lithography. Reflectors and lenses that have

been printed by 3D inkjet are demonstrated in [56] and [57]. These inkjet-printed

dielectric antennas either do not incorporate metal or use metal sputtered in high

vacuum. Recently, 3D inductors and capacitors are shown in [58] using 3D inkjet objects

and filled by a syringe injecting silver nanoparticle ink. The major challenges of 3D

printing RF passives are poor surface roughness, integration of the conductor and

dielectric, low conductivity of printed metals, and poor dielectric losses. Poor surface

roughness, which is pointed out in [54], is inherent to many 3D printing processes. While

the 3D printing of conductors and metals is feasible, combining them together in the

same process is challenging due mainly to temperature compatibility. Metal

nanoparticles provide the potential to overcome this challenge, since the nanoparticles

allow much lower processing temperatures than a bulk metal. Silver nanoparticle ink

can be additively patterned, but in order to get the best conductivity, sintering

temperatures above 180°C are required [59]. These temperatures remain incompatible

with many printed dielectrics. Pastes, aerosols, and plating solutions are demonstrated

on 3D plastic structures, but they limits the flexibility of the process [53], [60]. It would

be ideal to have a conductor that could be printed with the dielectric layer by layer.

Alternative sintering techniques (such as laser, photo, and microwave) have been shown

to provide increased conductivity at lower temperatures [61],[62],[63]. There have also been reports of metal decomposition inks that can provide high conductivity at low temperatures [64]. With reported advances in inkjet inks and alternative sintering methods, it therefore seems reasonable to expect that conductors could be integrated with UV-cured polymers to create fully 3D inkjet-printed RF passives. To date there has been no report of 3D passives that integrate both inkjet conductor and dielectric.

2.5   Summary

Sufficient work has been undertaken on inkjet-printed conductors (particularly silver nanoparticles) for RF antennas. However, little work has been done in the RF domain on printed dielectrics. Both organic and inorganic solution-processed dielectrics have been developed for transistors in display applications. These developments set a good foundation for potential inkjet dielectrics that could be used for RF passives. In the above literature review, three topics are discussed: inkjet-printed alumina dielectric, the multilayer inkjet printing of RF passives, and finally fully 3D inkjet-printed RF passives. In the case of alumina, there are two reports of particle-based inkjet printed capacitors with poor surface roughness and thick layers. A particle-free alumina ink and smooth thin layers are presented in chapter 4. As for multilayer passives, a few reports of exist in the field, but GHz frequency range is rarely explored. These reports show that high frequency is a relatively new area to explore and that significant improvement is necessary if printed passives are to compete with conventionally fabricated devices. Finally, 3D inkjet printing is an emerging field and the possibility to integrate inkjet-printed conductors would enable new RF designs; this has not been explored to date.

Chapter 3 - Methods and Fundamentals of Piezoelectric Inkjet Technology

The work in this thesis is a combination of inkjet printing, materials processing, and characterization, as well as passive RF devices. Background information on RF devices and materials processing is briefly presented, as it sets the stage for the following experimental chapters. This background chapter gives an overview of piezoelectric inkjet printing, including the mechanism of jetting, surface tension, wettability, and the drying and sintering of materials after printing. Along with these fundamentals, it provides an understanding of the measurements and methods used in this thesis. Although inkjet has been around for decades, the science behind jettability, substrate fluid interaction, and the coffee ring effect continues to advance. Some of the classic and more recent advances are presented in this chapter.

3.1 Piezoelectric inkjet technology

Modern piezoelectric inkjet heads can contain thousands of densely spaced nozzles, each jetting 100,000 drops per second. Several kg of material can be deposited each hour with a single print-head. When inkjet was first seriously investigated in the 1970s, it was far from the workhorse it is today. Early devices such as the glass tube structure of Figure 3-1 are still used in research or for jetting either high temperature or corrosive fluids.
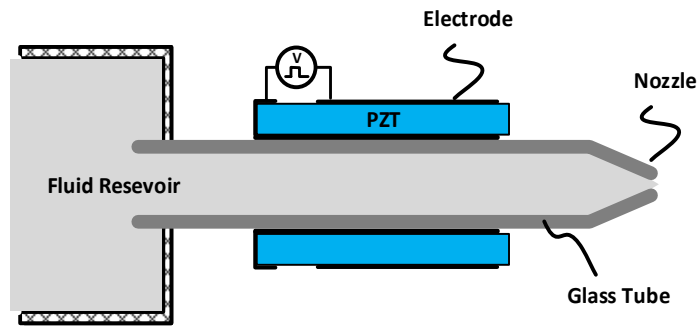
Figure 3-1: Piezoelectric Inkjet Device
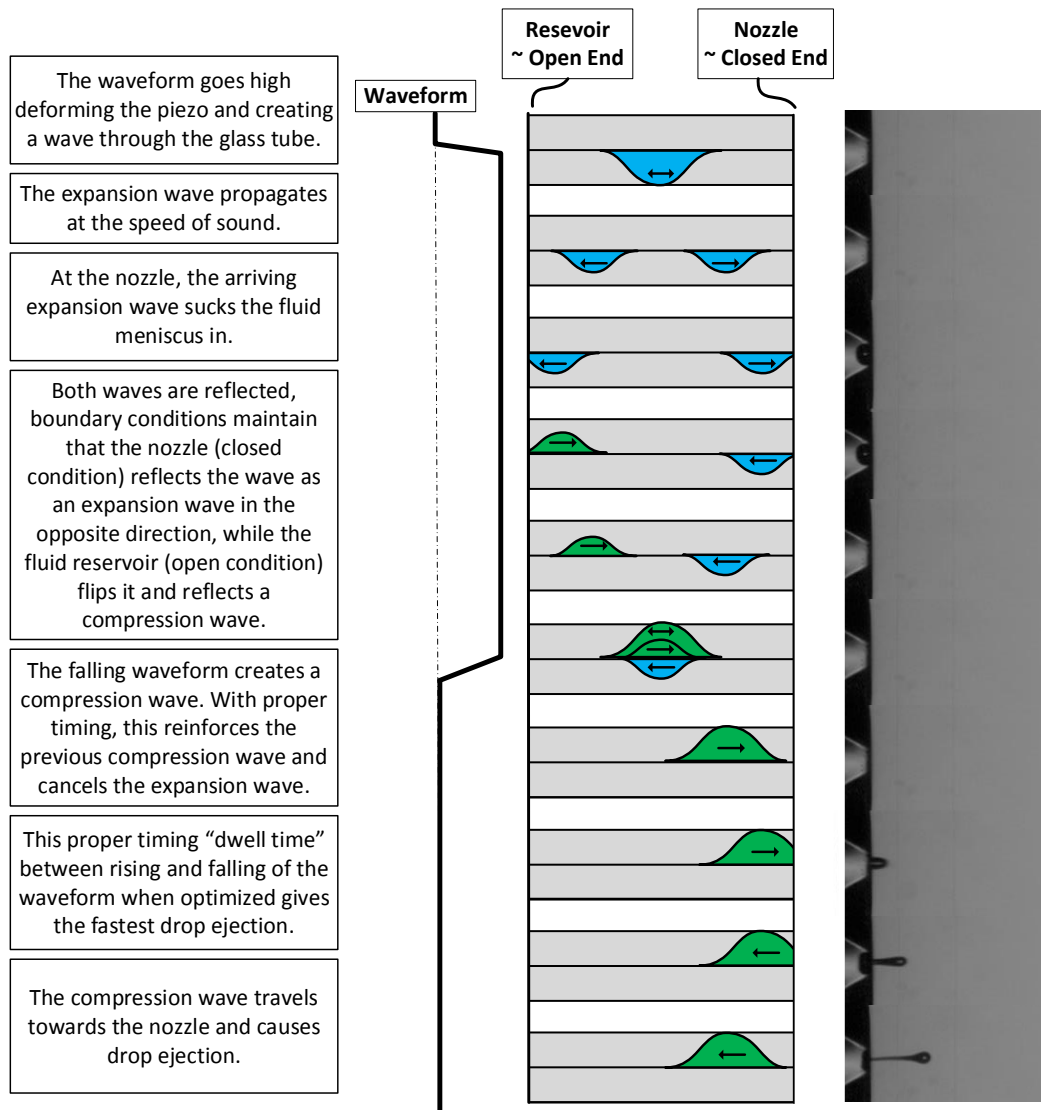
Figure 3-2: Simple acoustic model of a glass tube inkjet device. Waveform (left), acoustic illustration (center) and nozzle (right). (combined and adapted from [65] and[66])

The basic construction is a glass tube filled with ink and a piezoelectric crystal bonded around the outside of the tube. Wires from a voltage waveform generator connect to the electrodes of the tube[2]. In 1984, Bogy and Talke [65] explained the jetting of this device using a simple acoustic analysis and square wave pulse Figure 3-2.

Looking at the jetting operation of this device provides a solid foundation for all piezoelectric inkjet. While the simple square wave pulse can eject a drop, more complex waveforms are normally used. It is even possible to tune the waveform to eject different sized droplets. First used by Textronix in the Phaser product line, variable drop printing is now used by several print head manufacturers. This helps to create fine detail in certain areas of an image while maintaining high throughput in other areas. An example of waveforms used to generate different droplets in a piezoelectric print head are shown in Figure 3-4.
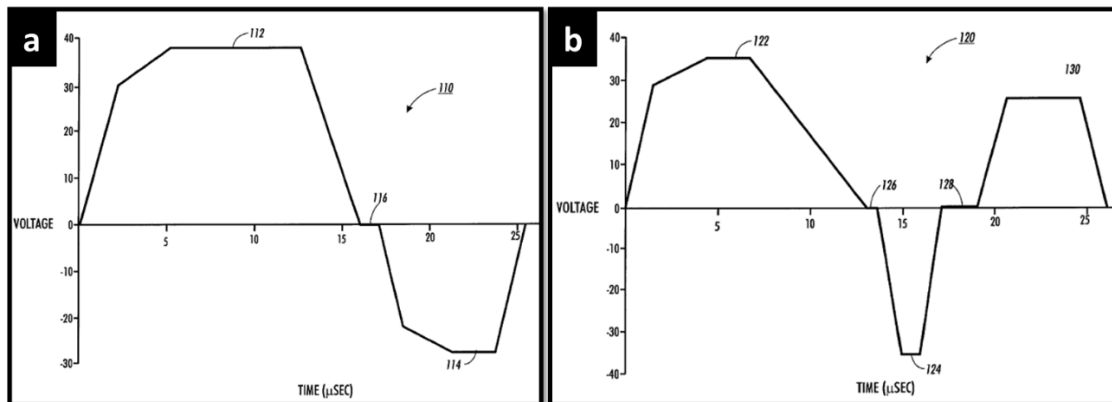
Figure 3-3: Example waveforms used for variable drop ejection within the same bend-mode print-head.(a) Larger drop waveform, 58 pL droplets (b) smaller drop waveform, 27 pL droplets.

---

[2] An engineer at Canon, Ichiro Endo who was investigating piezo inkjet found that when a hot soldering iron was touched to a tube, the ink was ejected. This started thermal inkjet development at Canon. While thermal is cheap and fairly common, it is slower, runs hotter, and typically with shorter print-head lifetime than piezo.

Although there are several different architectures for piezo inkjet, a common variant is

the bend mode shown in Figure 3-4 (a). The precision of the fabrication is phenomenal,

see Figure 3-4 (b) a perfect 21um diameter nozzle. Figure 3-4 (c) is a look inside an array

of pumping chambers and nozzles and shows the dense packing of the array. Then, in

Figure 3-4 (d) there are pillars that are used for acoustic damping. Back in Figure 3-2

notice that at the end of the drop ejection the wave will again be reflected; this

generates unwanted resonances in the device. Engineers have introduced the

terminator to dampen reflected waves and reduce unwanted resonances. This is

especially important as modern piezo-heads can run up to 100 KHz [67]. These features

are fabricated using semiconductor lithography techniques. This allows thousands of

devices to be fabricated on one jet stack with high repeatability. It is claimed by Menzel

et al. that the current fabrication process for the inkjet features and channels could be

scaled down to 3um nozzle sizes.[68]
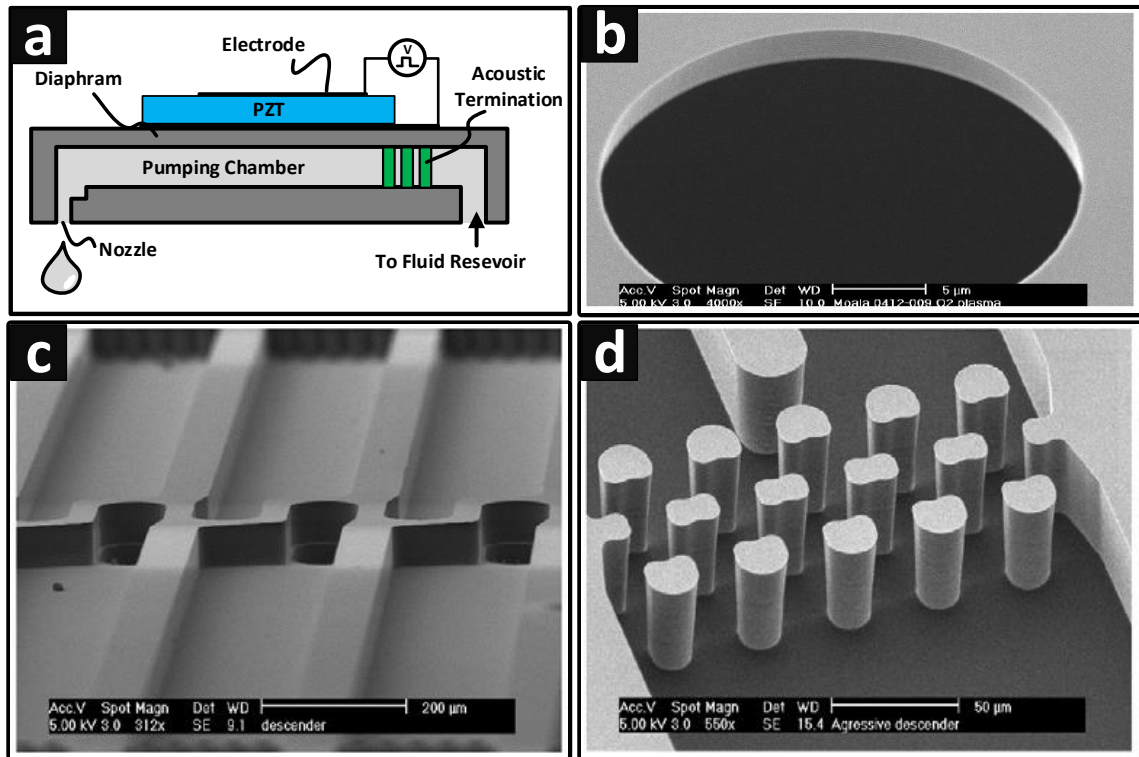
Figure 3-4: (a) Bend-mode inkjet architecture (b) nozzle (c) inside look at array of pumping chambers and nozzles (d) acoustic terminator. (From Spectra/Dimatix Inc.[68])

3.2   Fluid Fundamentals for inkjet

In 1936 Wolfgang Ohnesorge published a PhD thesis focused on experiments and

photography of drops and breakup of liquid jets. For the 1930's, he took excellent

images of fluids with different viscosity and surface tension ejected from a nozzle. He

studied a large space from slow dripping droplets to high pressure flow where the fluid

atomizes into a spray[3]. The mapping drawn by Ohnesorge in his 1936 paper is shown in

Figure 3-5 (a)[70]. He uses the Reynolds number on the x-axis and a new dimensionless

variable for the y-axis, which we now call the Ohnesorge number (Oh).

---

[3] Ohnesorge lamented to his family that his ground breaking work on imaging and characterizing droplets was tedious and difficult with many initial failures[69]. He defined four regions in his experimental space which are: (0) Slow dripping, (I) Axisymmetric Raleigh breakup, (II) Screw-like perturbations and wavy break up, (III) atomization of the jet. Regions I-III can be seen in the original graph Figure 3-5 (a).
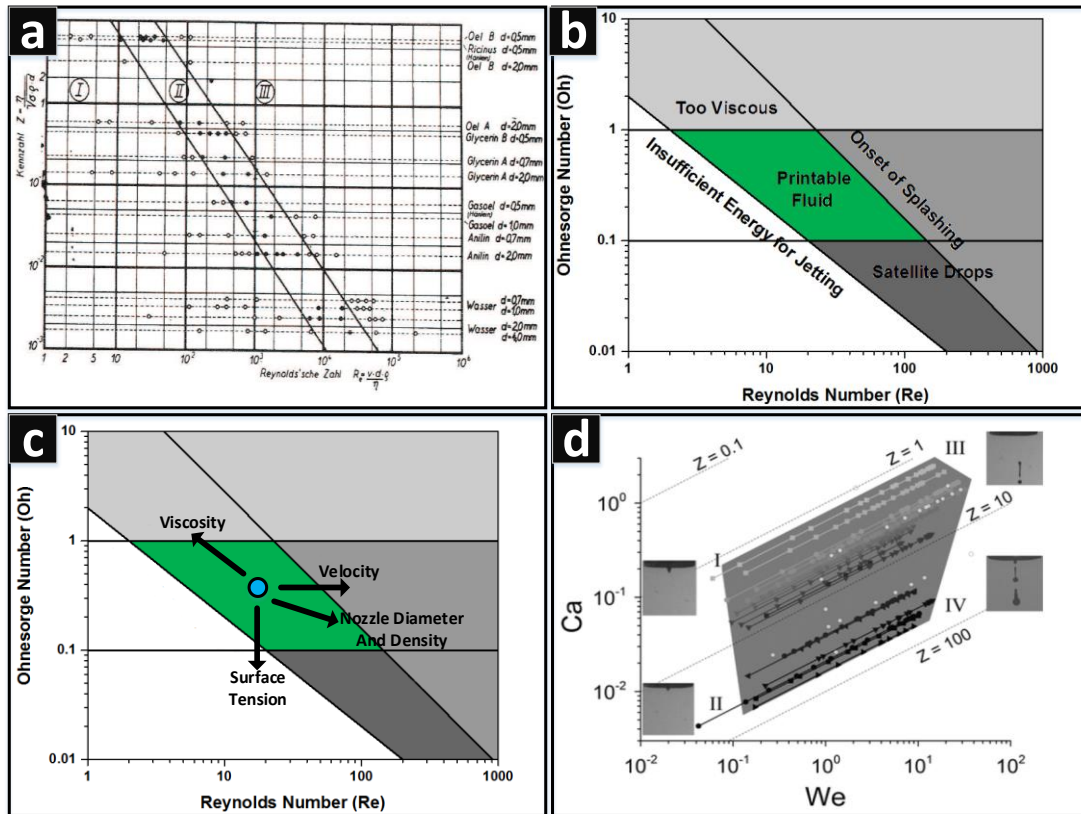
Figure 3-5: (a) Original fluids mapping by Ohnesorge, (b) adaptation of drop on demand mapping from [71][4], (c) Mapping showing the movement of operating position of dimatix model fluid (blue circle) with an increase in each parameter. (d) Experimental mapping of drop on demand as a function of capillary number and Webers number.

The common dimensionless numbers in fluid dynamics are given below:

$$Oh = \frac{\eta v d}{\sqrt{\rho v^2 d^2 \times \sigma d}} = \frac{viscous\ forces}{\sqrt{inertia \times\ surface\ tension}} \qquad 3\text{-}1$$

$$Re = \frac{\rho v^2 d^2}{\eta v d} = \frac{inertial\ forces}{viscous\ forces} \qquad 3\text{-}2$$

$$We = \frac{\rho v^2 d^2}{\sigma d} = \frac{inertial\ force}{surface\ tension} \qquad 3\text{-}3$$

$$Ca = \frac{n v d}{\sigma d} = \frac{viscous\ force}{surface\ tension} \qquad 3\text{-}4$$

---

[4] Note that Derby's initially mapped the space with Webers and the Z parameter, Z is simply 1/Oh. The original plot also has a factor of 10 error in Re number (x-axis). The plot shown here is consistent with [69].

Where η is viscosity, σ is surface tension, ρ is density, v is velocity, and d is the diameter

of the nozzle in our case. Ohnesorge was looking at fluids flowing through a nozzle,

which is very similar to the drop on demand inkjet printing situation. From this mapping

idea, Derby et al, studied jet-ability space of drop on demand printing. They defined a

space where fluids would be too viscous to print Oh >1, or with satellite drops Oh<0.1.

He also used equations for the onset of splashing at Oh = 50/Re5/4 and Oh =2/Re.

Plotted in Figure 3-5 (c), is the operating point (blue dot) where the Dimatix model inkjet

fluid fits [72] shows the parameters for the fluid.

Table 3-1: Dimatix Model Ink Parameters

Dimatix Model Ink	Viscosity (cp)	Surface Tension Dynes/cm	Density g/ml	Nozzle Diameter (um)	Velocity m/s	Re	Oh	We	Ca
	10	30	1	21	10	21	0.4	70	3.3

Unsurprisingly, the fluid has been designed to fit right in the sweet spot for jetting (blue

dot in Figure 3-5(c)). Notice the arrows point in the direction to which the point will

move for a positive increase in viscosity, surface tension, nozzle diameter, density and

velocity value. Since the results were published by Derby, there has been some

discrepancy in the jetting window notably from [73] and [74]. Figure 3-5 (d) from

Nallan et al. [74] is a jetting window in Ca – We space which is more specific and

experimentally verified with Newtonian solvents (with and without nanoparticle

loadings). Nallan shows a wider range of Oh numbers which can be printed from Oh of 1

to 0.016 (Z=1/Oh, Z range of 1 to 60). This type of work provide insights into the design of ink for good jetting.

3.3   Ink substrate interaction

One difficulty with inkjet as opposed to non-digital gravure or screen printing is that the ink viscosity is very low. Generally around 10 centipoise, just a bit more viscous than water. Conversely, screen printing inks have a viscosity more like honey. Combating the unwanted spreading is why inkjet paper is engineered with an absorbing polymer surface. Another solution is to use phase change inks, basically printing molten crayons that rapidly dry on the surface and do not spread. UV cure ink is also popular where the ink is exposed to a UV light immediately after printing to pin the drops in place; again avoiding spreading. This work however, focuses on functional electronic inks where ink spreading is something that needs dealt with. The substrate and ink interaction is key to final film quality. Understanding this interaction requires a look at surface energy of the substrate and the ink.

3.3.1   Surface tension

It has been said that if a person were small enough to fit inside an inkjet droplet they would not be able to escape, due to surface energy. It acts like an elastic outer wall around the droplet and becomes more and more dominant as the size scale shrinks. Surface tension can be measured by pushing a droplet from a nozzle so that it hangs with a pear shape just before falling. Gravity forcing it to drop under its own weight and surface tension keeping it together.
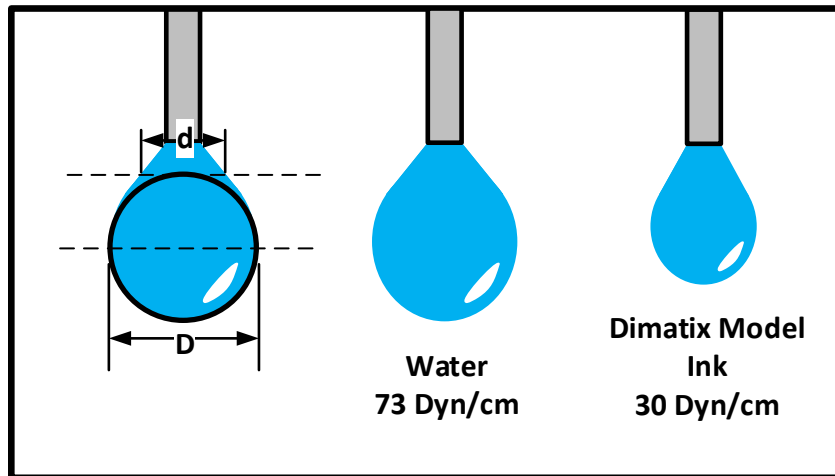
Figure 3-6: Surface Tension measurement with Pendant Drop Technique, and example shapes (using rame-hart calibration standard 100-27-05).

Figure 3-6 shows important dimensions from the pendant drop as well two examples of how the drops look from a syringe[5]. The surface energy can be calculated with the following equations from the classic 1937 paper by Andreas et al [75]. Although there are more advanced methods, this early method is still useful and provides understanding.

$$\gamma_L = \frac{(\rho_1 - \rho_2)gD^2}{H} \qquad\qquad \text{3-5}$$

$$S = \frac{d}{D} \rightarrow Table\ lookup\ \frac{1}{H} \qquad\qquad \text{3-6}$$

Where ρ_1 and ρ_2 are the density difference of the two fluids, typically ink and air in our case, g is the gravity constant, and H is determined via the lookup table which is attached in appendix 1.

---

[5] The shapes are not to scale and are only examples to give an idea of how small droplets with different surface tension really look out of a syringe, the shape of the droplets cannot be scaled at will.

3.3.2 Substrate surface energy and contact angle

When you notice rain drop bead on a leaf or completely wet a smooth piece of glass you will have seen substrate surface energy in action. This needs to be controlled carefully in coating applications, from painting to inkjet printing. Young described the phenomenon of surface energy and wetting in 1805 with the simple force balance Equation 3-7 and Figure 3-7.

$$\gamma_{SV} = \gamma_{SL} + \gamma_{LV}\cos\theta \qquad\qquad 3\text{-}7$$
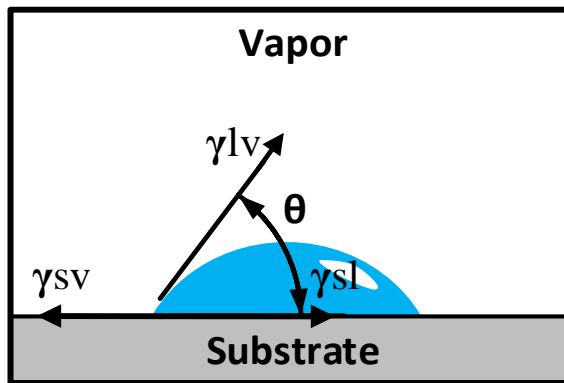
Figure 3-7: Contact angle and forces acting on a sessile droplet

Where θ is the contact angle, and γ_{SV}, γ_{SL}, γ_{LV} are the interfacial tension of the solid-vapor, solid-liquid, and liquid-vapor interfaces. The measurement of contact angle is straight forward with a good camera and compass, and γ_{LV} was discussed in the last section. However, determining γ_{SL} and γ_{SV} requires more work. The numerous methods available and extensive literature on the subject makes this subject daunting. One of the best, commonly used, and experimentally simple methods is Fowkes method, a classic paper from 1964 [76]. In this approach Fowkes breaks the surface energy into both a polar and dispersive component ($\gamma = \gamma^P + \gamma^D$) which unfortunately creates even more unknown variables. However, Fowkes method takes advantage of the unique properties

of materials. Water has a high polar component, while Teflon and diiodomethane have

zero polar component simplifying the equations and providing high accuracy. A full walk

through of Fowkes method is provided in Appendix 2 based on [77]. Using PMMA

(poly)methyl methacrylate (Plexiglas) as an example substrate, all variables can be

solved with only the four contact angle measurements shown in Figure 3-8 The

properties of the materials are given in Table 3-2.
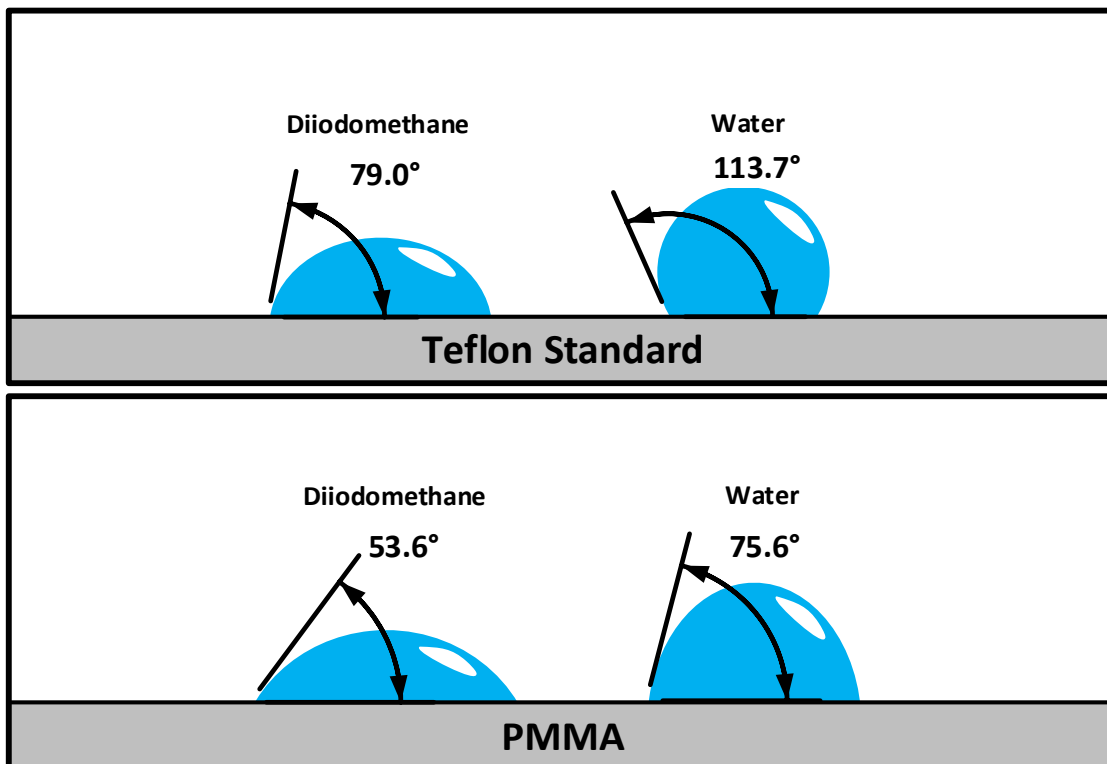
Figure 3-8: Contact angle measurements of Diiodomethane and water on Teflon and PMMA.

Table 3-2: Surface Energy

Material	Polar (dyn/cm)	Dispersive (dyn/cm)	Total (dyn/cm)
Water	51.0	21.8	72.8
Diidomethane	0	50.8	50.8

Teflon	0	18.0	18.0
PMMA	5.7	32.2	37.9

3.3.3 Wettability

As discussed at the start of this section the low viscosity means that the fluid is capable of moving on the substrate without much restriction. When starting to print, the ink will either spread all over the substrate or ball up due to high surface tension. As a general rule, ink should have a surface energy that is below that of the substrate [78]. Ink that makes a contact angles of around 15° are often used [79]. Wettability is normally a trial and error process where either the ink or the substrate can be modified. Changing the ink can affect functionality, stability, and jetting, therefore the substrate is good place to start. Application of a very thin physical layer, cleaning, plasma, and UV ozone treatment can be used. Below is an example how two minutes of Oxygen plasma lowers the contact of angle of water on the surface. The plasma breaks surface bonds creating a dangling bond which has a higher surface energy.
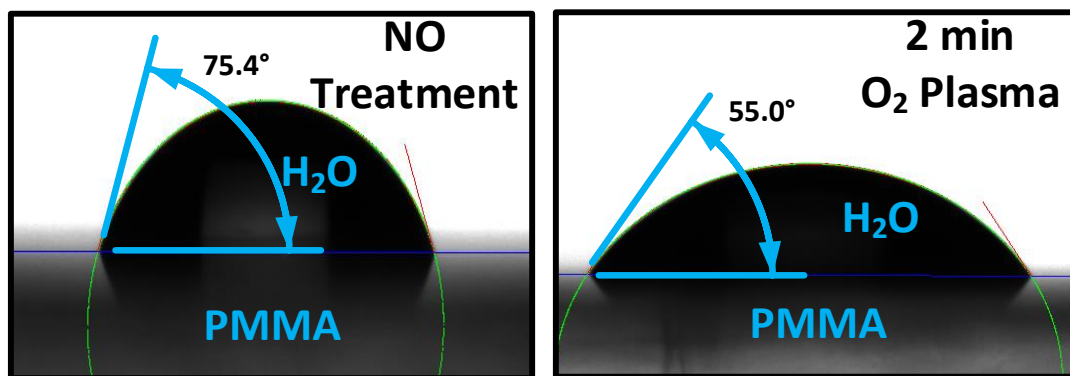
Figure 3-9: Photographs of water droplets on PMMA showing the effect of O_2 plasma treatment

3.3.4 Drying and Coffee Ring

When spilled coffee is left to dry on a table, its observed that as the water evaporates,

the coffee particles accumulate at the edge of the spill and with few particles in the

middle. Surprisingly, it was not until 1997 when this was explained by Deegan et al [80].
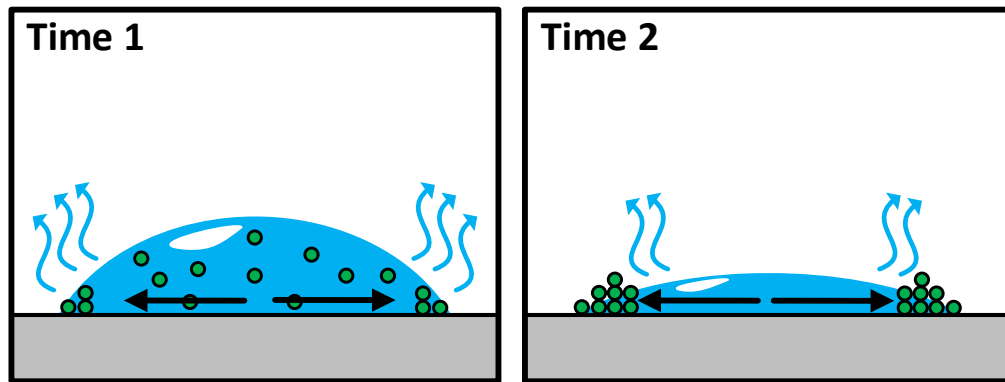
Figure 3-10: Depiction of coffee ring stain

As shown in the Figure 3-10 the particles in the solution are deposited at the contact

line of the droplet, pinning the contact line. Since the evaporation is greater around the

edge of the drop per unit volume of solvent, there exists a flow from the center of the

drop to the edge depositing the solute. This effect can be reduced by increasing the

contact angle, reducing the temperature of the substrate, increasing the viscosity and by

using co-solvents with different evaporation rates[81][82][83].

3.3.5 Printing lines

In order to understand how to print features, Soltman et al. started by looking at

printing lines. By studying the drop spacing and the delay between each drop a space

can be mapped out a space where a uniform line can be printed as shown in Figure 3-11.
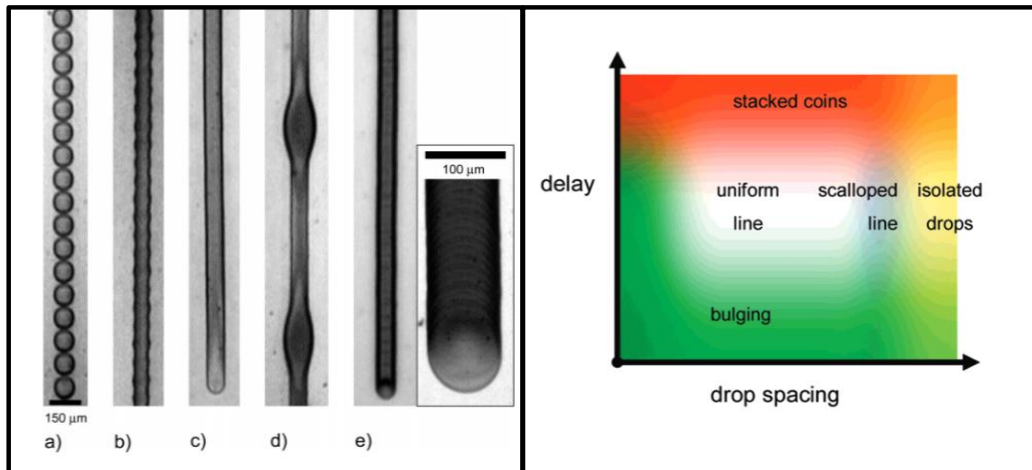
Figure 3-11: (left) Printed line behaviours (right) printed line behaviours at an intermediate temperature[84]

Clearly, when the drop spacing is too large, isolated drops will form on the substrate. This can be seen in Figure 3-11(a). As the drop spacing is decreased the amount of fluid in the line increases, first a scalloped line appears (b), and then an ideal smooth line (c), next a line with bulges due to the excessive ink (d). Finally in Figure 3-11 (e) the delay between drops is so great that the previous drop has time to dry on the surface, this creates rough lines we call "stacked coins". A map of delay and drop spacing is shown on the right side of Figure 3-11.

3.4 Drying and annealing

In many electronic inks, heat is needed to drive off the solvent and forms the final film. In the case of nanoparticle inks, the interesting thing is that the size of the nanoparticle lowers the melting temperature and surface pre-melting [85]. This enables heat treatment at relatively low temperatures to form continuous films. For precursor based inks, heat is necessary to drive the decomposition reaction. And for thermal crosslinked polymers, heat treatment is necessary to complete the crosslinking reaction. Many

polymers may need a specific thermal anneal to form the appropriate crystal ordering.

An exception is UV cured polymers which require a UV source to drive a polymerization

reaction. Although some UV polymers still need a thermal treatment to drive off excess

solvent first.

3.5   Creating functional inks

As stated in the previous sections industrial inkjet has primarily been a tool for graphic

arts industry. The development of inks for inkjet has many requirements. Jettability of

the fluid, viscosity and surface tension requirements. The drying out of the ink can cause

clogging as well as agglomeration of nanoparticles within the ink. Air bubbles and

foaming can be problematic and even bacteria growing inside of water based inks. There

is a substantial body of research on functional inks with semiconducting, piezoelectric,

gas sensing and other properties. In this thesis, we will focus on metal-based conductive

inks[6] and dielectrics which are both polymer and ceramic. Many of the inks in this thesis

are developed in house or modified. The general process usually starts with spin coating

or drop casting the material to see how it behaves and often making devices by spin

coating before moving to inkjet. A block diagram showing the general route to making

inkjet devices is shown in Figure 3-12.

---

[6] Often printed conductors are concerned with transparency for touch screens, solar cells, and displays, this conductivity and transparency is achieved with certain polymers and oxides. Pedot:PSS is a popular printable and transparent conductive polymer, too bad the conductivity is 10^3 S/m compared to 10^7 S/m for conductive metals. Conductive polymers or ceramics will not be used in this work due to the poor conductivity.
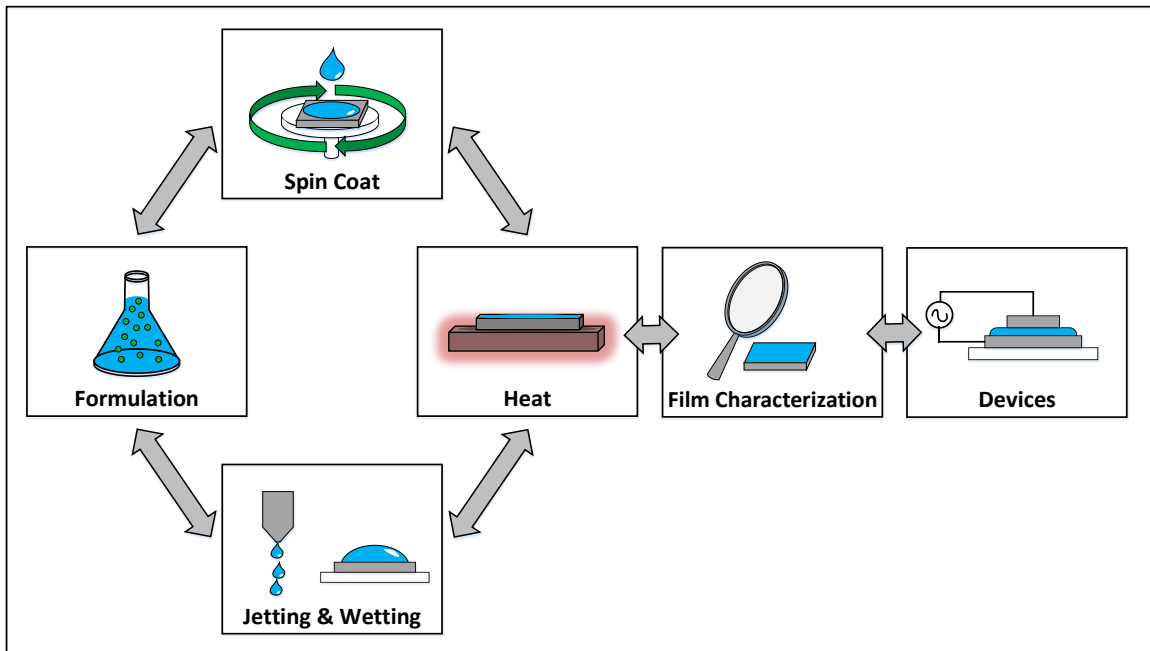
Figure 3-12: Inkjet Process Development

It is an iterative process involving formulating the ink for jetting and wetting on the

substrate. Modification of the substrate is often necessary by UV ozone or plasma

treatment and/or using a coating. Next, the films are annealed and characterized by

microscopy, profiled for thickness/roughness and x-ray techniques are used to see the

structure of the thin films. Finally, devices can be fabricated and measured; often taking

us all the way back to formulation step to improve the results.

Chapter 4 - Inkjet-printed Alumina for RF MIM Capacitors

The literature review in Chapter 2 showed that there are several relevant reports in two different research camps: traditional vacuum deposition of alumina for RF MIM capacitors and spin-coated sol-gel derived alumina for thin film transistors. The current work utilizes the sol-gel approach, moves it forward to inkjet printing, and applies it to RF MIM capacitors for the first time. Inkjet-printed alumina has been used for RF MIM capacitors, but both of the previous reports use micron-sized particle ink [40],[41]. The main problems with micron-sized particle ink are particle aggregation leading to nozzle clogging and rough micron-thick films with low capacitance density. The sol-gel approach solves these issues, since it is particle free and capable of forming thin (<100nm) layers. The existing literature reflects two prevalent precursors for making alumina sol-gel solutions: aluminum chloride and aluminum nitrate. To begin with, spin coating was used to test the film quality of both precursors, since spin coating is faster and less complex than inkjet. Quality films were formed with both precursors, although aluminum nitrate proved to be much more stable and easier to work with. Aluminum nitrate sol-gel was moved to inkjet printing. With viscosity modification and coffee ring suppression, ~100nm uniform inkjet-printed films were achieved. The printing process was integrated into an RF fabrication process using photolithography to create the RF MIMs with an airbridge. The RF MIMs are a useful demonstration as well as a method to completely characterize the sol-gel material as a function of frequency, temperature, and bias, which has never been reported in detail. A printable alumina dielectric is of interest to the RF community, and this comprehensive study will also be valuable for

those working in the competitive field of solution-processed dielectrics for thin film

transistors.

4.1   Initial spin coat trials with aluminum chloride precursors

The first report of sol-gel alumina as a transistor dielectric came in 2011 from the highly

cited paper of C. Avis et al. [34]. There have been several reports using a similar spin-

coating recipe [35],[36],[86] and solvent system with ethylene glycol and acetonitrile.

The experimental method employed in the current study is loosely based on these

reports. The final annealing temperature is investigated but the base recipe of ethylene

glycol/acetonitrile in a 65/35 volume ratio and a 2500 RPM spin speed with initial drying

at 70°C for 5 minutes and then 90°C for 5 minutes remains consistent in this section.

Although the end goal is to inkjet print the devices, spin coating is first deployed to

quickly screen the material and processing conditions. To better understand the

decomposition of the solution to alumina, a thermal gravimetric analysis (TGA) was

completed (see Figure 4-1). The TGA provides information about the temperature

regions where mass loss occurs. From the curve in Figure 4-1 it can be speculated that

all of the solvent evaporates by 150°C. In the zoomed in view in Figure 4-1(b),

decomposition to form aluminum oxide up to 400°C is then likely. The final

decomposition reaction is given in equation 4-1, although there are intermediate steps

detailed in [87].

$$AlCl_3\ 6H_2O_{(aq)} \xrightarrow[Decomposition]{\Delta} \frac{1}{2}Al_2O_{3\,(s)} + 3HCl_{(g)} + 4.5H_2O_{(g)} \qquad \text{4-1}$$
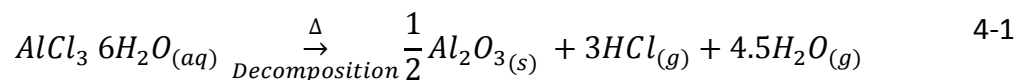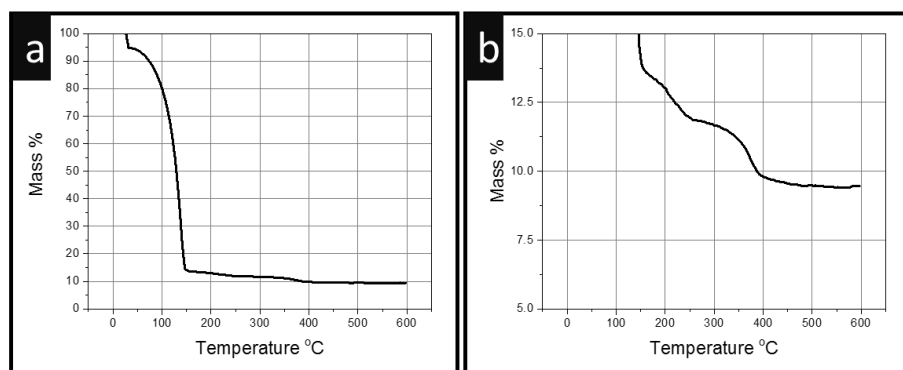
Figure 4-1: TGA of 0.4M aluminum chloride hexahydrate in 65% ethylene glycol and 35% acetonitrile by volume[7]

In the spun films, there is a large compaction after annealing from 200°C to 400°C. The

compaction can be seen in Figure 4-2(a), where a fairly linear trend in thickness with the

number of spins is also visible. Interestingly, the samples that were annealed at higher

temperature show high dielectric dispersion at low frequency, as shown in Figure 4-2(b).
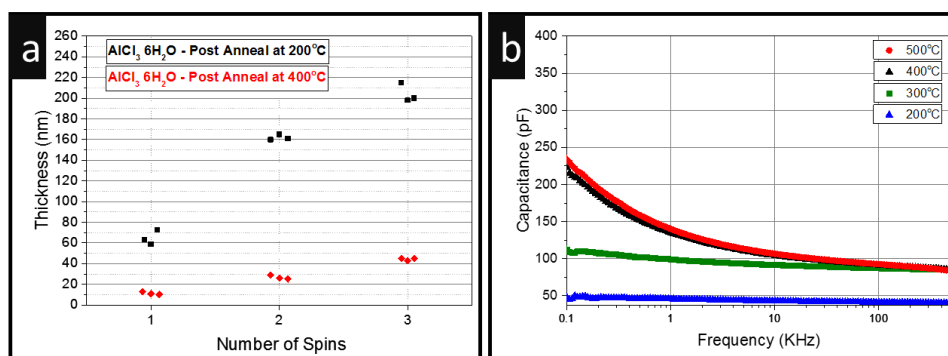
Figure 4-2: (a) Number of spins versus thickness of films on silicon substrates (Zygo interferometer). Aluminum hexahydrate 0.4M solutions with five minutes of ultraviolet ozone treatment before each spin. (b) Capacitance versus frequency of spin-coated capacitors at different annealing temperatures. Two layer spin coat on silicon, with aluminum top contacts. All capacitors have an area of 0.0675 mm². Measured at 25°C, with a 1-volt AC signal.

Films annealed at 200°C show little dispersion and a lower capacitance (due to being

thicker, ~160nm) while the 300°C, 400°C, and 500°C are thinner (~30nm) with increasing

---

[7] It should be noted that due to significant solvent evaporation at room temperature before starting the TGA analysis, the final weight percent remaining is higher than the amount we started with. Nonetheless, information about temperature and decomposition is provided. Measured with a TG 209 F1 at 10°C/min.

dispersion. All films are extremely smooth (<2nm RMS roughness), as measured by atomic force microscopy (AFM). Energy dispersive X-ray (EDX) analysis was conducted on the films to find the atomic concentrations. Interestingly, even a sample annealed at 200°C shows very little chlorine (4.6%) and carbon (6.2%); the oxygen and aluminum concentrations were near stoichiometric at 56.8% and 32.4%, respectively.

Element	Atomic %
C	6.2
O	56.8
Al	32.4
Cl	4.6
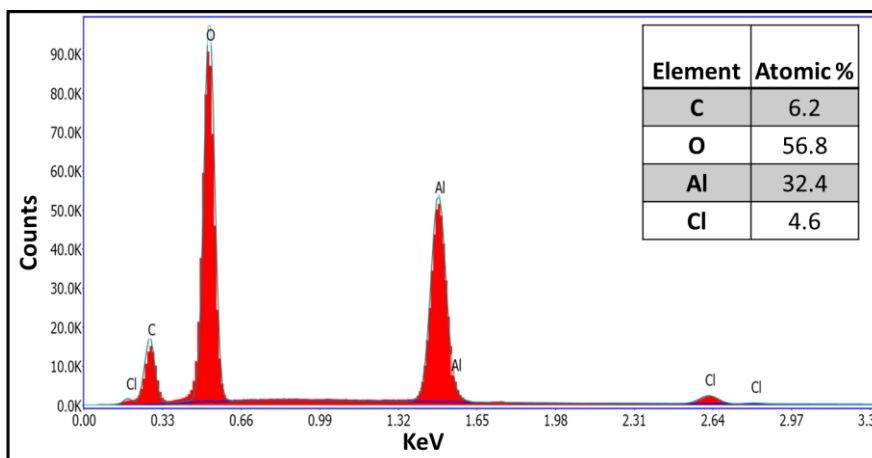
Figure 4-3: EDX analysis of film annealed at 200°C

Due to the EDX data and both the low dispersion and leakage current of the capacitors at 200°C annealing, it was thought that the ultra violet ozone (UVO) exposure may be providing the energy for decomposition. However, after inspection by XPS analysis we found that there was only a small change in the films with UV exposure reaching only 40% aluminum-oxygen bonding. The rest of the bonding is majority aluminum hydroxide. The XPS analysis of the oxygen peak is shown in Figure 4-14 with 2- and 20-minute UVO samples.
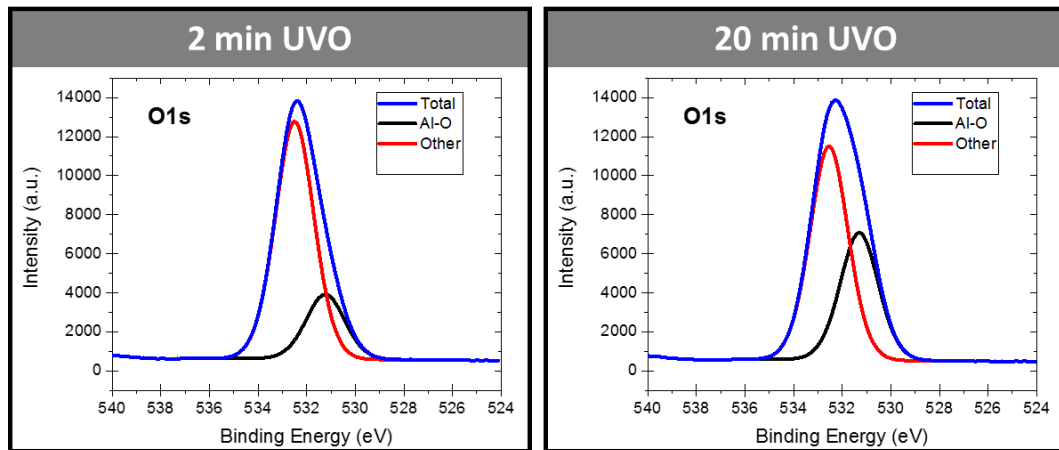
Figure 4-4: XPS results of oxygen peak for 200°C annealed AlCl$_3$ 6H$_2$O spin-coated films

With the verification of the large hydroxide component in the low temperature alumina

and the results from the TGA showing mass loss all the way up to 400°C, high

temperature annealing of at least 400°C is likely necessary.

The dielectric dispersion in the 400°C capacitors is a serious concern. To understand the

reason for the dispersion, capacitors were measured on a hot chuck (see Figure 4-5).

Increased chuck temperature during measurement reduced the dispersion somewhat,

but it would again return after cooling. The quality factors are also less than 10 in Figure

4-5(b); this is poor, as the factors should be above 50 for alumina MIMs [31].
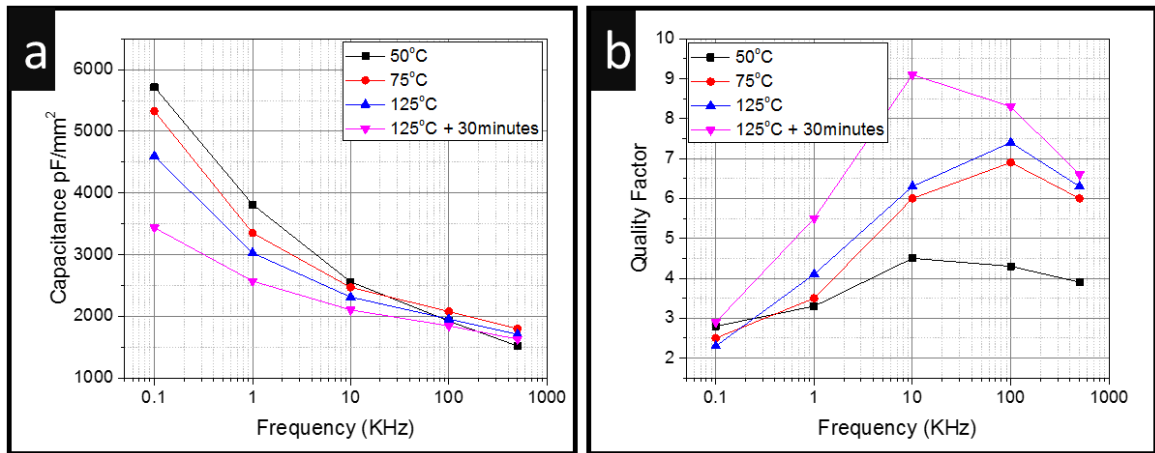
Figure 4-5: Effect of measurement temperature on dispersion: Spin-coated AlCl₃ capacitors on silicon, measured as a function of temperature. The devices were measured directly after a prebake at 150°C for five minutes (measured with 1V signal).

Alumina films were spun on gold-coated glass since the low conductivity of silicon could be a reason for the low quality factor capacitors. Both the low quality factors and the dispersion remain, despite the substrate change. The SEM images taken showed smooth films and gave reliable thickness measurements; see Figure 4-6. However, no structural information to explain the dielectric dispersion was revealed.
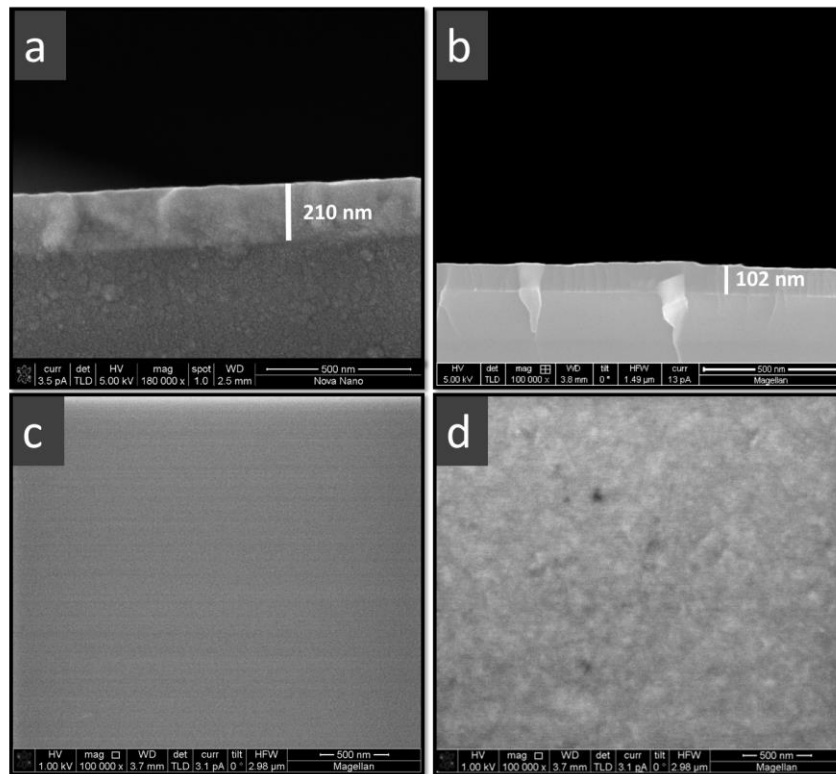
Figure 4-6: (a) Cross-section SEM image of 200^oC annealed spin-coated film on glass. (b) Cross-section SEM of a 500^oC annealed film on glass. (c) SEM top view of 200^oC film. (d) SEM top view of 500^oC film.

The annealing environment (O_2, N_2, Air) was studied given that it was thought that oxygen may aid in the decomposition of the film or create oxygen-rich or deficient films that would lead to some information about the dispersion. In Figure 4-7, all three samples (O_2, N_2, Air) show near equal amounts of low frequency dispersion. It is believed that water adsorption of the films is likely the cause for the dispersion. Porous alumina is well known commercially for its use in capacitive humidity sensors [88] and sol-gel alumina humidity sensors have been made during research [89]. This explanation is consistent with the data that heating the films temporarily reduced the dispersion and dielectric constant, since water partially came out of the films with heat exposure.
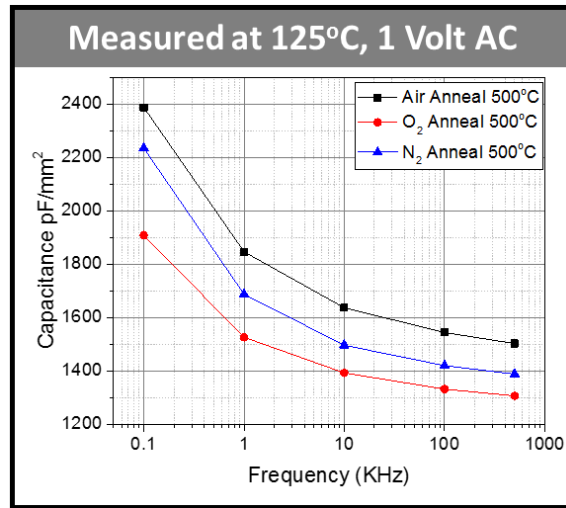
Figure 4-7: Effect of annealing environment (Air, O_2, N_2), 0.4M solution spun at 2500 RPM on sputtered gold, annealed at 500^oC, LCR meter signal voltage. Measured at 125^oC for reduced dispersion.

There are reports of nano-porosity (less than 30nm) in thin film chloride based sol-gel oxides reported in [90], and characterized in [91] by transmission electron spectroscopy (TEM). The explanation provided is that during the decomposition, it is HCl that creates bubbles and ultimately nano-pores in the film. The situation is depicted in Figure 4-8(a), where more porous films are made by spinning several layers to create a thick film and finally compacting them all together at 400^oC.
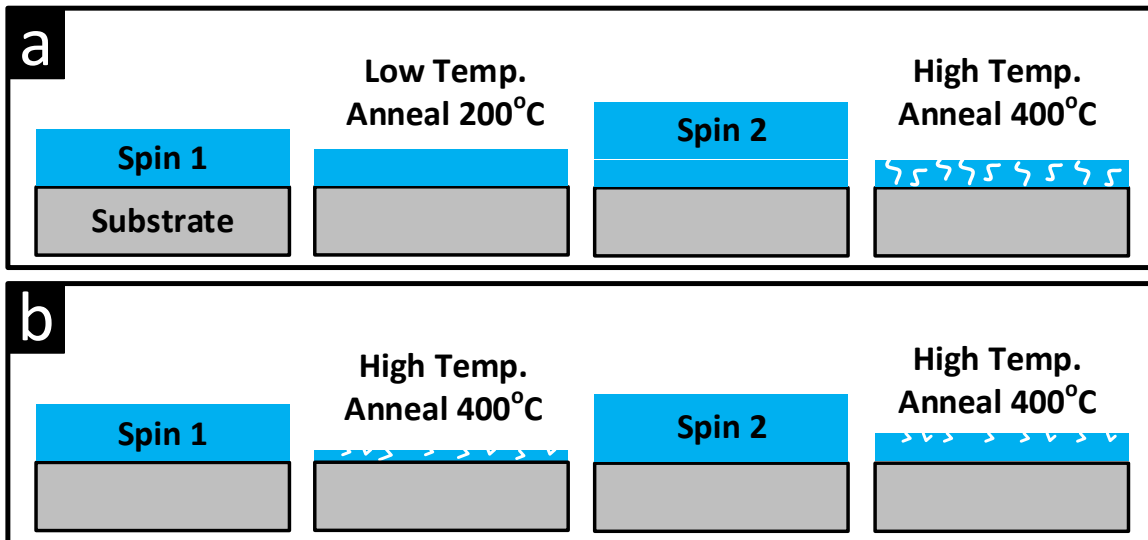
Figure 4-8: (a) Possible explanation of creating nano-pores in the film with improper thermal processing. (b) Possible method for creating a less porous film with high-temperature heat treatment between multiple spins.

Alternatively, films were fabricated using the situation in the less porosity case depicted in Figure 4-8(b). The films were heated at 70°C, then 90°C, and finally a ramped up 400°C after each spin, which may cause porosity; nonetheless, it is subsequently filled in by the next spin. The final film contained pores, mostly in the top layer. Capacitors were fabricated using the low dispersion method, and even at room temperature they had a fairly flat frequency response, as shown in Figure 4-9(a). The best capacitors made with this low dispersion method utilized three spins and a 400°C annealing step between each spin. The capacitance density change from 100Hz to 500KHz is only 4%, while the estimated dielectric constant is 6.2.
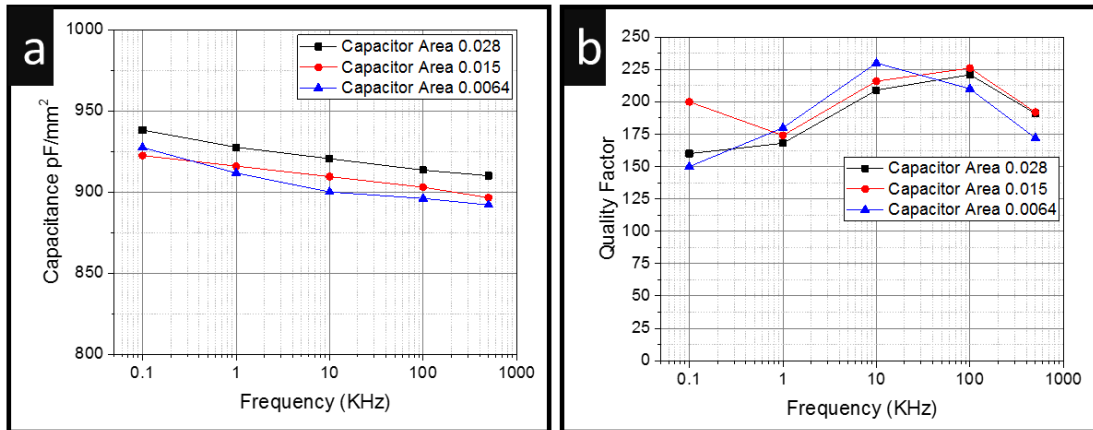
Figure 4-9: Low dispersion capacitors with high temperature annealing steps between layers, 0.4M solution spun on 500nm of gold-coated glass, measured at 25°C, with a 1V signal. Aluminum contacts are 250nm thick. Films are ~60nm thick.

The Qs of the devices are around 200 at low frequency, as shown in Figure 4-9(b). This is

a great improvement in comparison to the Qs of less than 10 in the high dispersion case,

although the stability of the aluminum chloride precursors remains an issue.

Furthermore, $AlCl_3$ $6H_2O$ was even stored under vacuum to increase the shelf life. After

a few weeks, however, the precursors could not be used to make stable sol-gel

solutions. As shown in Figure 4-10, precursors only two weeks old would produce cloudy

solutions with a two-phase liquid. The precursors could likely be used without issue if

they were stored and used in an inert glove box.
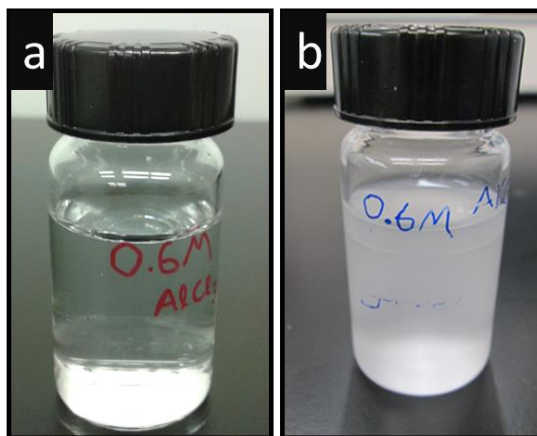
Figure 4-10: (a) Fresh AlCl₃ 6H₂O precursors used to make a clear sol-gel solution 65/35 Ethylene Glycol/Acetonitrile. (b) Cloudy and phase-separated solution, made two weeks after opening the precursor container.

4.2 Initial trials with aluminum nitrate precursors

Compared to aluminum chloride, aluminum nitrate was much more stable to work with.

Aluminum nitrate nonahydrate precursors as well as sol-gel solutions were both found

to be stable over several months of storage in an ambient environment. Uniform spin-

coated films could be made using the common sol-gel solvent of 2-methoxyethanol (2-

ME). A TGA was carried out to find mass loss versus temperature, as shown in Figure

4-11(a). The majority of the mass is lost by 125°C, which is the boiling point of 2-ME.

From the zoomed in view in Figure 4-11(b), the mass slowly decreases all the way down

to 400°C, at which point has likely decomposed to alumina. The decomposition reaction

is described by equation 4-2 [92].

$$Al(NO_3)_3 \; 9H_2O_{(aq)} \; \underset{Decomposition}{\overset{\Delta}{\rightarrow}} \; \frac{1}{2}Al_2O_{3(s)} \; + 2HNO_3 + \frac{1}{2}O_{2(g)} \qquad \text{4-2}$$

$$+ \frac{1}{2}N_2O_3 \; + 8H_2O_{(g)}$$
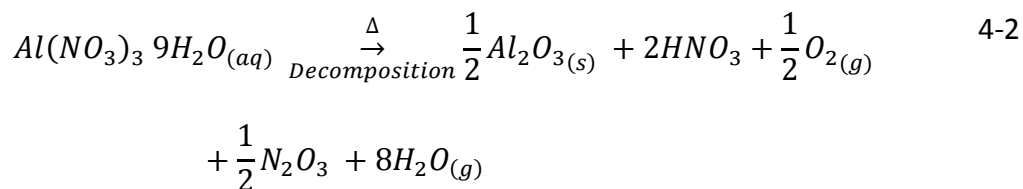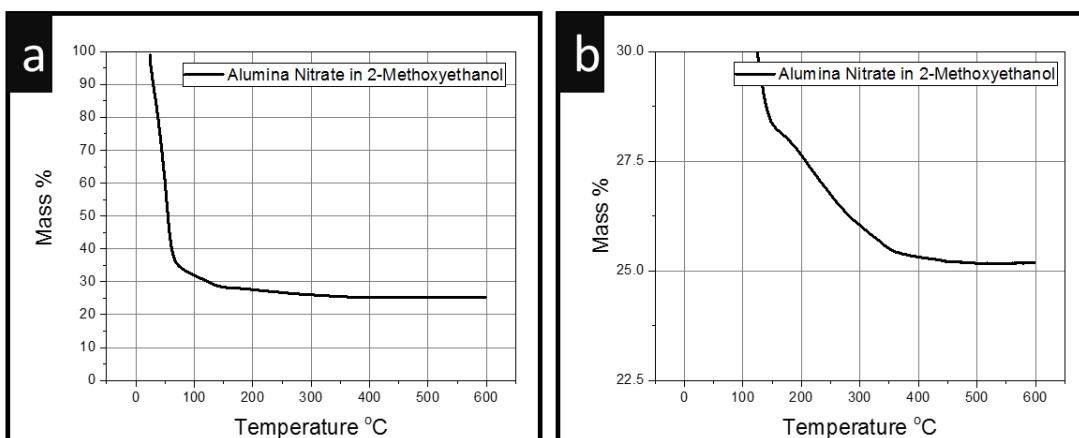
Figure 4-11: (a) TGA analysis of aluminum nitrate 0.4M in 2-methoxyethanol. (b) Zoomed in view.

Films were built up by spin coating three layers on silicon to find the thickness; see

Figure 4-12. Capacitors were made on gold-coated glass substrates, with top contacts

that were sputtered through a shadow mask with titanium (10nm) and gold (500nm).

The thickness of the three layers was nearly the same on gold-coated glass (i.e. around

110nm). A linear trend is observed in Figure 4-13, and the dielectric constant can be

estimated to be 6.4.
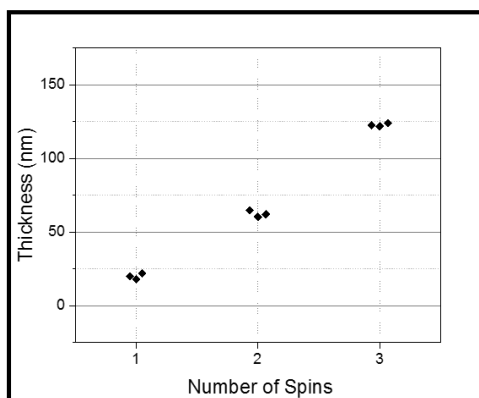
Figure 4-12: Spin-coat thickness measurements 0.4M Al(NO₃)₃-9H₂O in 2-Methoxyethanol on silicon. Spin speed is 2500RPM for 40 seconds. Each layer is annealed at 70°C for 5 minutes, 90°C for 5 minutes, and ramped up from 200°C to 400°C for 10 minutes for all layers, followed by a final 400°C anneal for 2 hours.

This was compared with an ALD sample with 98nm deposited film, which showed a Dk

of 9.2. Estimations were based on the basic parallel plate capacitor; see equation 4-3.

$$Capacitance = \frac{\text{Dk } \epsilon_o \ Area}{thickness} \ , \quad \epsilon_0 = 8.854E^{-12}F/m \hspace{3em} \text{4-3}$$
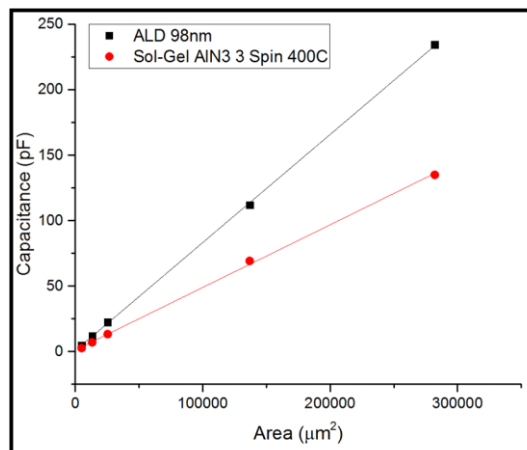
Figure 4-13: Capacitance versus capacitor area for both ALD and spin-coated sol-gel films.

The estimated Dk of 6.2 for the sol-gel derived alumina is low (~70%) [17]; however, it is

similar to other sol-gel reports in the literature [38],[36],[34]. Hu [37] used aluminum

nitrate precursors aimed at making dense films and investigated 550°C annealing, yet

reported a similarly low dielectric constant. The lower dielectric constant has been

attributed to a lower density of the film in comparison to ALD, which is somewhat

expected based on the previous reports. From XPS analysis (see Figure 4-14), there is an

undetectable amount of nitrogen left in the films after the 400°C anneal, which

indicates that the nitrate precursor has decomposed. Figure 4-14 shows the ratio of Al

to O is 1.57, nearly stoichiometric Al_2O_3, which would ideally be 1.50.[8] The single

---

[8] A carbon correction was used to increase the accuracy of the analysis described in [93],[94].

aluminum peak ~74.2 Ev confirms the formation of alumina. The oxygen peak at ~531.0

eV is recognized as O^{-2} in Al_2O_3, which is attributed to 74% of the oxygen bonding. The

smaller oxygen peak at ~532.3 eV is mostly associated with aluminum hydroxide ~26%.

A similar hydroxide component is also shown in alumina sol-gel films annealed at 500°C

by Nayak et al. in [36].
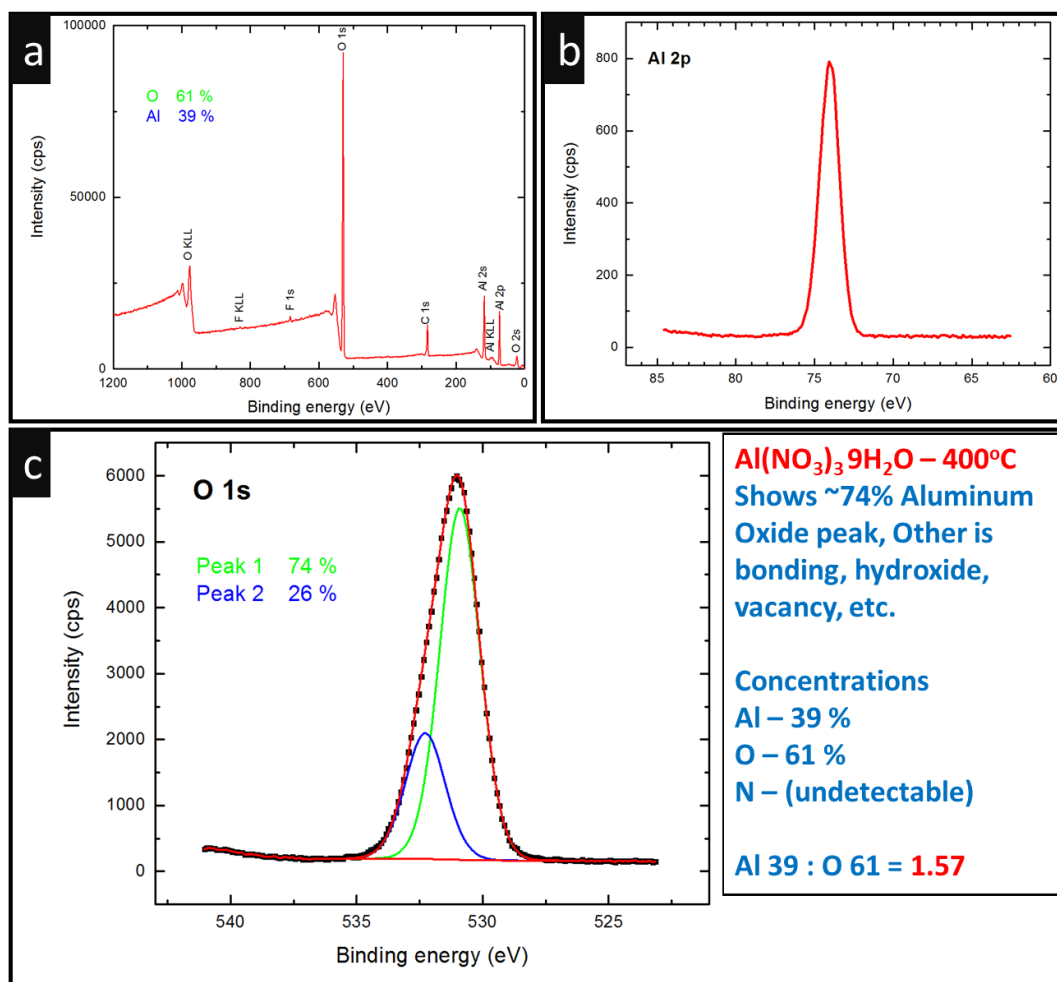
Figure 4-14: XPS analysis of Al(NO₃)₃-9H₂O 9H₂O in 2-ME annealed at 400°C.

The electrical characterization of these spin-coated films has a leakage current of $1x10^{-8}$

A/cm at 1MV/cm, as shown in Figure 4-15. The leakage is an order of magnitude worse

than the ALD films, but it is still good compared with previous sol-gel literature (see

Table 2-3). As shown in Figure 4-16(a), there is low dispersion in the dielectric from 100

Hz to 500KHz; the change is less than 3%. The ALD films have higher capacitance density

but show similar low dispersion of ~2%. The quality factors of the films are around 200

for the sol-gel capacitors and 250 in the case of ALD, as indicated in Figure 4-16(b);

these quality factors compare well. In Figure 4-17(a), capacitors have been tested

against voltage bias with negligible change and similar performance to ALD grade films.

No significant change is seen in the quality factor as a function of bias from Figure

4-17(b).
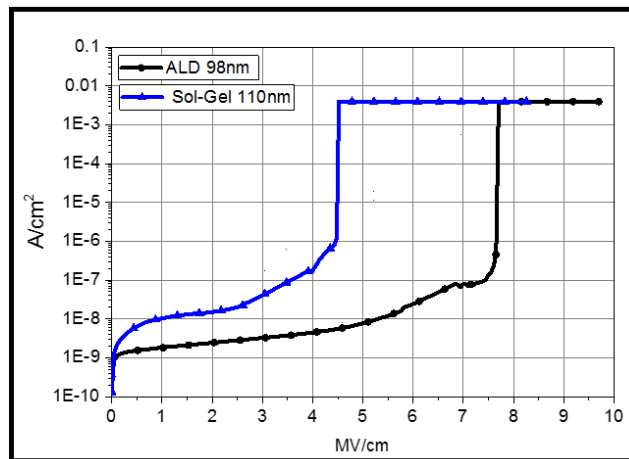
Figure 4-15: Typical leakage current comparison of ALD Al_2O_3, and 400^oC spin-coated AlN_3 $9H_2O$ 2ME sol-gel film on gold-coated glass, three spins ~110nm thick films with 500nm Ti/Au top electrodes.
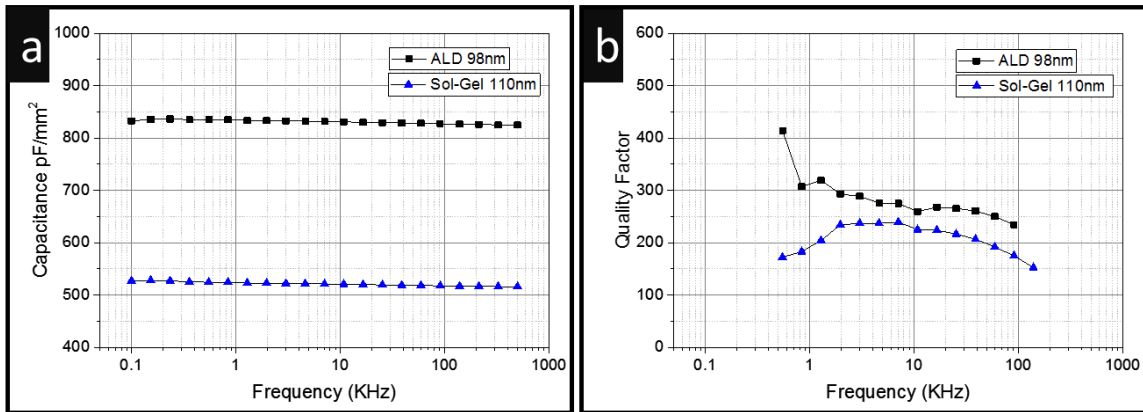
Figure 4-16: (a) Capacitor Low frequency testing with frequency. (b) Quality factor.
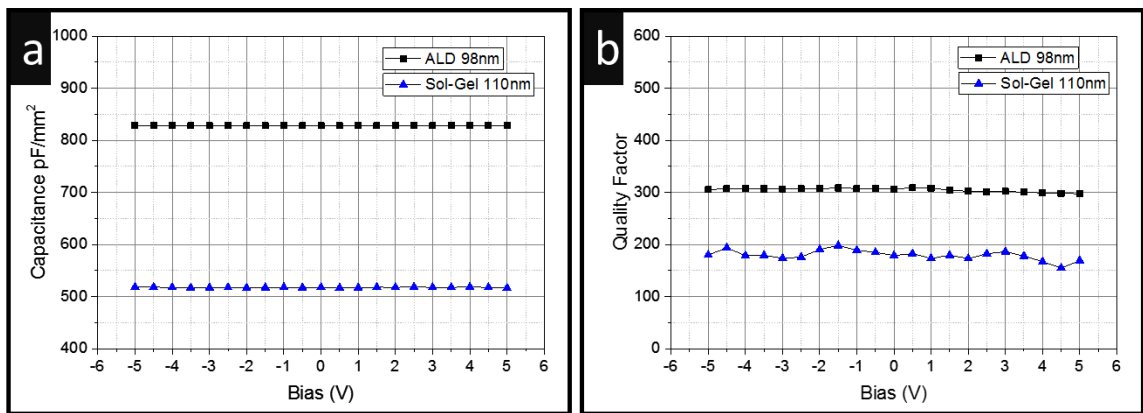
Figure 4-17: (a) Capacitor ias testing. (b) Quality factor.

Although the films show lower performance than ALD grade films, this can be expected from a solution process compared to a mature high vacuum process. The aluminum nitrate precursors turned out to work well, and were much more stable in environmental condition than aluminum chloride. These promising results motivate working towards inkjet printing of these aluminum nitrate precursors.

4.3   Inkjet RF MIMs process

This work is focused on developing a process to print an alumina dielectric and integrate it with a more traditional RF MIM fabrication process using photolithography. The inkjet

printing of alumina is described first; see Figure 4-18(a). The information presented

includes viscosity, surface tension modification, jetting characterization, coffee ring

suppression, and thickness and uniformity of the films.
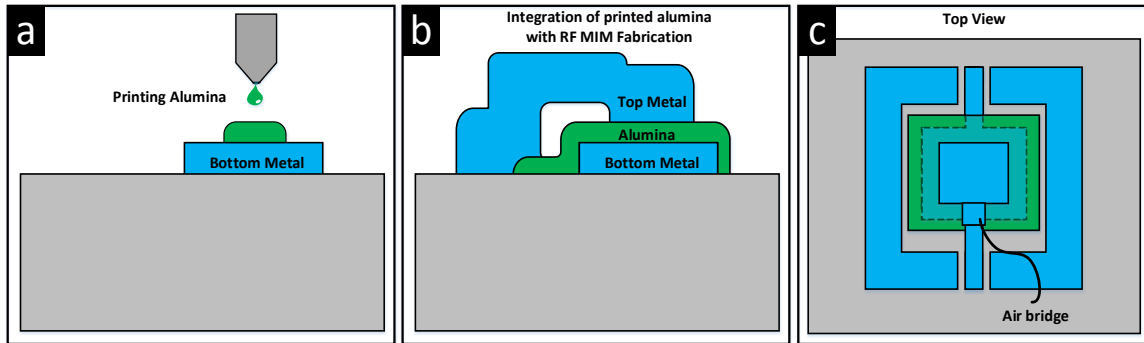
Figure 4-18: (a) Inkjet printing of alumina dielectric. (b) Integration of the alumina in an RF MIM fabrication process with an airbridge. (c) Top view of the final MIM capacitor.

After this section purely dedicated to inkjet printing, the entire RF MIM fabrication

process is covered; see Figure 4-18(b) and (c). The thick metal layers and airbridges that

are commonly used to improve quality factors and reduce leakage current in RF MIM

fabrication are also employed here. This is a photolithography process, and some

challenges related to patterning thick metal and etching are covered. A novel process

that includes low temperature lift off of amorphous silicon and XeF_2 etching to create an

airbridge is also described in detail.

4.4   Printing of alumina

In the current work we utilize a Dimatix 2831 inkjet printer with a 10pL cartridge. Full

details of the process (including ink recipes and all parameters) can be found in

Appendix 3. It proved difficult to inkjet print on the gold surface directly. A thin layer of

poly-4 vinyl phenol was spun on top of the gold (~5nm) with a measured surface energy

of 61 dyne/cm. An optimized UVO treatment was then applied for 150 seconds, as the

ink completely wets on this surface. It was found that the 2-ME solution had significant capillary-driven spreading and high coffee ring staining. Heating the substrate was not effective in making smooth uniform films, as seen in Table 4-1.

Table 4-1: Microscope images of initial tests, printing 500um squares with 0.8M AlN$_3$ 2-ME solution on thin PVP (~5nm) coated gold (500nm) with 150 seconds of UV ozone treatment.
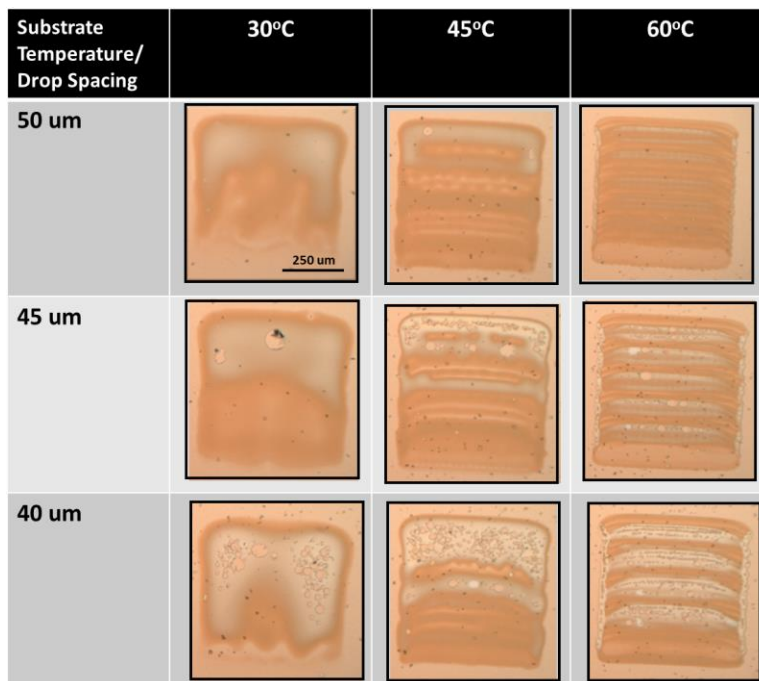
The ink tends to pool at the top of the printed squares, driven by evaporation and capillary flow. (These films are printed left to right and from top to bottom.) By increasing the temperature, the fluid partially dries and fully covers the square; however, coffee ring staining leads to highly non-uniform films. At lower drop spacing (which entails more ink), the single printed layer thickness (>100nm) causes films to crack and explode during annealing. Different solvents were attempted to alleviate these issues, including ethanol, 2-propanol, 1-butanol, and 2-butanol. In the end, ethanol gave the best results as its higher volatility limited the capillary-driven

spreading, which in turn reduced the coffee ring effect. As was done by Soltman et al.

[84], the droplets were printed and images were taken with a Zygo interferometer to

investigate coffee ring staining (see Figure 4-19). Profiles of each of these drops are

provided in Figure 4-20.
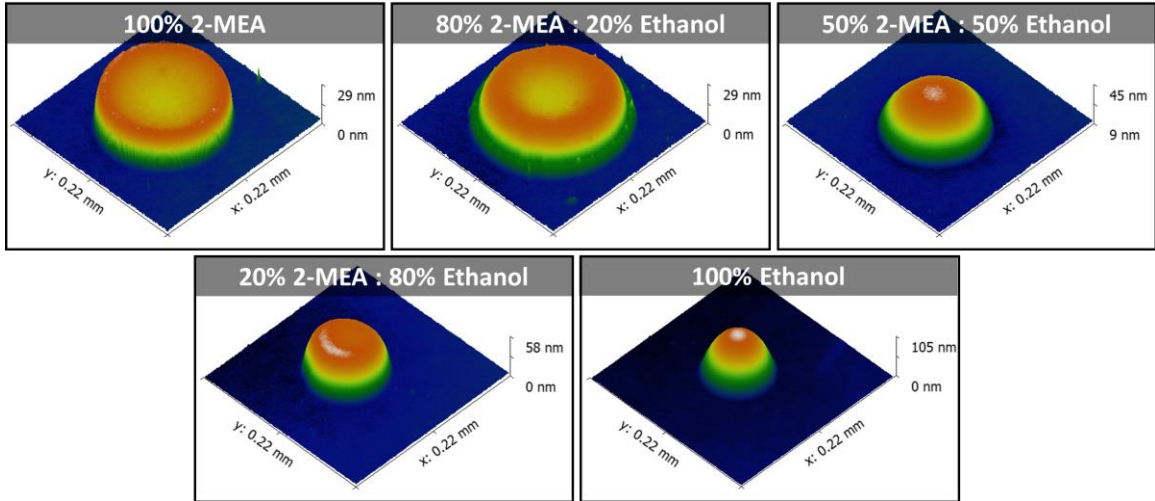
Figure 4-19: 0.8M concentration Al(NO₃)₃ 9H₂O printing of single 10pl droplet on a PVP-coated gold substrate with 150 seconds of UV ozone treatment (AlOₓ droplets imaged after annealing at 400°C).
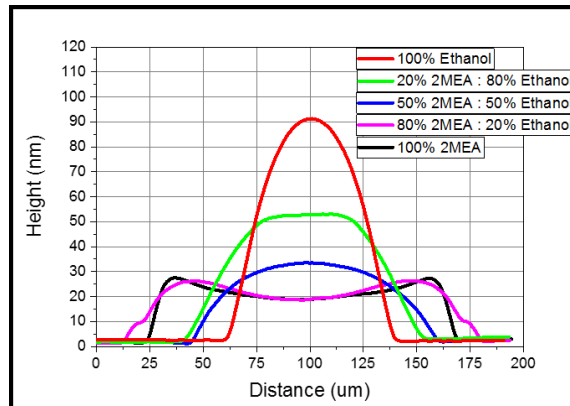
Figure 4-20: Profile of droplets with different 2-methoxyethanol to ethanol ratios.

The effect of ethanol on reducing both the coffee ring stain and the spreading of the

droplets is apparent. A 50/50 mix of ethanol and 2-MEA was chosen as the solvent for

the printing.

Films were then built up with printing in a similar fashion to the spin coating of the previous section: ~35nm layers were printed three times with a 400°C annealing step in between to form ~110 nm films. A profilometry scan of a printed ~110nm film that is fairly uniform at the centre can be seen in Figure 4-21(a).
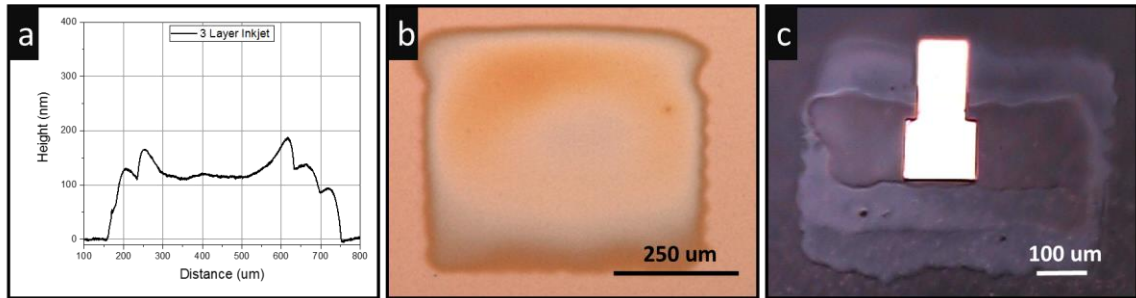
Figure 4-21: (a) Profile of the inkjet printed film. (b) Microscope image of the printed film. (c) Three-layer printing over top of patterned gold bottom metal and glass.

The microscope image of a printed square in Figure 4-21(b) clearly indicates improvement from Table 4-1. Figure 4-21(c) is a microscope image showing how three layers can be printed over glass and the patterned gold as used to fabricate the RF capacitors. The gold surface is very smooth, with 2.8 nm of RMS roughness from the AFM scan in Figure 4-22(a). The alumina films printed on top of the gold show only 0.4 nm of RMS roughness; see Figure 4-22(b).
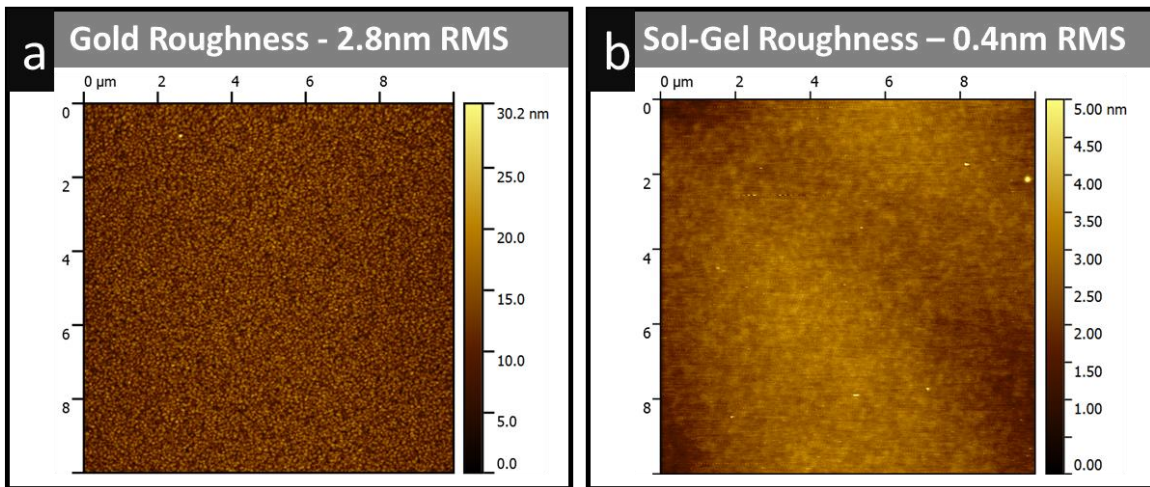
Figure 4-22: AFM scan showing 0.4nm of surface roughness.

The final ink used a 50/50 ethanol to 2-ME ratio with a 0.8M concentration. While these low viscosity solvents alone had a viscosity of 1.3 cp, the addition of the precursor raised the viscosity into a much better range of 7.0 cp for 0.8M, as shown in Figure 4-23.
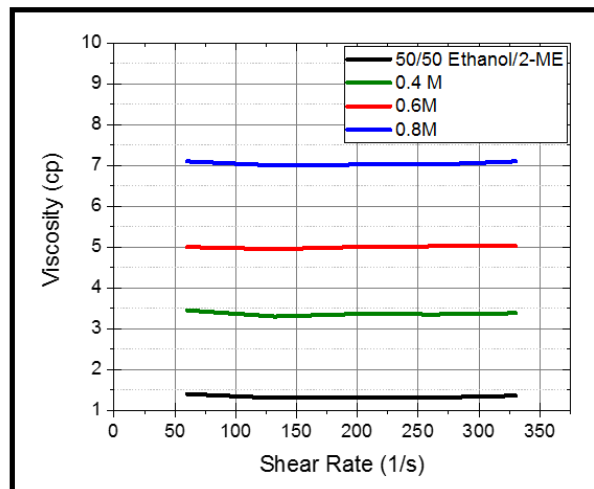
Figure 4-23: Viscosity of pure solvent and with the addition of different concentrations of aluminum nitrate precursors.

This viscosity is in a good range for inkjet printing, and there was no evidence of shear thickening or thinning behaviour from Figure 4-23. The characteristics of the ink are highlighted in Table 4-2.[9]

Table 4-2: Characteristics of Al(NO₃)₃ 9H₂O ink with 50/50% by volume ethanol and 2-ME solvent and 0.8M concentration at 25ᵒC, using the 10pL cartridge with 21um diameter orifice at 11m/s velocity.

Viscosity (cp)	Surface T. Dyne/cm	Density (g/cc)	Drop Mass (ng)	Ohnesorge (Oh)	Reynolds (Re)	Weber (We)	Capillary (Ca)
7.0	28.3	1.04	6.8	0.28	34	93	2.7

4.5   Inkjet RF MIM capacitor fabrication

Due to the leakage current that develops at the edges of the bottom metal, an airbridge is commonly used for RF capacitors [95],[30]. An airbridge is especially important for an inkjet-printed film where de-wetting at the edge of the bottom metal is observed, not only causing leakage but completely shorting the devices.
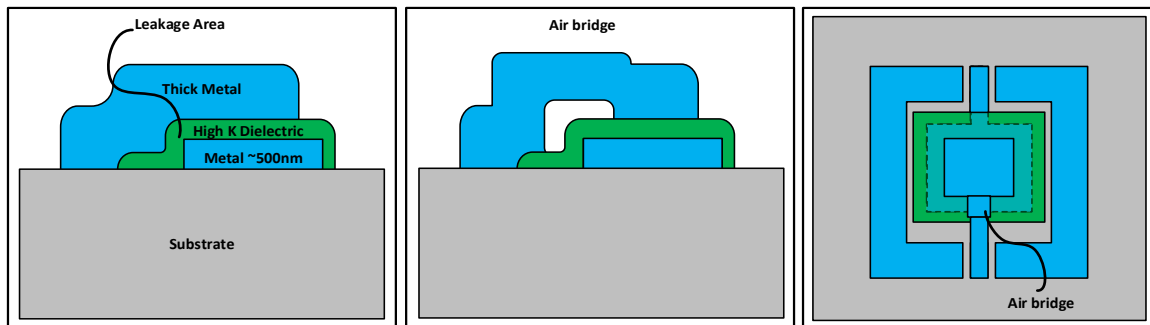
Figure 4-24: Airbridge fabrication for RF MIM capacitors.

---

[9] Viscosity was measured with a Brookfield Rheometer DV3T, surface tension was measured with a Kruss DSA 100, and drop mass was calculated by taking the average weight of 8 million ejected drops.

The fabrication process steps are shown in Figure 4-25, and a detailed description of all of the steps (including sputtering power and recipes for spin coating the resist) is included in Appendix 3.
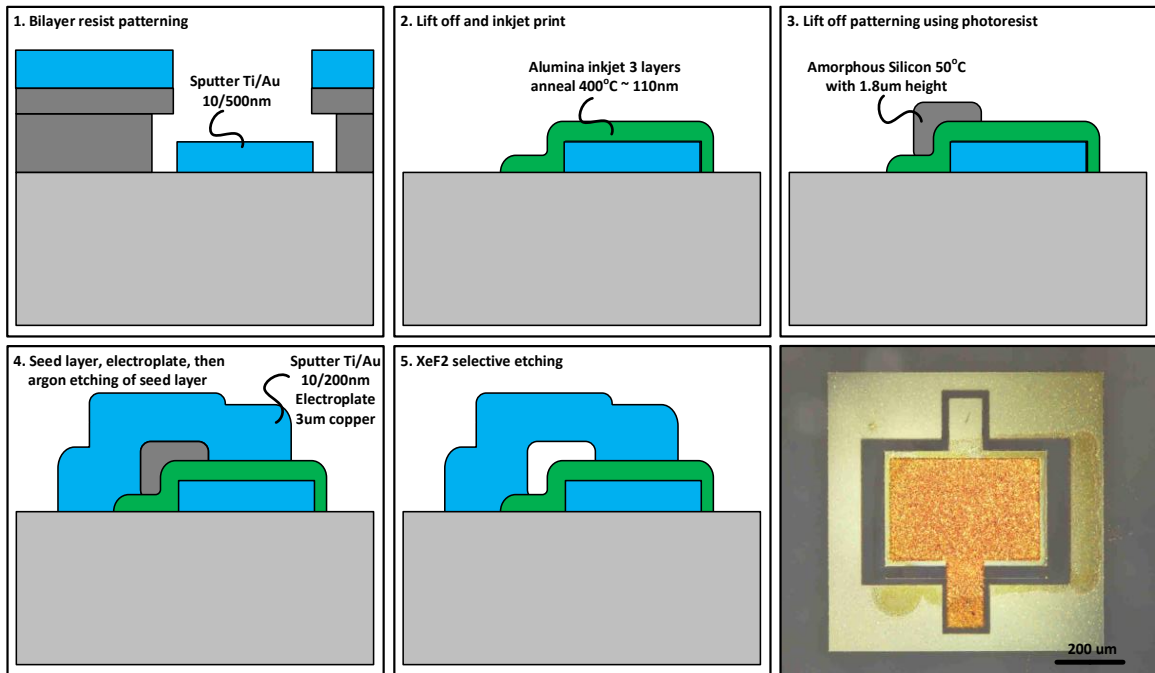
Figure 4-25: Fabrication steps for RF MIM capacitors

The jagged edges of the patterned bottom metal were a concern for the lift off technique. Alternatively, dry etching caused "bat ears" (i.e. tall spikes at the edge of the gold patterns) that would short all capacitors to appear; see Figure 4-26(a). This effect was greatly reduced from 500nm to 50nm bat ears by using a titanium coating on the resist, as described in [96].
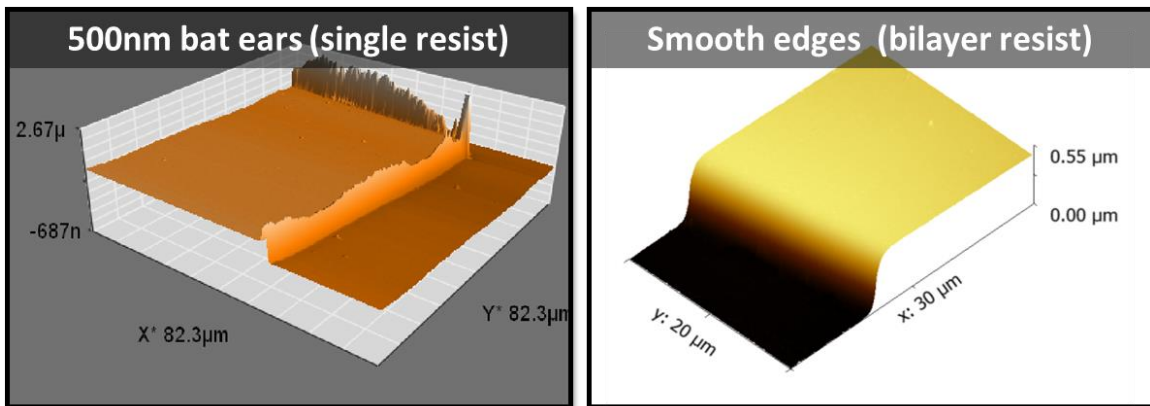
Figure 4-26: AFM scans of "bat ears" on conductors, which are fixed using a bilayer resist

While the titanium coating helped, a bilayer resist technique completely solved the

issue. When resist LOR 7B was spun on the bottom and AZ ECI 3027 (Microchem) on the

top, completely smooth edges were achieved, as shown in Figure 4-26(b). A photo of

the bilayer resist with appropriate exposure and development times can be seen in

Figure 4-27(a).
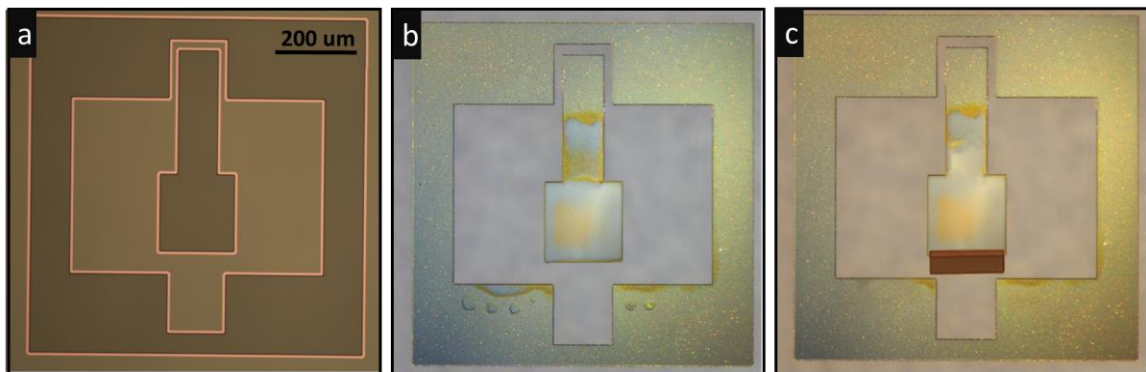
Figure 4-27: (a) Bilayer resist showing undercut after development. (b) Inkjet-printed film after 400°C anneal. (c) Amorphous silicon sacrificial layer for airbridge.

Finding the appropriate sacrificial layer and etching process to remove the layer from

under the airbridge proved to be rather challenging. This is because many etchants and

even photo-developers eat aluminum and also damage the thin Al_2O_3 film, which causes

excessive leakage current in devices. Photoresists and SU8 were first attempted as

sacrificial layers, but in the end a sacrificial layer of amorphous silicon (a-Si) worked the

best. A lift-off process with amorphous silicon was used by depositing at an unusually

low temperature (50°C). This was necessary so that the photoresist would not be hard-

baked to the wafer and the resist could easily be removed with acetone. The a-Si has

the added advantage that it can be selectively etched away with XeF_2 gas without

damaging any of the other materials. A picture of the a-Si during the fabrication process

can be seen in Figure 4-27(c). An SEM image of the alumina layer along with the

airbridge can be seen in Figure 4-28(a) and (c). There is a clear 1.8um gap under the

airbridge, and the a-Si has been removed by the XeF_2 etching. From the focused ion

beam (FIB) SEM image at high magnification, there are few details about the alumina

structure, although a ~120nm thickness of the layer is shown. The thin ~15nm titanium

layer can be vaguely seen below the top gold.
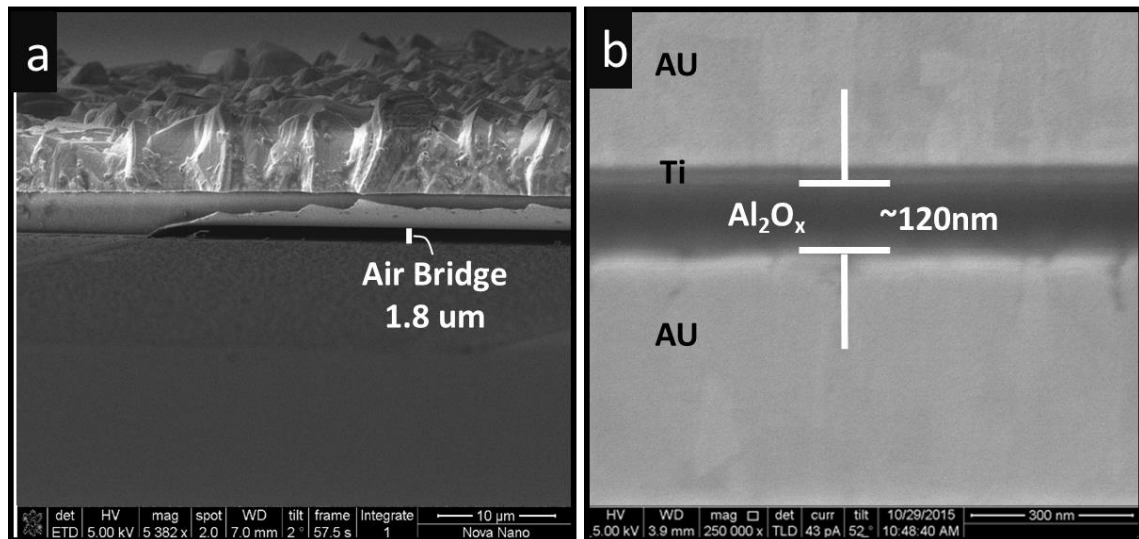
Figure 4-28: (a) SEM image of airbridge. (b) FIB-SEM image of alumina film.

4.6   Inkjet capacitor measurements

The printed devices had comparable performance to their spin-coated relatives. The leakage current of the capacitors is excellent, with better than $2x10^{-9}$ at 1MV/cm. The greatest concern for the printed devices is perhaps the variability in capacitor sizes that is caused by the fluctuation in film thickness.
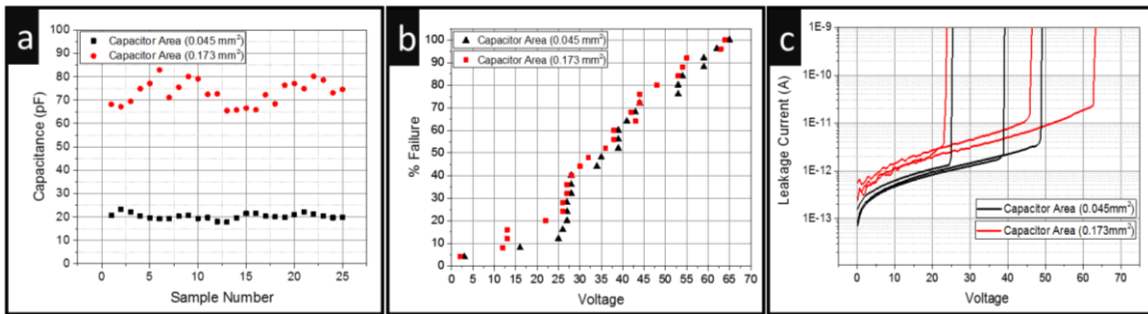
Figure 4-29: (a) Variation in capacitors. (b) Breakdown voltage. (c) Leakage current.[10]

There is a relatively large fluctuation in the capacitance values, as seen in Figure 4-29(a). The capacitance values for the 0.173mm^2 area devices have a standard deviation of 5.1 pF (7%), while the 0.045 mm^2 caps show a 1.2 pF deviation (6%). However, this is a new process and it is expected that with further improvement to the ink formulation and optimization of a uniform surface treatment, more uniform layers could be printed and the capacitance variation reduced. The breakdown fields for the capacitors are far from ideal with no predictable breakdown voltage. Nonetheless, most of the capacitors break above 20V, which is useful for many applications. Capacitance and bias were tested against measurement temperature.

---

[10] Note that these results were obtained on Ti/Au 10/500nm non-patterned bottom metal.
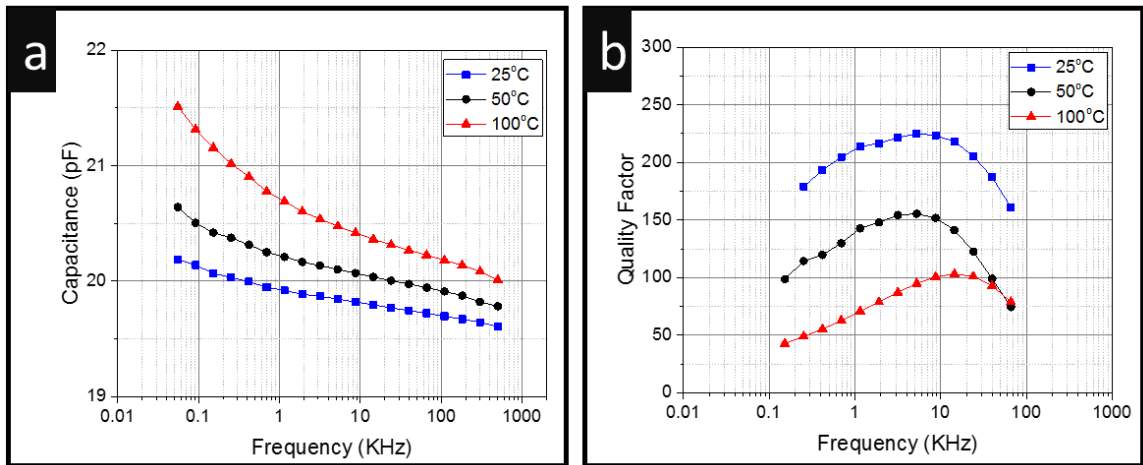
Figure 4-30: (a) Low frequency capacitance testing. (b) Quality factor.

There is a significant drop in the quality factor with temperature. While there is also a change in the ALD film, this change was less significant. The reason for this could have to do with the hydroxide component in the sol-gel films, although the understanding of this phenomenon would require further investigation. Nonetheless, quality factors in the range of 200 are excellent for an inkjet-printed film. There is some frequency-dispersion as well as a change due to temperature. The TCC at 100 KHz is calculated to be ~330 ppm/°C, which is comparable to sputtered films [31] and ALD films (further comparison with ALD films is shown in Appendix 4). The bias has been measured as a function of temperature as well; see Figure 4-31(a). While these measurements look flat, there is a small change as shown in the zoomed in plot in Figure 4-31(b). This change in capacitance can be normalized and plotted to find the voltage characteristics given from equation 4-4 [97].

$$\frac{C(V)}{C_o} = \alpha V^2 + \beta V + 1$$

<div align="right">4-4</div>
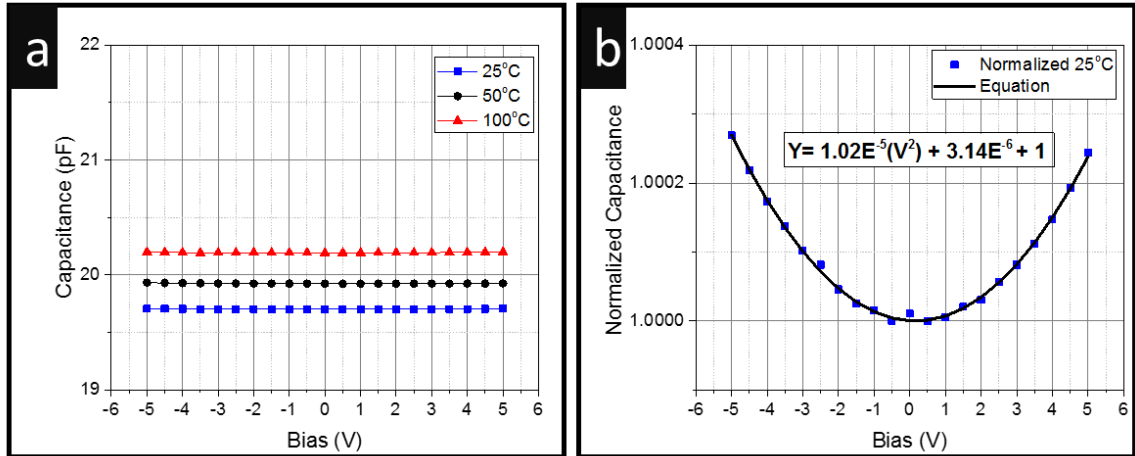
Figure 4-31: (a) Bias testing. (b) Normalized capacitance versus bias.

From the normalized plot in Figure 4-31(b) we find that α is calculated as 10.2 ppm/V^2

and β as 3.1 ppm/V. This shows slightly better voltage characteristics in comparison to

ALD [30]; however, it is important to bear in mind that the parameters are influenced by

capacitance density, which is higher in the ALD films. Further comparisons can be found

in Appendix 4. To the knowledge of the author, this is the first time that sol-gel alumina

has been characterized at high frequency. Measurements are obtained by taking the

measured S-parameters from the two-port network analyzer and then converting these

to Y-parameters and extracting the capacitance with the following equations [98]:

$$C = -\frac{1}{im\left(\frac{4}{Y_{11} + Y_{22} - Y_{12} - Y_{21}}\right) 2\pi f} \qquad \text{4-5}$$

$$Q = -\left(\frac{im(Y_{11} + Y_{22} - Y_{12} - Y_{21})}{re(Y_{11} + Y_{22} - Y_{12} - Y_{21})}\right) \qquad \text{4-6}$$

An electromagnetic simulation that was built with Ansoft High Frequency Structure

Simulator (HFSS) software compares well with the measured results, as shown in Figure

4-32. The simulation was run with 500nm of sputtered gold and 3um of copper top

metal. With a 120nm dielectric, Dk of 6.2 and a loss tangent of 0.005 (which was

extracted by taking the inverse of the low frequency quality factor [99]). The simulation

results and measurements have consistent self-resonance frequencies, capacitance, and

quality factors.
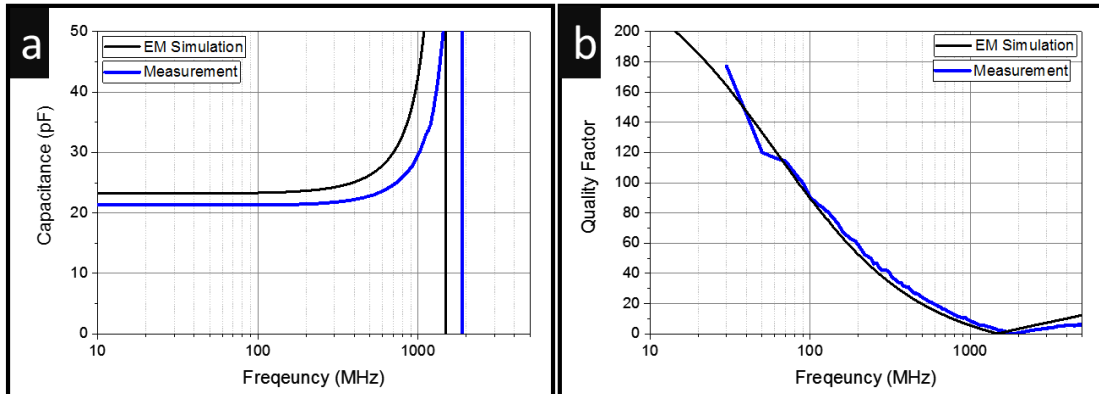
Figure 4-32: (a) RF testing capacitance measurement and simulation. (b) RF quality factor.

The simulated capacitance value is 23 pF and measurement is 21.5 pF, and the

difference can easily be attributed to thickness variations in the printed films. The

higher capacitance in simulation is also the reason for the slightly lower self-resonant

frequency (1.5 GHz versus 1.9 GHz). The quality factor follows the same trend as the low

frequency quality factors approaching 200, which is consistent with low frequency

measurements in Figure 4-30. The quality factor of the 20pF capacitor approaches 20 at

500 MHz. Design curves have been created from the capacitor measurements and

matching simulations to aid the designer in choosing which capacitors to use.
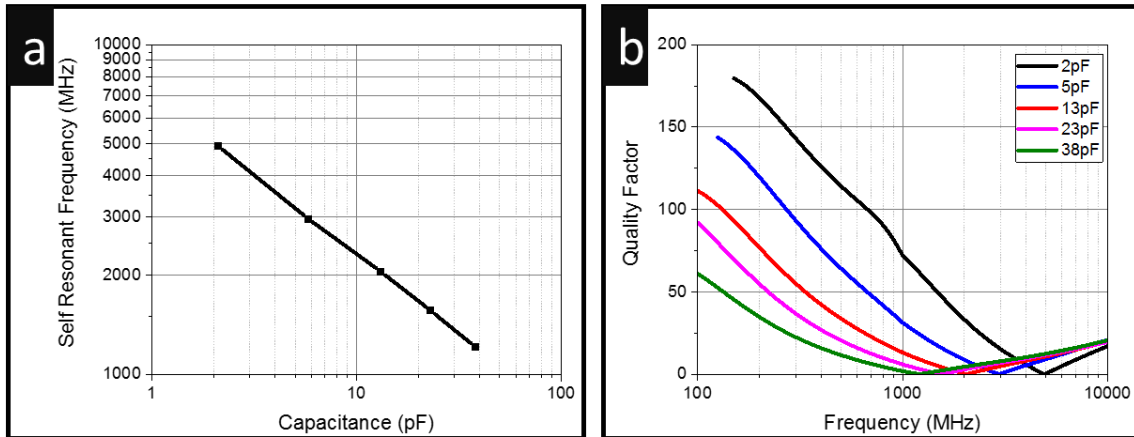
Figure 4-33: (a) Self resonant frequency versus capacitance size (b) Quality Factor. Note that the input pads are 250um in this case which has an effect on measured self resonance frequency.

The results Figure 4-33(a) show the trend of self-resonant frequency on a log-log axis as expected. The quality factors are plotted and also a clear trend with lower capacitance having a higher quality factor. All capacitors peak off at a quality factor of 200 as was shown with the low frequency measurements. These promising results show how solution-processed oxide dielectrics can produce quality RF components into GHz frequencies.

4.7 Conclusion

A sol-gel dielectric has been developed initially with spin coating and then successfully moved to inkjet printing. Early experiments detail that high dielectric dispersion in the films is overcome with proper (400°C) thermal processing of the film. Inkjet printed MIM capacitors with quality factors ~200 have been fabricated using a photolithography process developed in house, which includes an airbridge. The alumina layers are ~120nm thick, with ~0.5nm RMS surface roughness. Coffee ring staining has been studied and suppressed by utilizing an ethanol and 2-ME solvent system. The printed

alumina exhibits an estimated dielectric constant of 6.2 and temperature coefficient of capacitance of 330 ppm/$^{\circ}$C. The leakage current through the films is 2×10^{-9} A/cm^2 at 1MV/cm. Dielectric breakdown occurs above 20V. One concern is that the variation in capacitor value of these printed devices is ~7%. It is expected that with further development of the ink and surface treatment to optimize wetting, this variation could be further reduced. Radio frequency capacitors are shown with self-resonant frequencies in the GHz regime and a 20pF capacitor has a quality factor of ~20 at 500MHz. These are all promising results that demonstrate that high quality alumina thin films can be made by inkjet.

Chapter 5 - Multilayer Inkjet Printing of RF Passive Components

A dielectric was developed and printed for RF passives in Chapter 4. The next logical step is now to print the conductors and create a multilayer fully inkjet printing process. However, due to the high temperature (400°C), compatibility with printed conductors is a challenge due to oxidation and adhesion. The polymer dielectric PVP (poly-4 vinyl phenol) was chosen. This polymer has the unique property that it is processed at ~200°C, which is rather high for a polymer but ideal for the printed metal conductor. Tseng et al. have also shown in [10] and [100] that PVP can inkjet print for use in thin film transistors. The dielectric has excellent insulating properties with leakage current around $1x10^{-7}$ A/cm^2 for the printed films shown in the current work. Silver nanoparticle ink is utilized for the printed conductor, and vias are printed connecting the layers with less than 0.1 ohms of resistance. Spiral inductors of various sizes that demonstrate inductances from 10 to 75 nH with maximum quality factors around five have been realized. The 15 nH inductor exhibits a self-resonant frequency slightly below 1 GHz. The MIM capacitors are realized with densities of 50 pF/mm^2. These capacitors demonstrate values ranging from 16 to 50 pF. The 16 pF capacitor shows a self-resonant frequency over 1.5 GHz. The successful implementation of inductors and capacitors in an all inkjet-printed multilayer processes with vias is an important step towards fully inkjet-printed large area and flexible RF systems. This is the first demonstration of fully printed multilayer GHz inductors and capacitors with a dielectric and vias.

5.1   Inkjet printing PVP polymer

The PVP used for both spin coating and inkjet printing in this work is prepared by mixing three components: the solvent 1-hexanol (Sigma Aldrich 436216), the polymer PVP powder (Sigma Aldrich 436216), and the cross-linking agent poly (melamine-co-formaldehyde) (MMF) (Sigma Aldrich 418560). The solution is easily dissolved by stirring at room temperature with 5.0% by weight PVP and 0.77% by weight cross-linking agent. An advantage of PVP polymer is that it can be thermally cross-linked, which makes it resistant to environmental damage and the migration of silver through the thin layers. The structure of the PVP, the MMF, and the combination of the two can be seen in the thermally cross-linked PVP-MMF, as shown in Figure 5-1 [101].
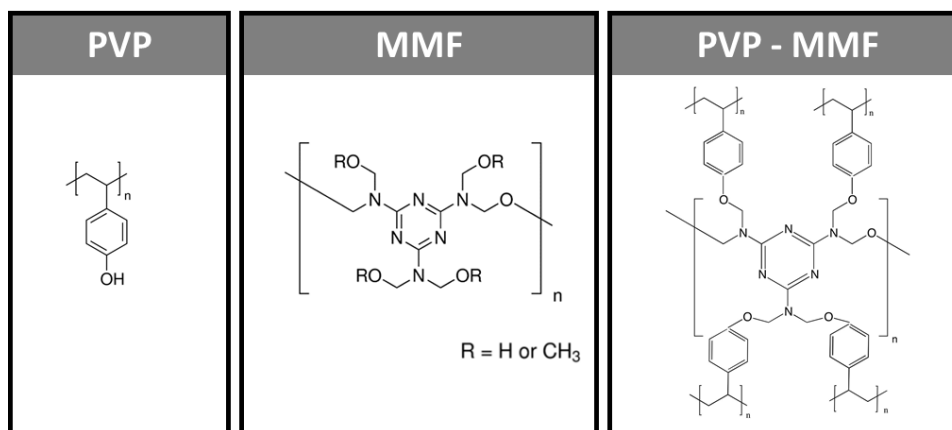
Figure 5-1: PVP and MMF chemical structures

A 5.0% wt. PVP was chosen since its rheology behaviour is nearly identical to Dimatix model ink, as compared in Figure 5-2(a). The addition of more PVP polymer causes a linear increase in the viscosity of the fluid.
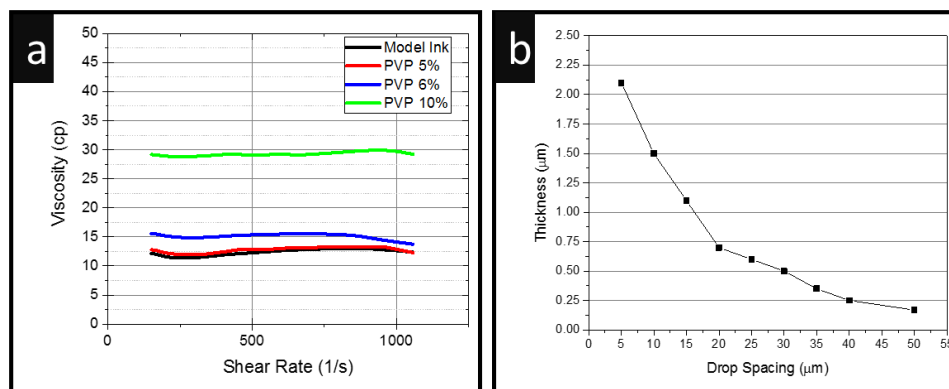
Figure 5-2: (a) Viscosity of fluids with different PVP concentrations compared with Dimatix model ink (Malvern Bohlin Gemini II Rheometer). (b) Drop spacing versus thickness.

Creating a PVP ink with similar fluid properties to the standard model ink allowed the model ink

jetting parameters to be used, including waveform, temperature, voltage, etcetera. The

properties of the formulated ink are detailed in Table 5-1.

Table 5-1 Properties of 5% wt. PVP ink in 1-Hexanol at 25ºC, using the 10pL cartridge with 21um diameter orifice at 9m/s velocity.

Viscosity (cp)	Surface T. Dyne/cm	Density (g/cc)	Drop Mass (ng)	Ohnesorge (Oh)	Reynolds (Re)	Weber (We)	Capillary (Ca)
11.5	29.5	0.89	7.4	0.49	14.6	51.3	3.5

Printing the PVP dielectric layer has the advantage that the thickness of the layer can be

precisely controlled. Additional layers of ink can be printed to increase the thickness, but finer

control can be obtained by varying the drop spacing, as demonstrated in Figure 5-4(b). One

difficulty of the printed PVP ink is coffee ring staining, which can be seen in the images of

printed squares in Figure 5-3. The problem was worse when printing was at high temperature;

each pass partially dried and had tall coffee ring stain edges. With room temperature printing,

the edges had coffee ring staining, although the central region was uniform. Only this central

region was used to make devices. A plot of drop spacing and PVP thickness, is shown in Figure

5-2(b). A comparison of an AFM film to a spin-coated PVP film is shown in Figure 5-4(a) and (b).
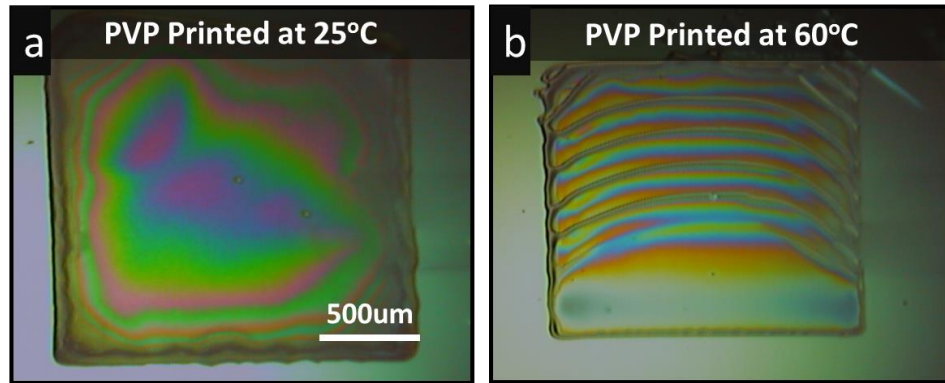
Figure 5-3: (a) Printed square of PVP ink on glass at 25°C. (b) Printed at 60°C substrate temperature.
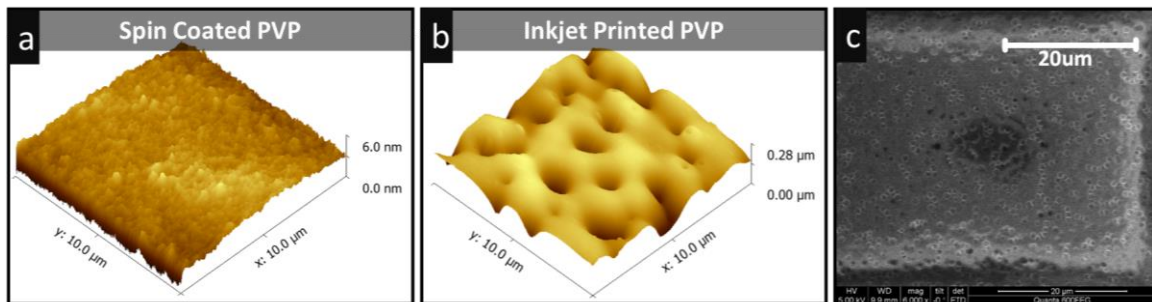
Figure 5-4: (a) AFM scan of spin-coated PVP film. (b) AFM scan of inkjet-printed PVP film. (c) SEM scan of inkjet-printed PVP film showing micro-bubbles in the film.

From the AFM image it is evident that there are small craters in the printed film in the hundreds

of nanometer range. These craters can be seen from the SEM image in Figure 5-4(c): on top of

the film there are micro-bubbles that form during the inkjet printed film. These micro-bubbles

contribute to breakdown and pinholes, and scaling the layers past 200 nm thickness was found

to be difficult. Printed MIM capacitors fabricated using overlapping patterns of silver ink and

PVP insulator are used to test the leakage current through the dielectric. Figure 5-5(a) the PVP

film shows good insulating behavior with an applied field of 0.5MV/cm a current density of

1.4×10^{-7} A/cm2 being measured. Even though this leakage current is small, it is one to two

orders of magnitude worse than conventional MIMs [27] and the alumina devices shown in

Chapter 3. No breakdown is observed for the 1.1 um-thick printed dielectric up to 0.9 MV/cm

(100V), which is the limit of the equipment. Figure 5-5 shows 100 MIM capacitors printed with

four different sizes to test the scaling and repeatability of the process. Although it appears that

the largest 3.4×10^{-2} mm^2 capacitor has the highest variance, all of the capacitors have a standard

deviation of roughly 5%. This is good considering the ink spreading, drop placement accuracy,

and variation of the printed dielectric thickness. As mentioned in Chapter 4, traditional silicon

nitride MIMs show variation of only 0.6%.
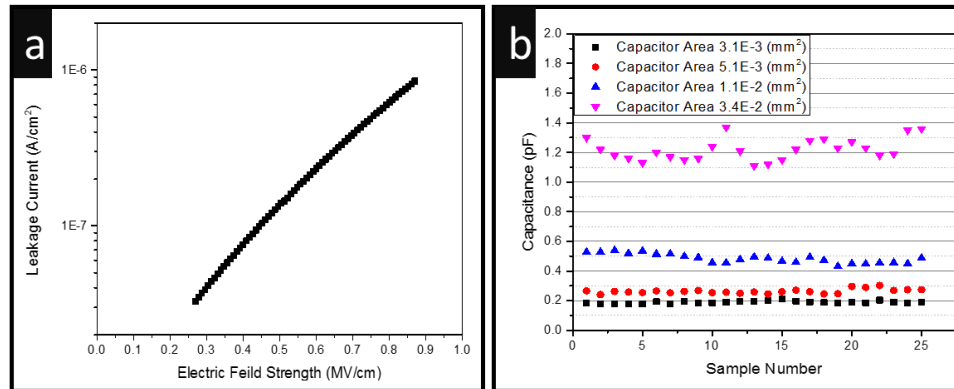
Figure 5-5: (a) Leakage current density of a printed 0.034 mm^2 area MIM capacitor through a 1.1 μm thick printed PVP dielectric layer. (b) Repeatability of fully inkjet-printed overlap capacitors with a 1.1 μm thick printed PVP dielectric layer.

5.2   Printed silver nanoparticle ink

Sigma Aldrich silver nanoparticle ink is commercially available and tailored for the

Dimatix printer with a viscosity of 10 centipoise and surface tension of 30 dyne. The ink

is conductive at sintering temperatures less than 200⁰C [59]. This ink can also be stored

for several weeks at room temperature in a cartridge without any noticeable change in

the performance or permanent nozzle clogging. One difficulty of nanoparticle ink is

surface roughness. This is especially crucial when printing multilayer structures, such as

the capacitors and inductors presented here. By optimizing the heating process smooth

films can be achieved. Figure 5-6 (a) is an image of a smooth inkjet printed silver line on

top of a printed PVP film.
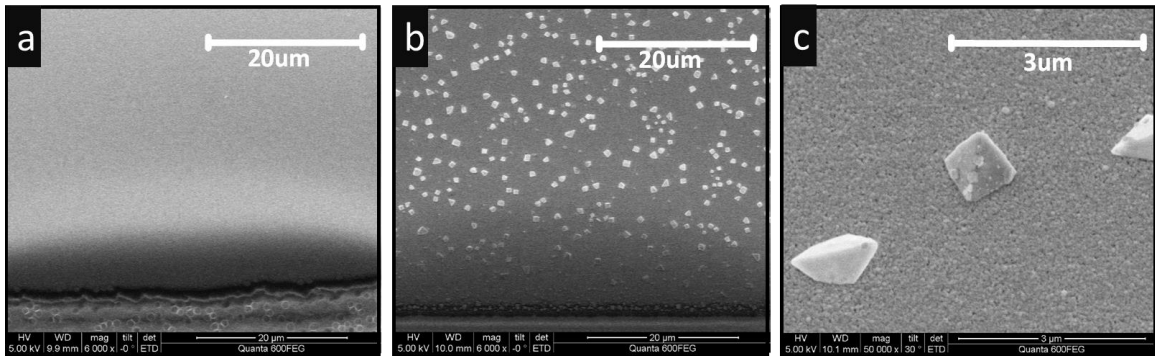
Figure 5-6: (a) Image of a printed silver line sintering in air at 150°C. (b) Image of a printed silver line sintered at 210oC. (c) Zoomed image of large particles on a printed silver line.

The printed silver ink was measured after being sintered at 150°C and 180°C, both cases

show root mean square surface roughness of < 20nm measured by atomic force

microscopy. Figure 5-6 (b) is an image of a silver line sintered at a higher temperature

(210°C) where there are visible particles on top of the film. Figure 5-6 (c) is a closer view

of the micro-meter sized particles on the silver line. These particles are observed when

processing several different batches of ink, and have been analyzed with energy

dispersive X-ray spectroscopy (EDS) to find that the particles have high concentration of

silver and chloride. Therefore it is probable that these particles are salt crystals (AgCl).

These particles cause short circuits, leakage current and voltage breakdown when

making multilayer components. Low processing temperatures (<200°C) provide smooth

silver lines as depicted in Figure 5-6 (a) that are necessary to make working

components. The conductivity of printed silver is especially important for RF passives

shows the conductivity of the printed silver ink on both glass and PVP substrate measured with a four point probe.
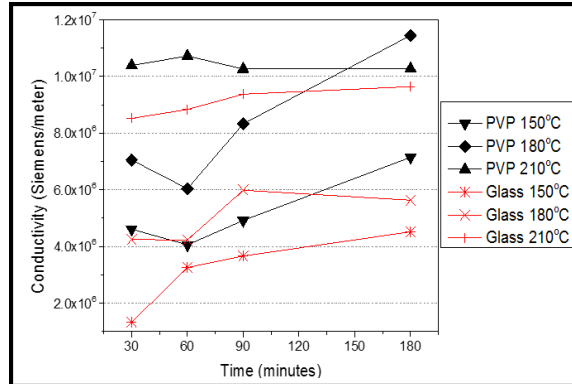
Figure 5-7: Comparison of silver nanoparticle ink conductivity for a single layer printed with 20 μm drop spacing on glass and PVP (sintered in air).

Each point in Figure 5-7 represents a different sample and the trend is that increased time and temperature increases conductivity. Also from Figure 5-7 it can be seen that the silver ink printed on PVP reaches a higher conductivity in less time and lower temperature than on a glass surface. The effect of substrate on sintering of nanoparticles has been reported in [102] [103] where coalescence occurs slower when particles are more tightly bound to the substrate surface. The 600 nm thick silver layers heated at 180°C show conductivity at 15% of bulk silver corresponding to a sheet resistance of 0.16 Ω/□ or 1.2×10^7 S/m. This is in agreement with [59] which shows between 1.0×10^7 - 2.0×10^7 S/m at 200°C on a Kapton substrate. Higher conductivities can be obtained with increased temperature, but exceeding 200°C for several minutes is not advisable since PVP begins to visibly decompose.

5.3 Fully printed multilayer inductors and capacitors

Multilayer printing and dissolving vias are used to create RF components as described in detail in this section. Several steps are involved in the fabrication and a flow chart is shown in Figure 5-8. A glass slide is used as a mechanical support which must be thoroughly cleaned. An initial layer of PVP is printed on the glass substrate which provides lower surface energy and superior print properties for Sigma Aldrich ink compared to a glass slide. The measured surface energy of PVP and glass (Fisher 12-544) is 47 mN/m and 71 mN/m respectively. Printed silver on the PVP surface with 10 pL drops and 20 um drop spacing provides a minimum silver line width of 40 um and can demonstrate reliable gaps of 50 um. More information about the drop spacing and lines is provided in Appendix 5. A laboratory oven is used for crosslinking of the PVP layer at 180°C, and then a layer of silver ink is printed on top of it. The temperature and ramp rate are important parameters to ensure smooth films. The silver ink is heated at a ramp rate of 2°C/min and held at 180°C for 30 minutes. Then a 350 nm thick single layer of PVP is inkjet printed on top of the sintered silver pattern. A via is then printed on the fresh PVP film to connect to the underlying metal. An image of the printed via on a wet PVP film is shown in Figure 5-10 (a). Dissolving vias have been introduced by Kawase et al. in [51] where an alcohol based solvent is printed to create a hole in PVP films, which could then be filled with conductive ink to create a via. In this work, the alcohol based silver ink both dissolves the PVP film and creates a conductive via to the next layer, thus reducing the need for printing solvent.
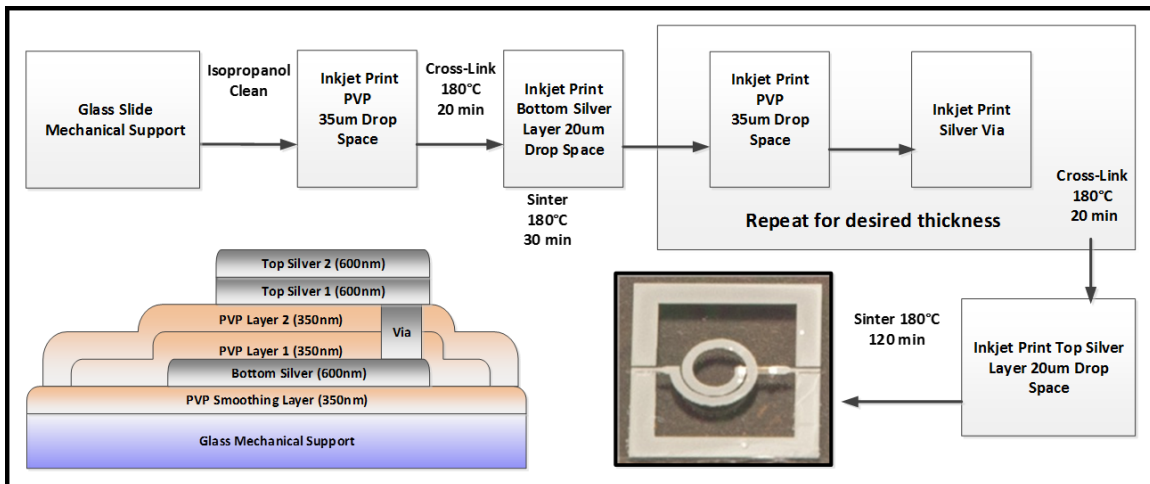
Figure 5-8: Process flow of fully inkjet printed inductor and capacitors and multilayer inkjet process stack-up (side-view).

Once the PVP is thermally cross-linked at 180°C for 20 minutes the dielectric film is robust and is not dissolved by solvent. Then the top layer of silver ink can be printed. This process of printing layers with connecting vias can potentially be repeated several times to create complex multilayer structures. The Dimatix printer has a realignment accuracy of ±25 µm which allows accurate multilayer printing using alignment markings. The printed layers as would be seen from a side view are shown in Figure 5-8. Using a profilometer the thickness of both the printed PVP and the silver can be seen in Figure 5-9. From this plot the single layer of PVP is around 350nm and the single layer of silver is about 600nm thick.
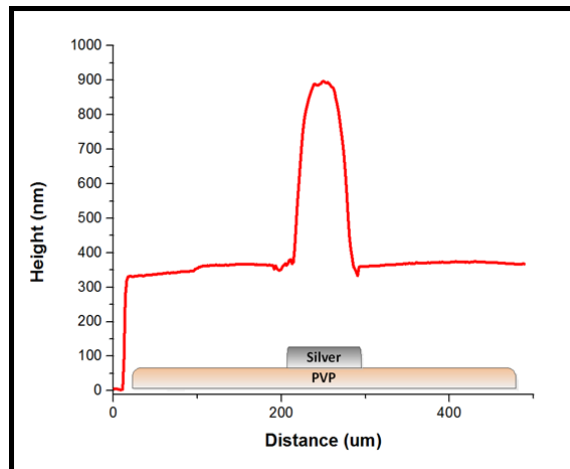
Figure 5-9: Profilometer measurement showing one layer of printed PVP and a single layer of silver printed on top
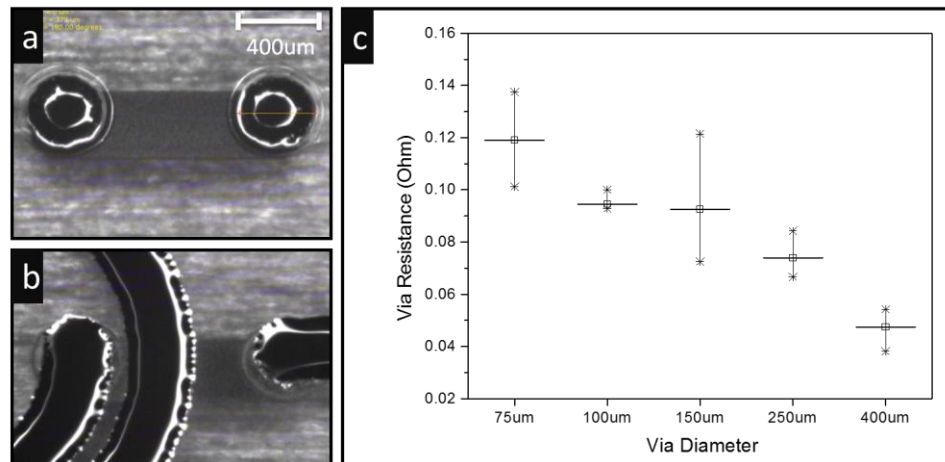
Figure 5-10: (a) Dissolving vias printed on top of a wet PVP layer. (b) Spiral inductor printed on top of the cross-linked PVP and vias. (c) Resistance of dissolved vias of different diameters printed though a 350 nm layer of PVP film. (Star is the min and max, square is the mean).

From Figure 5-10, the resistance of a 75 μm diameter via is slightly greater than 0.1 Ω

and is reduced to near 0.05 Ω for a 400 μm diameter via. For comparison, printed vias

demonstrated in [51] utilized conductive polymer ink and the interconnects were highly

resistive (>105 Ω). In [104] printed silver nanoparticle vias have been realized through

100 μm thick polyimide film drilled with a laser, these 30um diameter vias show

resistance of 0.25 Ω. This method of printing 400 μm diameter vias though 350 nm thick

PVP layers is used in both the capacitor and inductor fabrication. The 700 nm PVP films in Section IV are achieved by printing the 350 nm thick dielectric films and vias twice.

5.4 Characterization of capacitors and inductors

High frequency capacitors and inductors are designed using the process and material described in the previous sections. Ansoft High Frequency Structure Simulator (HFSS) software is used to make EM simulation models for both the inductors and capacitors. Advanced Design System was utilized to create lumped element models. The devices have been measured with an Agilent E863C vector network analyzer using 150 µm spaced Infinity GSG probes and a cascade probe station.

5.4.1 Capacitors

Capacitors are fabricated utilizing a via so that they can be measured in a two port configuration with 150 µm GSG probes. A depiction of the capacitor measurement planes and the de-embedding structures used is shown in Figure 5-11 .
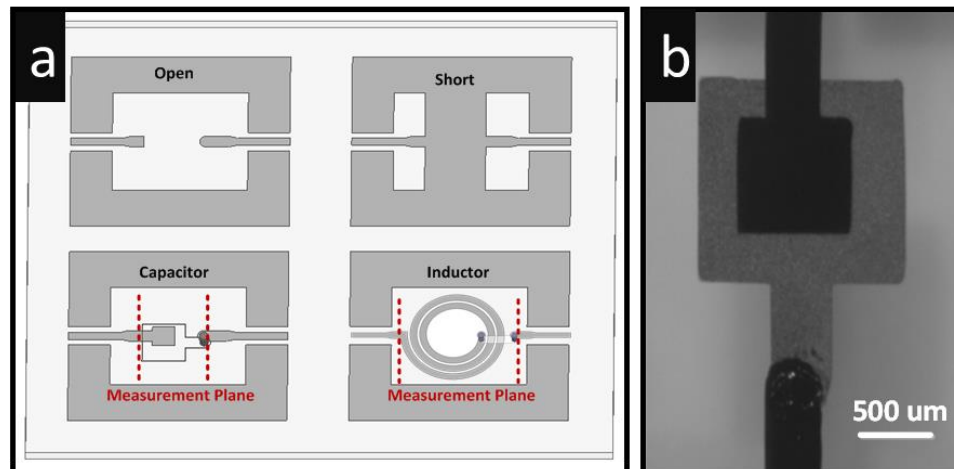
Figure 5-11: (a) Depiction of the de-embedding structures used along with the measurement plane of the capacitors and inductors (b) Fully inkjet printed MIM capacitor.

The thickness of the dielectric layer is 700 nm, achieved by printing two 350 nm thick layers of PVP ink. The structure of the capacitors is shown in Figure 5-11(b) The capacitance C and quality factor Q are extracted from the measurements using the following Y-parameter equations at each frequency point f.

$$C = -\frac{1}{im\left(\frac{4}{Y_{11} + Y_{22} - Y_{12} - Y_{21}}\right) 2\pi f} \qquad \text{5-1}$$

$$Q = -\left(\frac{im(Y_{11} + Y_{22} - Y_{12} - Y_{21})}{re(Y_{11} + Y_{22} - Y_{12} - Y_{21})}\right) \qquad \text{5-2}$$

In order to reduce the effect of the surrounding test structures, an open short de-embedding method is used as described in [105] and given by equations (3), (4), and (5). Where Y_{DUT} is the measured Y-parameters of the device and surrounding coplanar test structure. Y_{open} is the measured Y-parameters of an open test structure and Y_{short} is the shorted test structure. Z_{DUT}' and Z_{short}' are the Z-parameter matrices that are converted from Y_{DUT}' and Y_{short}' respectively. This de-embedding procedure eliminates the parasitics associated with the coplanar ground and input lines but the effect of the via is not removed.

$$Y_{DUT}' = Y_{DUT} - Y_{open} \qquad \text{5-3}$$

$$Y_{short}' = Y_{short} - Y_{open} \qquad \text{5-4}$$

$$Z_{Device}' = Z_{DUT}' - Z_{short}' \qquad \text{5-5}$$

Three capacitors 16 pF, 22 pF and 48 pF are demonstrated with areas of 0.34 mm², 0.50

mm², and 1.10 mm² respectively. A dielectric constant and loss tangent estimate were

based off of measured capacitor dimensions and values at 10MHz. A dielectric constant

of 3.3 and loss tangent of 0.07 are used in the simulations. A comparison of the

calculated, simulated and measured values is presented in Table I. The table highlights

the values of capacitance and quality factor at 13.56 MHz which is an important band

for RFID.

Table 5-2: Comparison of capaictors: calculated, EM simulation and extracted from measurement.

Area	Parrallel Plate Calc.	EM Simulation (13.56 MHz)		Measurement (13.56 MHz)	
(mm²)	(pF)	(pF)	QF	(pF)	QF
.34	14.2	16.0	12.7	16.6	12.9
.50	20.9	23.0	12.0	23.3	12.0
1.1	45.9	49.0	10.2	50.0	10.4

QF = Quality Factor

The calculated capacitance based on parallel plate method does not account for fringing

fields and is slightly lower than the EM simulations and measurements. The circuit

shown in Figure 5-12 is used to create a lumped element model for the capacitors based

on [106], [107].
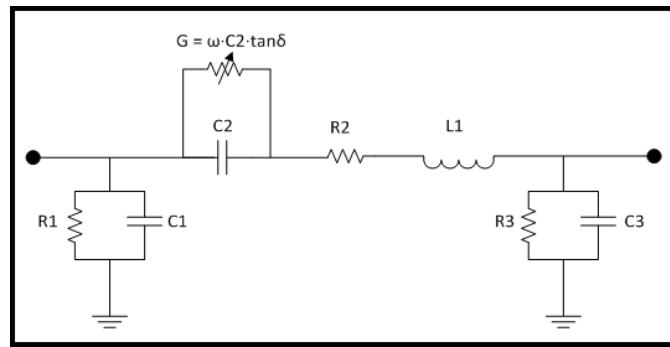
Figure 5-12: Capacitor lumped element model.

Table 5-3: Capacitor lumped element model values

(mm^2)	R1 (MΩ)	R2 (Ω)	R3 (MΩ)	C1 (pF)	C2 (pF)	C3 (pF)	L1 (nH)
.34	50	11.50	50	0.05	15	0.05	0.7
.50	50	11.0	50	0.05	20.5	0.05	0.7
1.1	50	9.8	50	0.05	46.5	0.05	0.6

The conductance G in the model is frequency dependent where ω is the radial

frequency and tanδ is set to 0.07. The values are obtained by providing the Y-

parameters extracted from measurement to Advanced Design System software and

setting them as the goal. An optimization routine is then run to find lumped element

values that provide a good match to the measured Y-parameters. Table 5-3 details the

lumped element values obtained. The measured, EM simulation and the lumped

element models match well and the extracted capacitance and quality factors are

plotted in Figure 5-13.
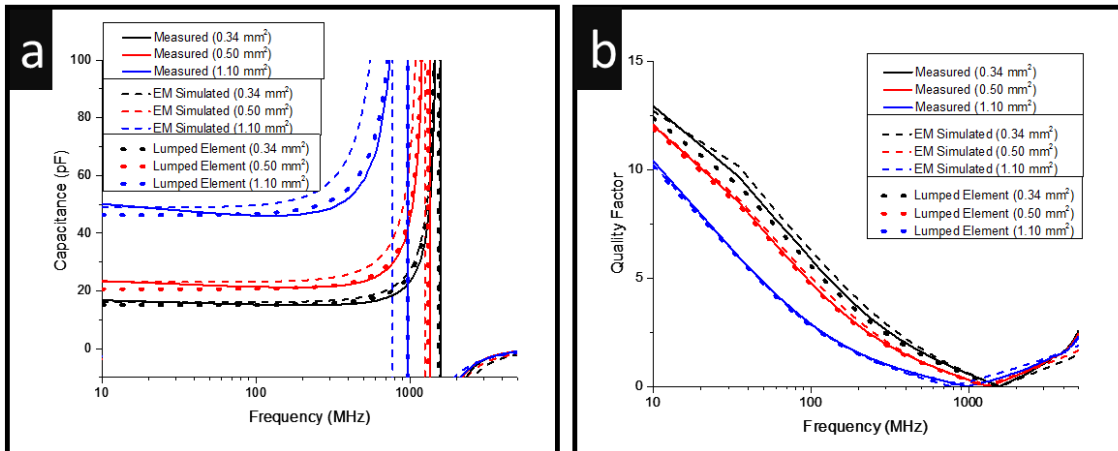
Figure 5-13: (a) Fully printed capacitors measured, EM simulation, and lumped element capacitance values vs. frequency (b) Quality factors vs. frequency, printed PVP dielectric thickness of 700 nm.

From Figure 5-13 (a) the measured curves show a decrease in capacitance with increasing frequency, which is evidence of dispersion in the dielectric constant. This effect is visually more pronounced for the 1.10 mm^2 capacitor since it has a larger capacitance. The capacitors also show ~2% increase in capacitance and ~20% decrease in quality factor after being stored in environmental conditions for 8 months. This may be due to the moisture adsorption, however proper packaging should improve this. Roughly 3% decrease in capacitance value is seen when the devices are heated to 100°C which is an acceptable result. Dissipation in the dielectric as well as the thin layers of low conductivity electrodes are major factors contributing to the low quality factors. The dissipation factor of solution processed PVP is poor compared to conventional microwave materials. As an example, DuPont PTFE has a dissipation factor of <0.0001 at 1 MHz [4]. As seen from the lumped element model the value of R2 is around 10 ohms and thicker higher conductivity ink is necessary to reduce the series resistance. These low quality factors <10 are also observed for printed capacitors in [11]. The measured

self-resonant frequency of the 0.34 mm2 capacitor is 1580 MHz, which is satisfactory for

low radio frequencies, including 13.56 MHz Radio Frequency Identification (RFID).

5.4.2 Inductors

Spiral inductors are designed and modeled using High Frequency Structure Simulator

software, based on the parameters in Figure 5-14 (a). The inductors are simulated using

a conductivity of 1.0×10^7 S/m with 1.2 µm thick metal layers. The inductors demonstrate

the ability to fabricate complex curved structures using inkjet printing. The gaps

between inductor windings are scaled down to 45 µm which allows for compact designs.
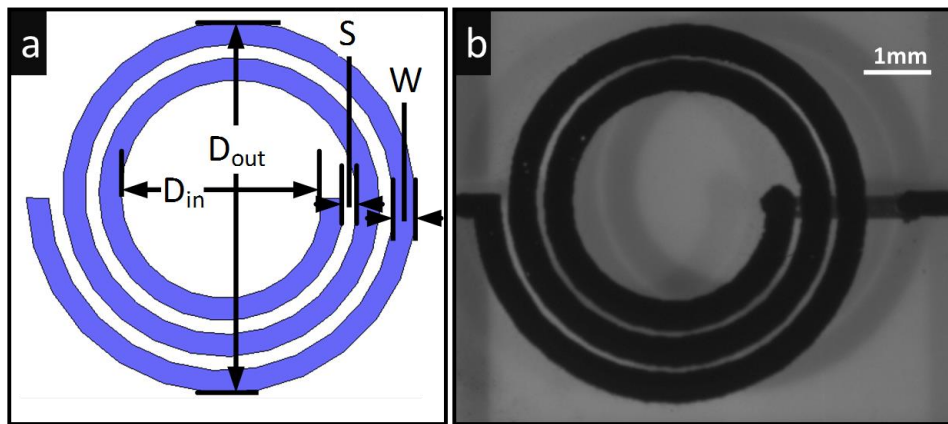
Figure 5-14: (a) Spiral 2.5 turn inductors, (S) space between lines, (W) width of line, (Dout) outer diameter
and (Din) inner diameter (b) Fully inkjet printed 2.5 turn inductor.

The open/short method described in Section IV A is used for de-embedding and the

measurement plane is shown in Figure 5-11(a) which includes the via. The quality factor

and inductance is extracted using equations (2) and (6).

$$L = \frac{im\left(\dfrac{4}{Y_{11} + Y_{22} - Y_{12} - Y_{21}}\right)}{2\pi f} \qquad \text{5-6}$$

EM simulation results and measurements of three printed inductors are highlighted in

Table 5-4.

Table 5-4: Comparison of inductance values from EM simulation and extracted from measurement

Dimensions					EM Simulation		Measured	
Turn	D_{out}	D_{in}	S	W	L	QF	L	QF
1.5	3550	1850	50	380	9.1	5.3	9.7	4.4
2.5	3500	1825	85	250	22.2	3.6	23.0	2.9
3.5	6400	3300	45	400	72.7	3.1	76.0	3.3

These inductors are printed with two layers of silver ink at a 20 μm drop spacing to improve the quality factors of the inductors. Dissipation from the dielectric has negligible effect compared to the inkjet printed silver nanoparticle films. The quality factors of the planar printed inductors demonstrated in [49] are less than 5 which is comparable to these results. There is no observed change to the inductors after storage for 8 months in environmental conditions. There is no significant change in the inductance value, but a one point increase in maximum quality factor is seen at an elevated temperature of or quality factor was observed with temperature up to 100°C. The lumped element model in Figure 5-15 is based on [108] with the addition of L2 which is the result of the bottom layer interconnect and via. Similar to the capacitors, the lumped element values are obtained by measured Y-parameter matching with Advanced Design System.
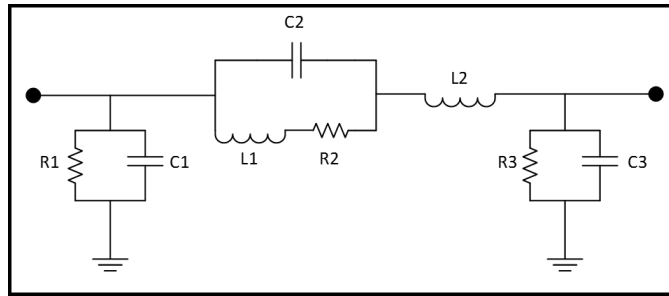
Figure 5-15: Lumped element model of the inductors

Inductor-lumped element values are shown in Table 5-5. In the lumped model, the estimated series resistance R2 increases as expected with the size of the inductor and number of turns. Even the 1.5 turn inductor exhibits about 3.5 ohms of series resistance, producing quality factors of around 5. The interwinding capacitance is similar for the 1.5 and 2.5 turn inductors, given that the 2.5 turn inductor has a larger conductor spacing of 85 um compared to 50 um. The measured EM simulation and lumped element models, which are compared in Figure 5-16, show a good match.

Table 5-5: Inductor-lumped element model values

Turns	R1 (MΩ)	R2 (Ω)	R3 (MΩ)	C1 (pF)	C2 (pF)	C3 (pF)	L1 (nH)	L2 (nH)
1.5	50	11.50	50	0.05	4.8	0.05	7.5	1.3
2.5	50	11.0	50	0.05	4.6	0.05	20.5	2.0
3.5	50	9.8	50	0.05	8	0.05	72	3.5
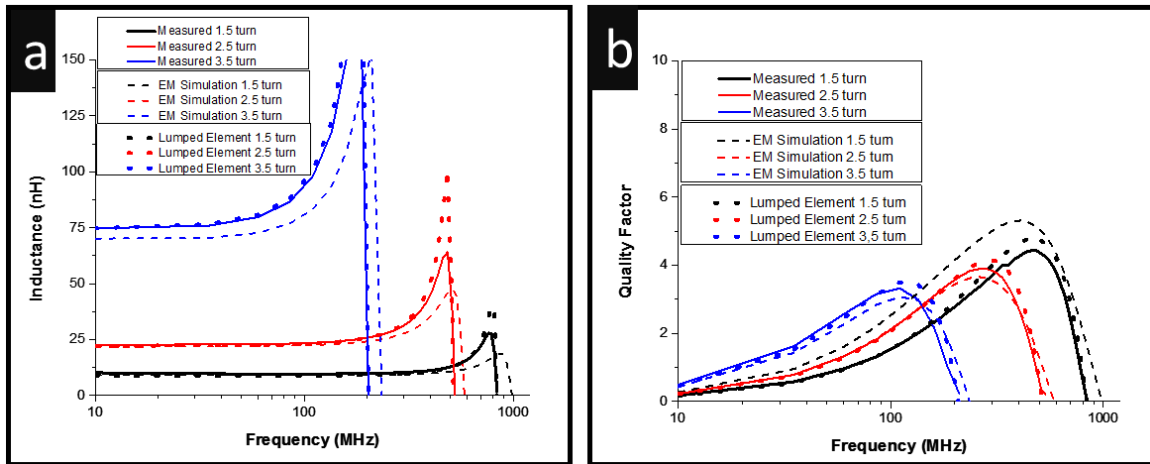
Figure 5-16: (a) Inductance values extracted from measurement, EM simulation, and a lumped-element model versus frequency. (b) Quality factors versus frequency, printed PVP thickness of 700 nm.

The thickness of the silver ink presents a major problem and simulations show that increasing the thickness from the 1.2 um used herein to 20 um would provide Qs of 15. Printing several layers of silver ink may seem like an obvious solution for reducing the series resistance, but difficulties arise with ink spreading. Using nanoparticle ink with a higher silver loading (>20wt%) may be an option. An alternative to nanoparticle-based printing that shows promise for reducing the resistance is a catalysis-based electroless metal deposition printing method [109].

5.5   Conclusions

In this work, we demonstrate inkjet-printed multilayer capacitors and inductors with through vias. The process we use provides a first step towards fabricating RF matching circuits and filters on printed circuit boards. A glass substrate is used as the mechanical support in this work; however, the process can be applied to other smooth surfaces that can withstand temperatures of 180°C. A key advantage of the process is that inkjet-

printed dissolving vias are shown to be repeatable with less than 0.1 ohms resistance. A wide range of printed RF MIM capacitors from 16 pF to 50 pF are shown. The self-resonant frequency of a 16 pF capacitor is 1580 MHz, which is sufficient for many RF applications (including RFID). The quality factors of the capacitors are relatively low compared to conventional capacitors that use microwave dielectrics. These results draw attention to the fact that resistive printed conductors and a poor dissipation factor in solution-processed PVP are issues for RF capacitors. In the future, other materials such as fluoropolymers or solution-processed oxides with lower a dissipation factor can be investigated to improve the performance of printed capacitors.

Complex spiral inductors that show good agreement with simulations have been demonstrated. A 9.7 nH inductor is shown to have a self-resonant frequency of 850 MHz and maximum quality factor of 4.4. Large value inductors of 75 nH with a footprint of 42 mm^2 and Q of 3.3 have also been fabricated. Both the self-resonant frequency and the quality factor can be improved with increased dielectric thickness. Unlike with capacitors, the dielectric loss is not as crucial and the metal thickness and conductor loss are the significant influences.

Chapter 6 - 3D Inkjet-printed Passives

The concept of fully inkjet-printing passive components with a dielectric and metal was shown in Chapter 5. A further step is now taken to 3D inkjet print the dielectric. Such printing allows for multilayer lumped element passives, as well as thick dielectric layers and complex geometries for 3D passive RF components (such as antennas). This work demonstrates an all-inkjet printing process that can create 3D parts with integrated highly conductive metal for the first time.

6.1   3D inkjet printing process

One of the major advancements in inkjet printing has been the use of UV-cured acrylic materials. Like acrylic paints, inks can be made with vibrant colour and immediately cured upon exposure with a low-cost UV flood lamp. A major benefit of UV-cured ink is that the droplet is pinned, which restricts ink spreading due to the polymerization reaction that is immediately induced by the UV exposure. This concept can be taken beyond graphic art to form fully printed 3D parts. While the technology is still in its infancy, commercial 3D inkjet printers that are based on the concept shown in Figure 6-1 are now available from Stratasys and 3D Systems.
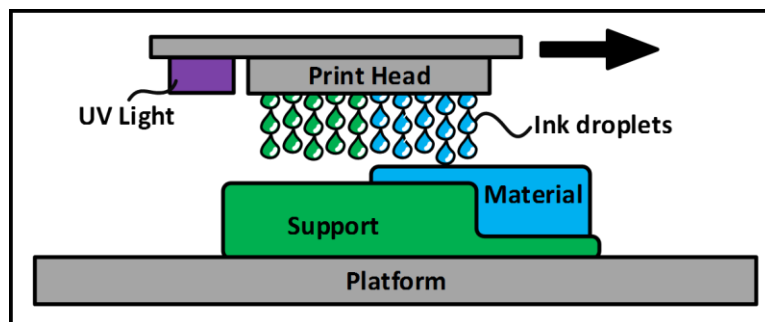
Figure 6-1: 3D inkjet printing with UV-cured polymer and wax/gel support

From Figure 6-1, both a build material and support material are printed together. The support is necessary to hold up overhangs during printing. After printing the support is simply washed or melted away, leaving a solid UV cured acrylic part. A major advantage of the inkjet process over other 3D techniques is that multiple materials can be deposited together. So far this has been restricted to the colorful UV cured acrylics and wax/gel like support materials. An exciting opportunity exists for 3D inkjet printing of electronics if a metal could be integrated within the process. To date there have been several reports of 3D printed RF electronics, however the metal has been deposited by sputtering, aerosol, plating solutions, and conductive pastes [53], [57], [60]. In this work an inkjet printed metal is integrated into the UV cure material creating a fully 3D inkjet technique for rapid prototyping and electronics fabrication. The major difficulty with integrating the metal is the thermal compatibility with the 3D material. A new silver organo-complex (AOC) ink is utilized, developed in house, which achieves a high conductivity of 1×10^7 S/m at a low temperature (80°C) only using a low cost IR lamp. Two applications are demonstrated: an RF low pass filter and a patch antenna. The second application, a printed patch antenna, takes advantages of the complex shapes that can be created with 3D printing. A honeycomb substrate minimizes material consumption, reduces the weight, dielectric constant, and dielectric loss which is all around beneficial. The key to the fully inkjet printing process is the materials involved, both the AOC ink the UV cure polymer. The materials are characterized in terms of jetting stability, temperature behavior, surface roughness, dielectric and conducting properties, voltage, and especially as a function of frequency.

6.2 UV Cure polymer ink

Stratasys UV cure ink is sold under the name "Vero", and comes in different colors and hardness. From the MSDS of hard Vero White, it is composed mostly of acrylic monomers (<30%), isobornyl acrylate (<25%), and various other components; acrylate oligomers and urethane acrylates [78], [110]. Less than 1% titanium dioxide is used for the white color. The photoinitiator is Diphenyl-2,4,6 trimethylbenzoyl oxide (<2%), which produces a free radical upon UV exposure, initiating the polymer reaction of the acrylic monomers and oligomers. The acrylic monomers are liquid at room temperature but too viscous for inkjet, at 125cp, Figure 6-2.
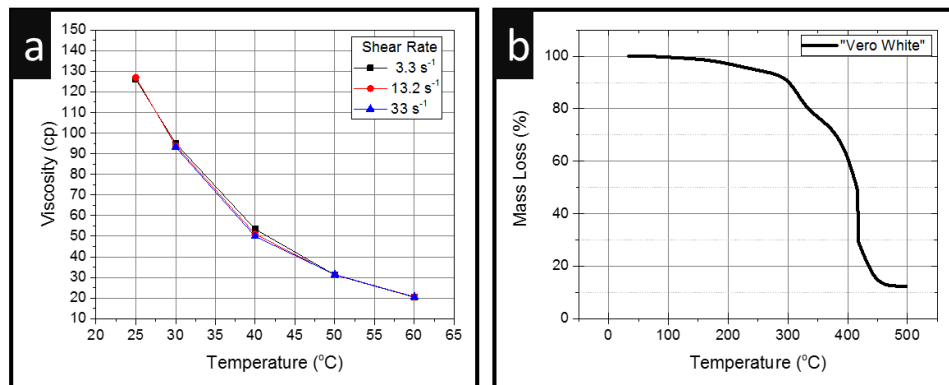
Figure 6-2(a) Viscosity of Vero ink (b) TGA of Vero material after UV curing.

Although the Vero ink is tailored for Stratasys Objet product line of 3D inkjet printers, it was more convenient to print with the Dimatix printer. The Dimatix allows control over nearly all print settings[11]. By using a jetting temperature of 60°C the viscosity of the Vero ink drops to 20cp, allowing for excellent jetting from the Dimatix 10pL print head. The fluid properties and operating point of the ink are given in Table 6-1.

---

[11] The 3D inkjet printers use software which automatically places support material around the part, which is often unwanted when metal is to be integrated with the parts.

Table 6-1: Fluid properties of Vero ink at 60°C jetting temperature with a Dimatix 10pL 21um nozzle at 9m/s. (Surface Tension has little variation with temperature, and was measured at 25°C)

Viscosity (cp)	Surface T. Dyne/cm	Density (g/cc)	Drop Mass (ng)	Ohnesorge (Oh)	Reynolds (Re)	Weber (We)	Capillary (Ca)
20.0	30.2	1.1	9.6	0.75	10.4	62	6.0

Throughout this work the UV cure ink is printed with 2 layers at 30um drop spacing forming 12um thick layers. For curing, the material is exposed with 7500 mJ/cm² 365nm UV after printing. After UV curing a TGA was completed to understand the thermal limits of the material, Figure 6-2(b). The TGA shows that there is negligible mass loss up to 150°C, however the glass transition for the material is 50°C [111] and there is extreme warping of the material over 80°C. Processing the cured material above 80°C should be avoided.

In order to design radio frequency components with the dielectric it is important to know the dielectric constant and dissipation factor. From the parallel plate measurements in Figure 6-3, the Vero material has a dielectric constant of ~3.0 and a dissipation factor ~0.02 up to 1GHz.
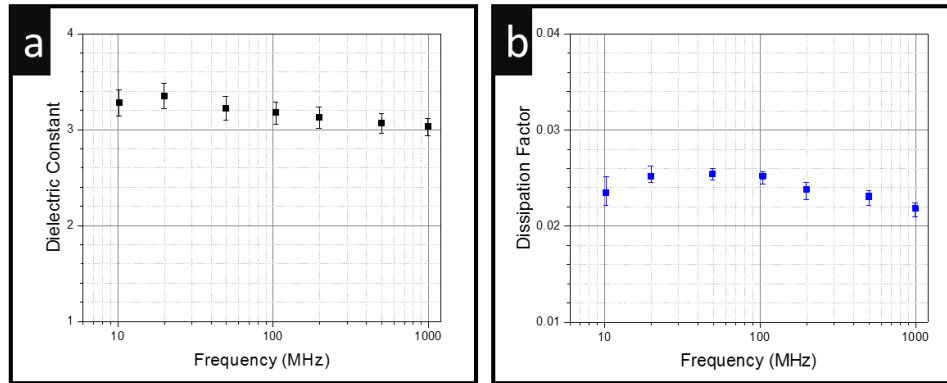
Figure 6-3: Dielectric properties of Stratysys Vero White UV cure acrylic polymer material. Bars represent the maximum and minimum measurement values of five test samples with the parallel plate method Agilent E4991 and dielectric test fixture 16453A

Capacitors were printed with an in-house silver ink for electrodes (discussed in the next section). The capacitors have leakage current values around 1×10^{-10} A/cm^2 at 0.08MV/cm (equivalent to 100V across the 12um thick capacitor). This is excellent, even compared to the popular poly-(4-vinyl phenol) dielectric [9],[98], albeit the layers are an order of magnitude thicker, 12um in this case.
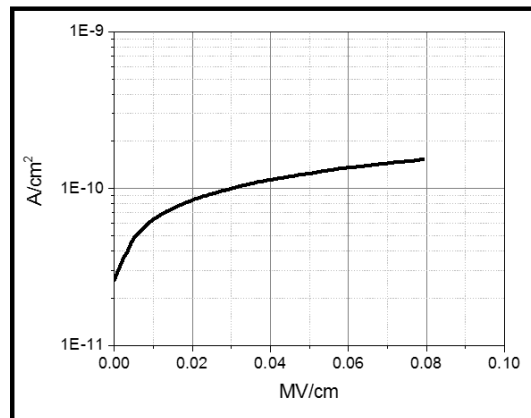
Figure 6-4: Leakage current of a typical fully printed capacitor (tested to 100V ~0.08MV/cm) Dielectric thickness 12um.
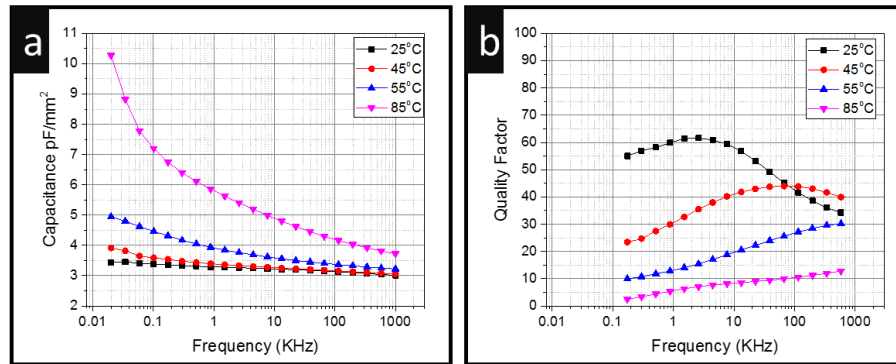
Figure 6-5: (a) Capacitance versus frequency (b) quality factor, tested at 1V AC signal and 0 bias condition. 12um thick printed layers.

The capacitors were tested against frequency and temperature, Figure 6-5. While the dielectric behaves well at room temperature and up to 45°C, the material shows considerable dispersion at elevated measurement temperature. This is a known behavior in acrylic materials caused from dielectric relaxation at the glass transition temperature, (~50°C). A thorough investigation of the dielectric relaxation in thin acrylic sheets is provided in [112]. A complete characterization of the dielectric relaxation with temperature for this material is out of the scope of this work. The important point is that the dielectric is sensitive to temperature and should be operated below the glass transition. The Vero dielectric has also been tested against voltage bias and there is negligible change in capacitance value, Figure 6-6. The major change in both physical and electrical dielectric properties occurs at elevated temperature. There is no issue so long as the material is processed below 80°C to avoid excessive warping, and operated below 45°C to avoid dielectric changes at the glass transition temperature.
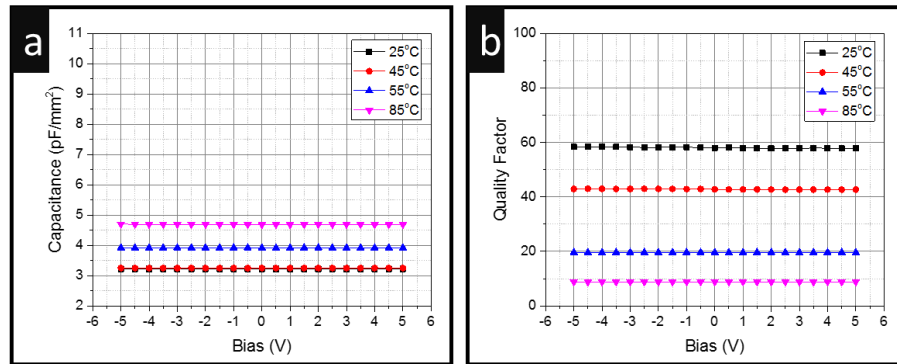
Figure 6-6: (a) Capacitance versus bias (b) Quality factor. Measured with a 1V AC signal and 10KHz frequency.

6.3 Silver-Organo-Complex ink

While silver nanoparticle ink has been widely investigated and is available commercially, it has some drawbacks. Silver nanoparticle ink has a complex synthesis protocol, high cost[12], high sintering temperatures (>150 °C), particle aggregation, nozzle clogging, poor shelf life, and jetting instability. Through the use of smaller nanoparticles (~10nm), and more robust ink formulation, commercial silver ink performance has improved considerably, even during the course of this PhD. However, in the long term it is difficult to avoid particle aggregation and precipitation in a nanoparticle system. Organometallic inks are another approach to printing conductive patterns. They contain dissolved precursors of metallic elements bonded with organics(i.e. silver acetate, silver oxylate [113], copper hexanoate [114]) In general, the organometallic bond is broken and the organic molecule evaporates away leaving a metal film behind. In the past

---

[12] The cost of nanoparticles inks at a research level are very high. While the current price of silver is about $480 per Kilogram, nanoparticles inks are in the range of $20,000 to 25,000 per kilogram of silver.

organometallics have been less successful than their nanoparticle counterparts[13]. In

2012, B. Walker et al. presented an organo-metallic silver complex ink with a simple

preparation protocol that provided bulk conductivity at 90°C [64]. This is a major

improvement from the typical ~25% conductivity seen for nanoparticle inks at >150°C.

However, there are many factors besides conductivity to consider when designing ink,

such as adhesion, viscosity, and long term stability. An in house Silver-Organo-Complex

(AOC) ink which is stable and transparent (Figure 6-7) has been developed in

collaboration with Mohammed Vaseem within our laboratory group at KAUST and

recently accepted for publication[14].
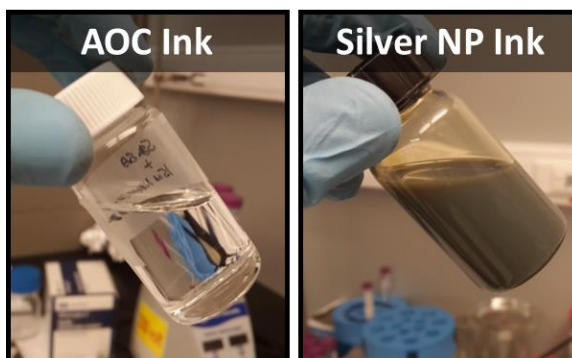
Figure 6-7: Silver Organo Complex (AOC) ink and a Silver Nanoparticle ink.

The AOC ink does not achieve bulk conductivity as does the work by Walker, but still

provides an impressive 1x10^{-7} S/m, (20%) of bulk conductivity at 80°C. Along with the

high conductivity at low temperature the ink exhibits strong adhesion, long term

stability (> 5months in a print head), and robust jetting performance. The detailed ink

---

[13] This is evident since until recently there were virtually no commercial organometallic inks compared to nanoparticle based inks. One of the first commercial metalorgano inks was TEC-IJ-040, InkTec Co., Ltd, Korea [115].

[14] V. Mohammed, G. McKerricher, Atif Shamim "Robust Design of a Particle Free Silver-Organo-Complex Ink with High Conductivity and Inkjet Stability for Flexible Electronics" Manuscript ID: am-2015-08125n, Accepted with Revisions, ACS Applied Materials & Interfaces (Full Paper), Oct. 2015

formulation is explained with an illustrative experiment in Appendix 6. Briefly, the ink is based on silver acetate complex with ethylamine, ethanolamine, water, methanol and 2-Hydroxyethyl cellulose (Mw ~90,000) that acts as a viscosity modifier and adhesion promoter. The fluid parameters of the ink are given in Table 6-2.

Table 6-2: Silver (AOC) ink fluid properties at 25°C jetting temperature and 10m/s from a 10pL 21um Dimatix nozzle.

Viscosity (cp)	Surface T. Dyne/cm	Density (g/cc)	Drop Mass (ng)	Ohnesorge (Oh)	Reynolds (Re)	Weber (We)	Capillary (Ca)
5.9	30.7	1.17	7.0	0.21	41.6	80.0	1.9

The conductivity of the ink has been tested as a function of layer thickness, shown in Figure 6-8. The ink has a silver loading of ~17% and can provides ~500nm thick layers per pass with the 10pL nozzle, similar to nanoparticle based inks. The conductivity of the ink approaches 2×10^7 S/m at 150°C and 1×10^7 S/m at 80°C with overprints as shown in Figure 6-8(b).
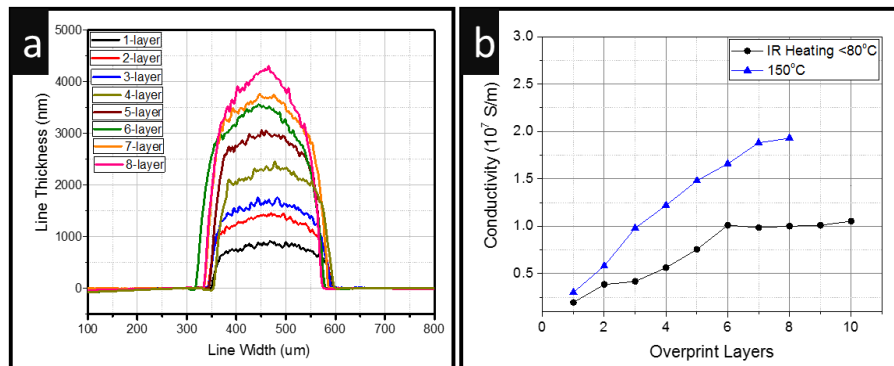
Figure 6-8: (a) AOC ink thickness at 20um drop spacing (b) conductivity of the ink after 30min 150°C heating of each layer and with 5min Infrared heating (IR measured surface temperature is near 80°C).

The AFM scan in Figure 6-9 (a) shows surface roughness of 95nm on the sintered AOC

ink. The SEM image Figure 6-9 (b), reveals high density and 99% silver content is

detecting from EDX.
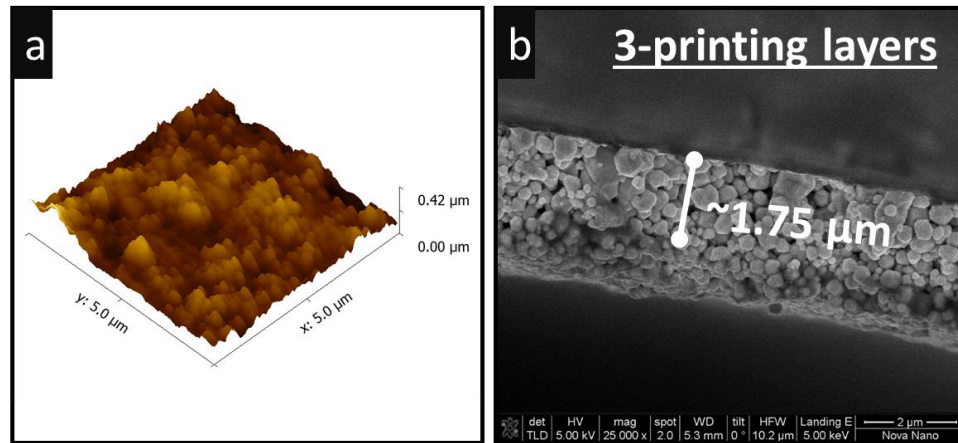
Figure 6-9: AFM surface scan of AOC ink after sintering at 150ºC (b) cross section SEM of the sintered AOC film.

Adhesion was a major concern for the ink and it was found experimentally that the

addition of a small amount of 2-Hydroxyethyl cellulose solved the issue. Adhesion to

glass, PET, and the 3D printed materials was tested with scotch tape without any

removal of the silver film. The ink is stable over the long term, as tested with a Dimatix

10pL cartridge over 5 months with no observable reduction in the overall drop mass.
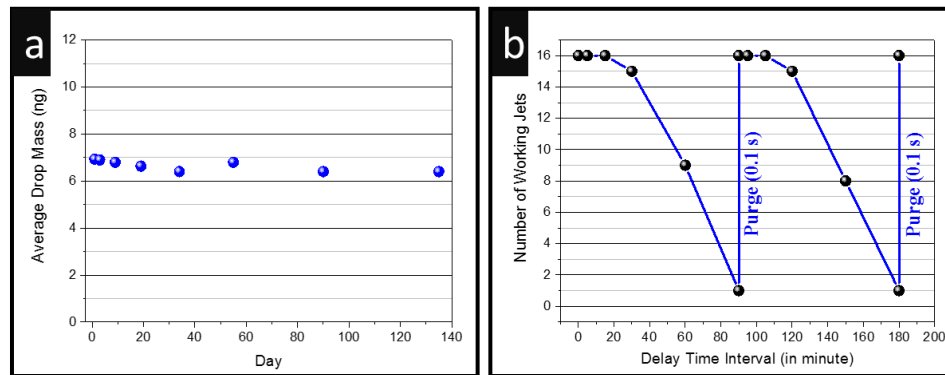
Figure 6-10: (a) Average drop mass with number of days and (b) number of working jets with delay time interval. For storage, the ink was kept in a refrigerator at 4 0C.

Figure 6-10(a) is a graph of the average drop mass with time, indicating that there is no full or partial nozzle clogging over 5 months in a cartridge. The effect of the delay time interval on the number of working jets was also investigated, as presented in Figure 6-10 (b). The number of working jets on the Y-axis of Figure 6-10(b) means that when the delay test starts there are 16 total nozzles available all ejecting ink. The nozzles are paused and replayed with every delay time interval, and the jetting of the nozzles is assessed. At up to 30 minutes of delay, all the nozzles jet without issue. As the delay time interval increases from 30 to 60 mins, working nozzles dropped to total of 9, which further dropped to 1 after 90 min delay. Most of the nozzles stop working after a 90 min delay and the likely reason for this is the evaporation of ink in the nozzle. However, after 0.1 s purge, all 16 nozzles again restart and follow the same delay trends. The effect of evaporation temporarily blocking nozzles at 30 minute delays is not an issue since the nozzles can be restarted after a short purge.

6.4 Fabrication process

Both the AOC and UV cure polymer have excellent jetting properties from the Dimatix printer and can be processed at 80°C. They can now be integrated to create fully 3D inkjet printed RF components. A depiction of the all inkjet process is shown in Figure 6-11.
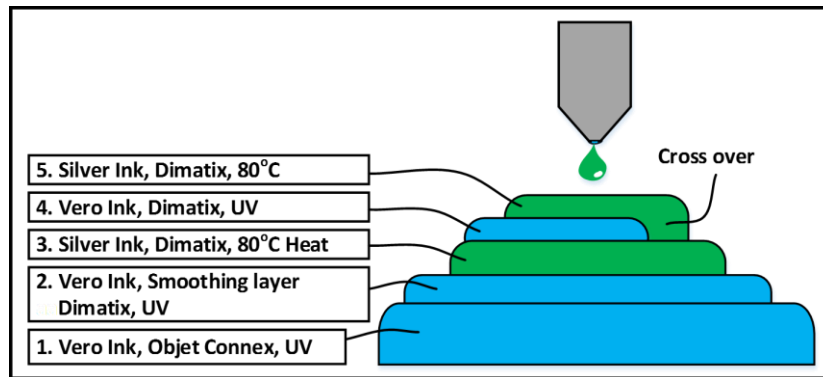
Figure 6-11: 3D inkjet process with integrated metal

First the UV cure material is printed with the Objet 3D printer allowing complex and thick shapes. A challenge that still exist is the surface roughness of the printed material from the Objet printer. Surface roughness is especially detrimental in RF components where it causes loss in the devices. The AFM scan in Figure 6-12 (a) shows the wavy surface "as printed" and instantly UV cured material with 1.8um RMS roughness. This was improved with the jetting of an additional layer of Vero ink with the Dimatix printer. After deposition the ink is allowed to spread before UV curing and smooths the surface to 0.4um RMS roughness, Figure 6-12(b).
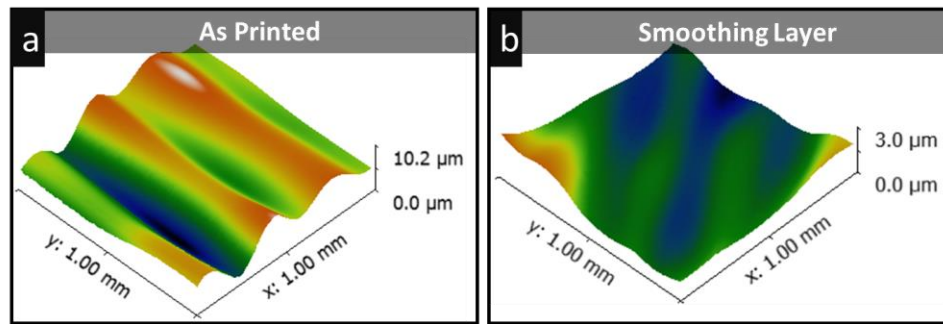
Figure 6-12: Interferometer measurements of the UV cure Polymer (Vero white) as printed RMS roughness of 1800nm and with smoothing layer 400 nm RMS roughness.

Another difficulty to overcome during the fabrication was the wetting of the Vero ink on the printed AOC silver layer. The Vero ink spreads excessively on the silver layer. In order to optimize the wetting condition a perfluorodecanethiol (PFDT) treatment was used. This treatment has been demonstrated in [9] to increase the surface hydrophobicity of printed electrodes. The parts are dipped in a bath of 0.28mL PFDT with 100mL of IPA, then rinsed in IPA and dried with nitrogen. The change can be seen in the contact angle measurements Figure 6-13.
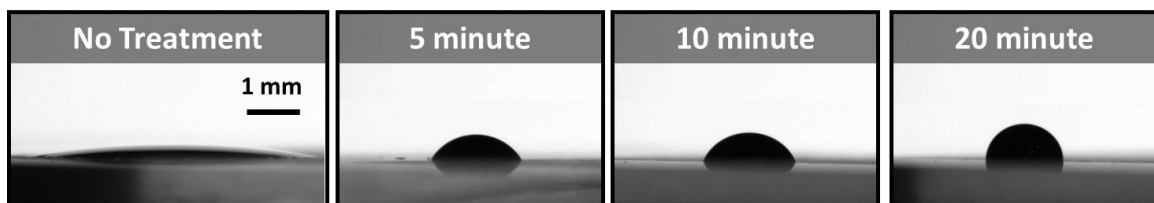
Figure 6-13: Contact angle adjustment of vero ink on AOC silver after immersion in perflourodecanethiol bath. (contact angle measurements taken 5 seconds after impact)

Without treatment the ink spreads uncontrollably on the surface, (note that all images are taken 5 seconds upon impact). After 10 minutes of surface treatment, the contact angle remains stable at 65° and high definition patterns were possible with the Vero ink on top of the silver. This allows for vero and silver to be printed in a multilayer fashion, capable of fabricating RF passives.

6.5   3D printed filter demonstration

RF passive filters are an integral component in almost all wireless devices. They are also physically large, since the size is dependent on the frequency of operation. These large area devices could benefit greatly from a low cost large area printing technology. It is no surprise that there has been several reports of inkjet printed filters in literature. However, these filters have shown less than ideal performance with insertion loss of 5 to 10dB [116], [117]. One of the best reports has shown insertion loss around 0.5dB at its center frequency (2 GHz), but utilized inkjet printing along with electroless plating to increase conductivity and thickness[118]. Other filters in literature including [119],[120] have used conductive ink on a conventional substrate and without a dielectric. A recent report [58], shows a novel concept of 3D printing, together with syringe injection of a silver paste at 70^oC to create 3D inductors and capacitors; however these pastes achieve low conductivity of 2.8×10^5 S/m. This work demonstrates two orders of magnitude higher conductivity 1×10^7 S/m with a fully 3D inkjet printing process. To the authors knowledge this is the first 3D inkjet printed lumped element RF filter. A Butterworth filter has been chosen as a demonstration, this is a textbook example, described in the classic paper by S. Butterworth in 1930 [121]. One implementation of a low pass Butterworth filter uses a series inductor and shunt capacitor as shown in Figure 6-14 (a).
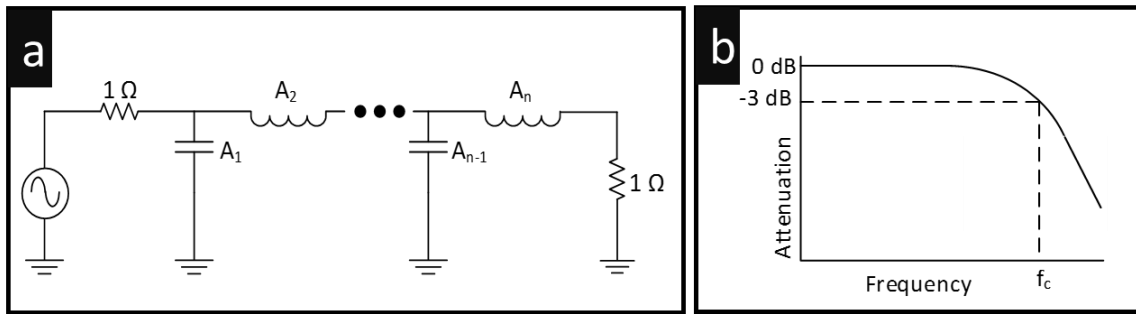
Figure 6-14: (a) Butterworth low pass filter (b) Butterworth response

The values of the components are chosen by using equation 6-1.

$$A_k = \frac{2\sin(2k-1)\pi}{2n}, \quad k = 1,2\ldots n \qquad \text{6-1}$$

The equations give component values for a normalized cut off frequency (f_c) at 1 radian, and input and output impedances of 1 ohm. To scale the values for the intended f_c, and impedance (typically R=50 ohm in radio frequency designs), the following equations are used.

$$C = \frac{A_k}{2\pi f_c R} \qquad \text{6-2}$$

$$L = \frac{RA_k}{2\pi f_c} \qquad \text{6-3}$$

Individual inductors and capacitors were fabricated and measured to gauge the performance. A capacitor measurement and simulation are shown in Figure 6-15.
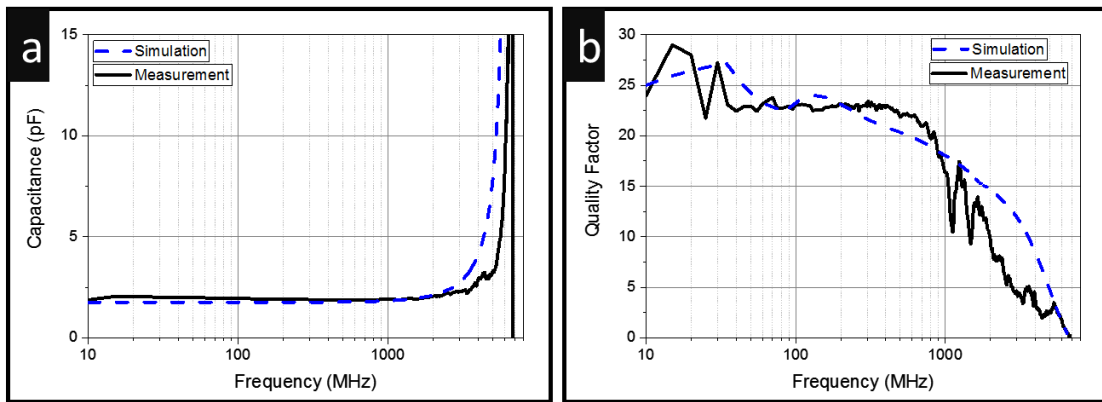
Figure 6-15: (a) Capacitor measured and simulated (b) quality factor (Capacitor area is ~0.9mm^2 with a 12um dielectric)

The capacitor is about 2pF and has a self resonant frequency of 6.5 GHz. The quality factor of the capacitor starts out at 25, and drops down to zero at self-resonance; this is consistent with low frequency measurements in Figure 6-5(b). An inductor has also been tested as shown in Figure 6-16. This 1.5 turn inductor has a self-resonance at 4 GHz, and is roughly 8nH at 1GHz frequency. The quality factor in simulation is slightly higher than the measurement at 7.5. This is likely due to more resistance from the printed ink than simulated, the inductors are extremely sensitive to conductivity and thickness of the printed ink. These inductors have been printed with 5 layers of AOC ink. The quality factors for both the inductors and capacitors are considered state-of-the-art among inkjet printed passives, [98] [122] even with the low 80°C processing temperature.
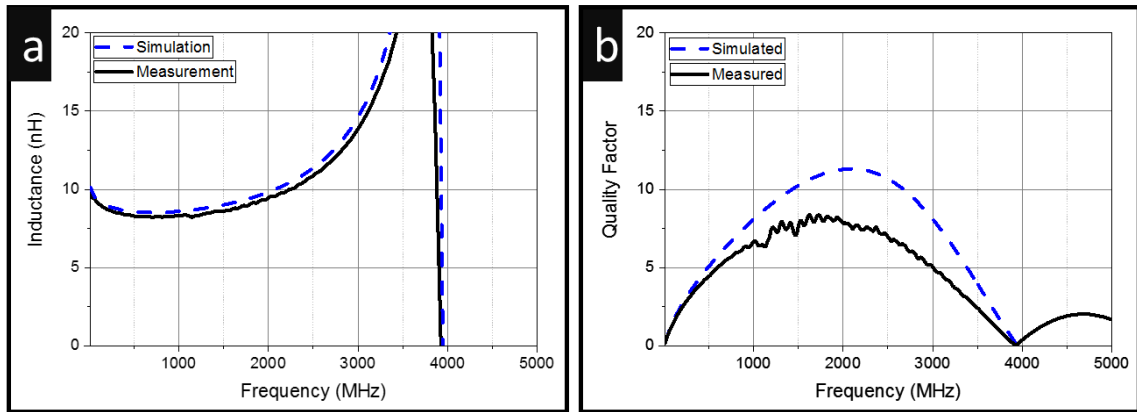
Figure 6-16: (a) Inductor measured and simulated (b) quality factor (1.5 turn inductor with an outer radius of 4mm, and 600um thick lines)

For simplicity a two element filter is chosen with a cut off frequency of 2.0 GHz. The filter was tuned in a full wave EM simulation using Ansoft HFSS to finalize the layout, shown in Figure 6-17 (a).
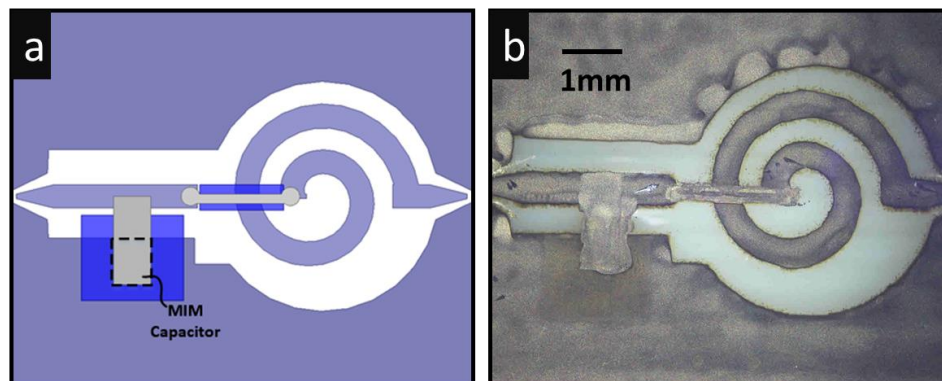
Figure 6-17: (a) 3D Printed Filter with inductor and capacitor structure (b) EM simulation of the filter

From the depicted 3D simulation Figure 6-17 (a) shows areas for the inductor cross over and dielectric of the capacitor clearly marked. The layout was fabricated with the same dimensions as the simulation, shown in the microscope image Figure 6-17 (b). The measured frequency response of the filter matches well with the simulation with a 3dB cutoff at 2GHz. The filter has no ripple in the passband and an insertion loss of 0.8 dB at

1GHz, Figure 6-18 (b). As seen from the zoomed in filter response Figure 6-18 (a) a

rejection near 10 dB at 3GHz and better than 20dB at 4 GHz is achieved.
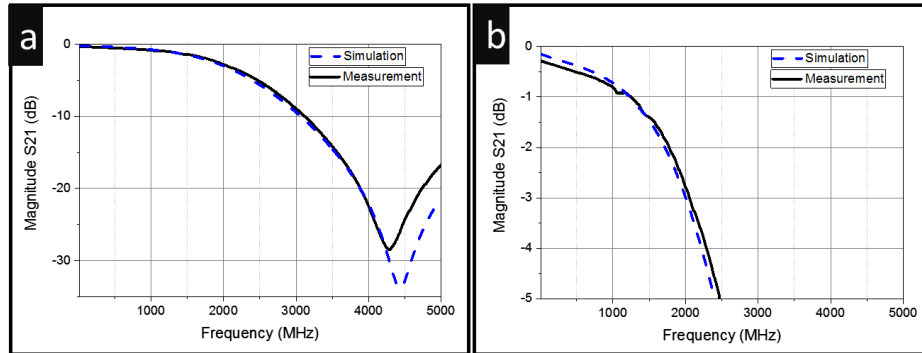
Figure 6-18: (a) Measured and simulated filter response. (b) Zoomed in view of the filter response.

The low insertion loss is excellent for a printed filter especially considering the

temperature constraints of 80°C. These results show that there is promise for

development of more complex RF designs using this 3D inkjet process.

6.6   3D inkjet printed antenna

The printed antenna work in this section was done prior to the development of the AOC

ink discussed throughout this chapter. However, it is correct to end on this application

since the 3D printed antenna demonstrates the unique possibilities that 3D fabrication

can offer in creating complex shapes that improve RF passive performance. It also serves

as a comparison and highlights the benefit of the AOC ink since the silver nanoparticle

ink was only able to achieve a conductivity ~1×10^6 S/m (even after selective laser

sintering) while the AOC ink achieved 1×10^7 S/m conductivity. The fabrication process is

similar to the previous section (also utilizing 3D inkjet printing) but uses a 3D systems

inkjet printer with Visijet UV cure polymer. The Visijet UV polymer was found to have

similar dielectric properties to the Stratasys Vero material. One advantage of the 3D

systems material is that the surfaces were smoother, ~100nm RMS roughness. The silver

nanoparticle ink was jetted on to the surface dried at 80°C and then annealed with an IR

laser to improve conductivity achieving $1x10^6$ S/m (about 1.6% the conductivity of bulk

silver). However, the design of the antenna itself is robust against conductivity and is

still able to achieve an impressive 81% efficiency and 8dBi of gain. The antenna is

designed with a honeycomb substrate which minimizes material consumption. This

reduces the weight, dielectric constant and dielectric loss which are all beneficial. The

antenna is entirely inkjet printed including the ground plane conductor. The honeycomb

substrate weighs twenty times less than a solid substrate. For comparison the

honeycomb antenna provides an efficiency nearly 15% greater than a similarly

fabricated antenna with a solid substrate and 5.7dBi of gain.

Three inks are used to fabricate the antenna; a wax material, a UV-cured polymer, and a

silver nanoparticle ink. The wax and polymer are used to form the 3D structure. They

are printed with a 3DSystems 5500 Multijet printer that has 1236 inkjet nozzles and can

eject ~2.5 Kg of material per hour. The printer has a spatial resolution of 33 × 33 × 29

μm in x, y and z directions. The polymer material is printed and cured layer by layer with

UV lights. The wax is a support material deposited in unison, it encases the UV-cured

polymer and supports any overhangs. In Figure 6-19 (a) the wax material can be seen

encasing the polymer which is subsequently melted and washed off Figure 6-19 (b). The

final antenna with printed silver is also shown in Figure 6-19 (c).
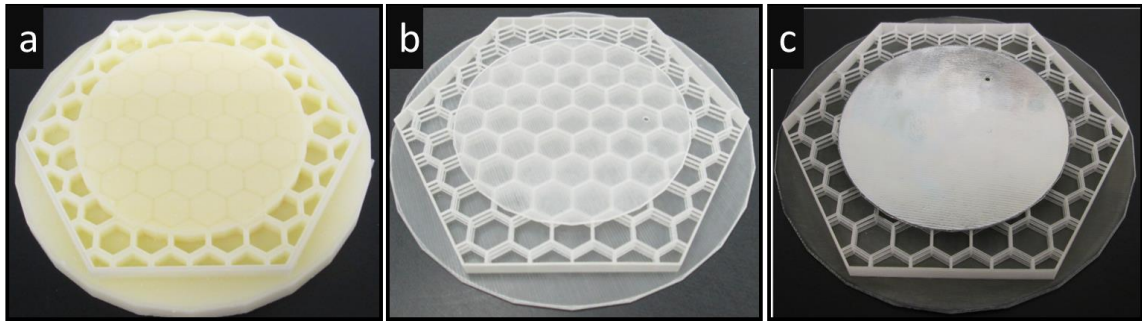
Figure 6-19: (a) Multijet printed structure with wax support material, (b) remaining polymer shell after melting the wax (c), final antenna with inkjet printed silver ink.

A Dimatix 2831 inkjet printer is used to print the silver nanoparticle ink (Sigma Aldrich Silver Ink 719048) with a disposable 10 Pico-liter 16 nozzle head. While it is best to print all materials within the same printer, the nanoparticle ink is not stable enough to use with non-disposable inkjet-heads as they will eventually clog the nozzles.

After UV-curing, the polymer material is rigid, with good mechanical properties similar to polycarbonate. It is not an ideal radio frequency dielectric though, with a dissipation factor of around 0.02. The material has been characterized from 10 MHz to 1 GHz with an Agilent E4991 impedance analyzer and dielectric test fixture 16453A, results are shown in Figure 6-20.
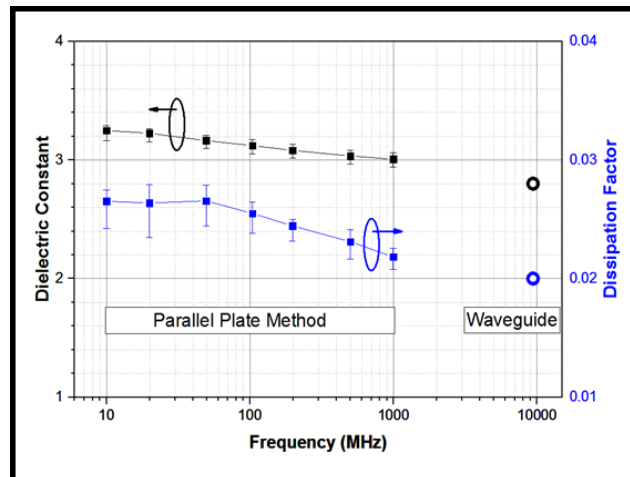
Figure 6-20: Dielectric properties of 3DSystems UV-Cure Polymer Material (Hard Acrylic based). Bars represent the maximum and minimum measurement values of five test samples with the parallel plate method while filled squares are the average value. Circular data point at 9.375 GHz is from a waveguide measurement.

Measurement of five different samples shows there is a range especially in the dissipation factor at low frequency. A single waveguide test done at Delsen Labs in California USA characterized the material at 9.375 GHz and is also plotted in Figure 6-20 and shown as a circle. The dielectric shows some dispersion with increasing frequency, ranging from 3.2 in the low MHz to 2.8 at 9.375 GHz. Although the precise value of dissipation factor is difficult to measure, it is around 0.03 - 0.02 over this frequency range.

A major benefit of 3D printing is that complex internal features can easily be fabricated, which would be difficult to realize with traditional tooling. The honeycomb substrate used in this work provides a reduced dielectric constant and improved dissipation factor which are both desirable for antenna performance. The use of a planarizer which levels the material as it is being printed provides smooth finished surfaces. Atomic force

microscopy scans of the printed surfaces show roughness better than 100 nm root mean

square for the UV-polymer seen in Figure 6-21 (a).
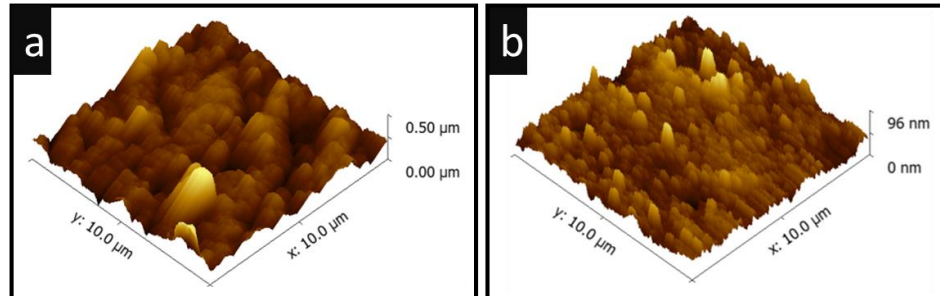
Figure 6-21: (a) Atomic force microscopy inkjet printed polymer material surface 95 nm root mean square roughness. (b) Inkjet printed Silver nanoparticle surface, 11 nm root mean square roughness.

This is a major improvement over 3D printed surfaces in [54] [123] with 10-30 μm of

roughness. The silver nanoparticle ink in this work is printed at 30°C and is fluid after

being deposited. This allows the ink to be very smooth with root mean square

roughness of 11 nm as shown in Figure 6-21(b). Although nanoparticle sintering occurs

at reduced temperature relative to bulk metal, temperatures above 180°C are best.

However, these temperatures are above the glass transition point for the UV-cured

polymer. In order to achieve conductivity at much lower temperature a laser sintering

process is used [63]. A total of six silver layers are printed, three layers at a time and

partial dried at 80°C to avoid excessive ink spreading. After the six layers are printed and

dried, laser sintering is performed; this takes about 15 minutes. A CO_2 engraving laser

(Universal Laser system PLS6.75) operated at 60W and a speed of 30 cm/s defocused 20

mm above the silver ink and giving 1000 pulses per inch is utilized. The final thickness of

the printed silver is approximately 3.5 um measured by a Dektak profilometer. It should

be noted that both the patch and the ground plane are printed in this way. The antenna

is probe-fed using a coaxial connector shown in *Figure 6-22*(b).
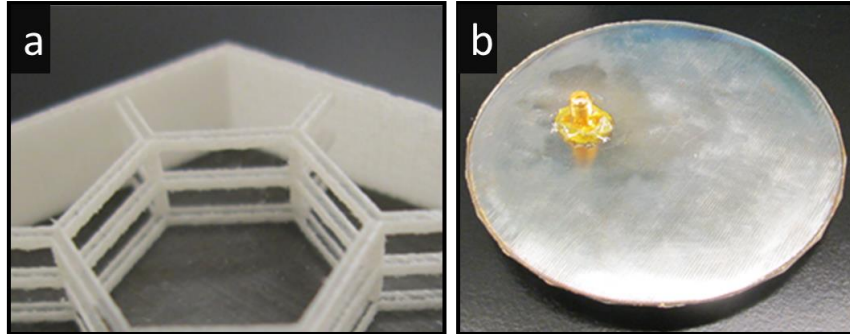
Figure 6-22: (a)Zoomed in view of honeycomb (b), back of antenna with probe feed.

Since soldering the thin nanoparticle silver is not possible, a silver epoxy (Duralco 120) is

used. A non-conductive epoxy (Loctite Quickset) is used on top for additional strength.

6.7   Antenna design

The patch antenna is one of the simplest and most well studied antennas. They are

popular because they are planar, low profile, and can provide different polarizations.

The linearly polarized patches in this work, are designed to operate at 2.4 GHz, a

popular industrial scientific and medical band. Two patches are compared, the first

antenna has a solid 3D printed substrate. Both honeycomb and solid substrate patches

are fabricated using the same process and materials. The second antenna is a

honeycomb structure which is meant to emulate air while maintaining structural

support. Each hexagon has 4.5 mm length sides and the beams are 500um thick shown

in *Figure 6-22*(a).

For the honeycomb structure, the dielectric constant and dissipation factor were

estimated to be 1.1 and $2e^{-3}$ respectively. This estimate was made by calculating the

volume filling factor of the honeycomb and using a weighted average. The effective

dielectric properties were used to simplify the simulation of the honeycomb structure

and save computing time. Although this method is not the most accurate it provides a

sufficient estimate for this work; as shown in [56]. A near field Satimo Star lab system is

used to measure the antennas. The antenna radiation efficiency is measured to be 81%

and 67% respectively. The simulated efficiency for comparison is 84% and 71%.

Simulations show that by doubling the printed silver layers to 12 the efficiency of the

honeycomb substrate could be pushed to 91%. From Table 6-3 it is clear that the gain

has increased and that efficiency is improved in the case of the honeycomb structure.

Table 6-3: Antenna Parameters

Antenna	Patch Radius (mm)	Substrate Thickness (mm)	Center Frequency (GHz)	Total Weight (gram)	Peak Gain (dBi)	Radiation Efficiency (%)
Solid Substrate	20	5.0	2.4	35.0	5.7	67
Honeycomb Substrate	32	5.0	2.4	5.8	8.0	81
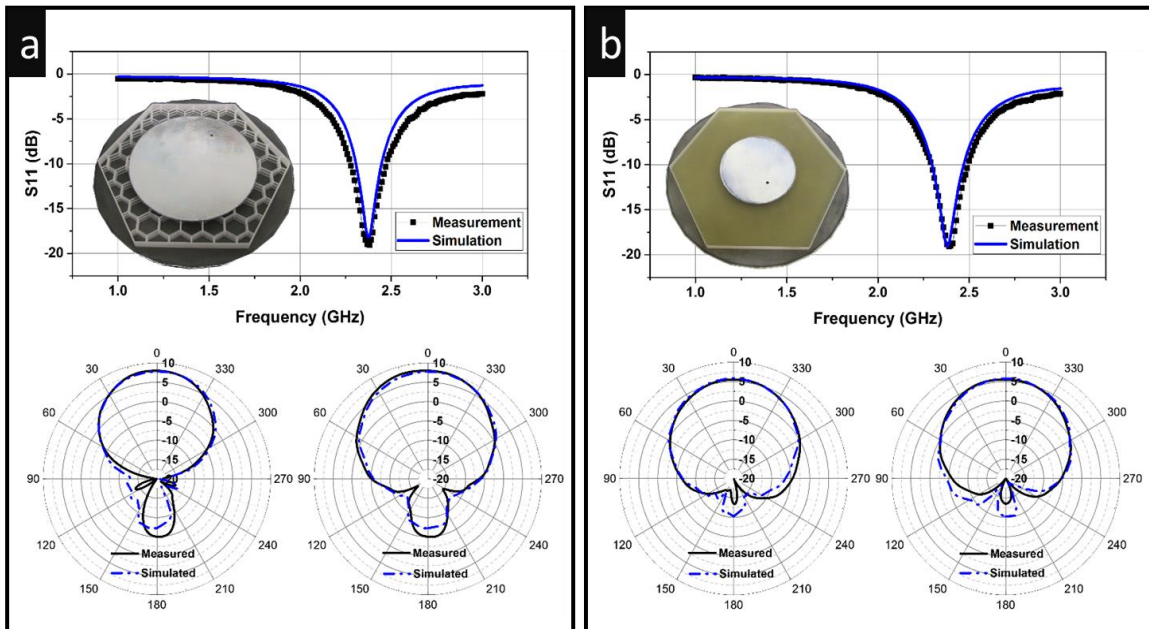
Figure 6-23: (a) Measurements and simulations of the honeycomb patch antenna, magnitude of S11 versus frequency (top), E-plane radiation pattern cut (bottom left), H-plane cut (bottom right) (b) Measurements and simulations of the solid substrate patch antenna.

Both patches are matched well at 2.4 GHz as shown in Figure 6-23. The air like dielectric

substrate provides a larger patch with 32 mm radius however the weight is reduced to

only 5.8 grams including the connector. An interesting observation is seen when

comparing the E and H plane cuts at low elevation angles (50° to 90°) for the solid

substrate antenna Figure 6-23(b). The patterns are equalized, which is not the case for

the honeycomb antenna at low elevation. This is true for both the simulations and

measurements. The phenomenon of equalizing the E and H plane patterns at low

elevation angles is shown in [124] and occurs at a specific combination of dielectric

constant and ground plane size for the circular patch. This phenomenon could be used

to make antennas with high purity polarization at low elevation angles, beneficial in

precision global positioning applications.

6.8   Conclusions

Inkjet printing is transitioning from solely a graphic arts medium into a useful fabrication

tool. The ability to deposit multiple materials and the scalability of inkjet systems with

thousands of nozzles makes it possible to realize large and complex parts. A process is

presented where inkjet printed UV-cured polymer, and silver ink are integrated

together. A major challenge is integrating a metal with the low temperature UV cure

plastic material. A novel silver-organo-complex ink has been deployed, developed in-

house which provides a conductivity of $1x10^7$ S/m at 80°C in order to combine the

materials effectively. A silver nanoparticle ink was also investigated and with selective

laser sintered without damaging the surrounding UV-cure polymer the ink was pushed

to a conductivity of $1x10^6$ S/m. Both a fully inkjet printed filter and antenna are

demonstrated. The filter uses an inductor and capacitor to demonstrate the first fully inkjet printed lumped element filter. The capacitor and inductor exhibit state-of-the-art quality factors of ~20 and 8 respectively in the radio frequency regime. The low pass filter has an insertion loss of 0.8 dB at 1GHz. For the antenna, the true benefit of 3D printing is exploited by employing a complex honeycomb structure. This lowers the dielectric constant and improves the dissipation factor by emulating air. The antenna is entirely inkjet printed including the ground plane, and achieves an impressive 81% efficiency with 8 dBi of gain. With future advances in printed metals, performance could one day overcome conventional fabrication methods.

Chapter 7 -Conclusions and future work

7.1   Summary

This work focuses on RF passives specifically capacitors and inductors, although an

antenna is also demonstrated within the 3D inkjet printing process in chapter 6. There

have been plenty of reports on printed conductors for RF passives, mostly antennas.

Printing of dielectrics is a much less studied area, and there have only been a few

reports of to-date of RF inductors and capacitors in the literature. In this thesis, inkjet

printing is utilized as the fabrication method, with three main dielectric materials

explored. These are; a sol-gel derived alumina ceramic, a thermally crosslinked polymer

poly 4(vinyl phenol), and a UV cure acrylic polymer. A summary of each of these

respective materials and chapters follows:

7.1.1   Inkjet printed alumina for RF MIM capacitors

An experimental method for producing sol-gel derived alumina films was loosely based

on previous spin-coating reports in literature. The goal was to move away from spin-

coating to inkjet print the films and create RF MIM capacitors for the first time. Two

precursors, aluminum chloride and aluminum nitrate were investigated. It was found

that aluminum nitrate was the more stable choice in ambient environment. An inkjet

recipe was developed with this sol-gel solution using ethanol additive to reduce capillary

driven spreading and suppress coffee ring effect. Fairly uniform ~110nm thick films were

printed in three ~35nm passes with a 400°C annealing step between each printing pass.

The capacitance density of the films is more than 400pF/mm^2. Capacitors were

demonstrated with 2x10^{-9} A/cm^2 current density at a field strength of 1MV/cm. A 20pF

capacitor shows a self-resonance frequency of 1.9 GHz. The 20pF capacitor has a Q of 200 at low frequency, dropping to 20 at 500 MHz. These are all promising results but a concern for the printing process is the variation in capacitor value due to thickness variation. Capacitors were shown to have a thickness variation of 6%, which is quite high considering the often tight tuning tolerances of RF circuits. It is expected that by further optimization of the ink formulation and appropriate surface treatment that the variation could be reduced. The 400°C annealing temperature is also an issue since this eliminates the possibility of using a plastic substrate. Mature vacuum deposited ALD alumina films are typically deposited at 300°C which is still beyond the limits of plastics. The high temperature also restricts integration of any low temperature polymers or oxidizing metals. Further research into ink formulation and alternative heating methods (IR heating, photo sintering, UV, microwave, etc.) has potential to reduce the temperature and would be beneficial.

7.1.2   Multilayer inkjet printed RF passives with PVP polymer

Inkjet printed multilayer capacitors and inductors with through vias have been demonstrated using poly (4-vinyl phenol) and silver nanoparticle ink. This process provides a first step towards fabricating by inkjet printing, radio frequency matching circuits and filters. A glass substrate is used as the mechanical support in this work; however the process can be applied to other smooth surfaces that can withstand temperatures of 180°C. A key advantage to the process is that inkjet printed dissolving vias are shown to be repeatable with less than 0.1 ohms resistance. A wide range of printed RF MIM capacitors from 16 pF to 50 pF are shown. And self-resonant

frequencies into the GHz regime. Complex spiral inductors have been demonstrated, a 9.7 nH inductor is shown to have a self-resonant frequency of 850 MHz and maximum quality factor of 4.4. Large value inductors up to 75 nH with a footprint of 42 mm^2 and Q of 3.3 have also been fabricated. The quality factors are relatively low compared to conventional capacitors using microwave dielectrics. These results draw attention to the fact that resistive printed conductors and poor dissipation factor in solution processed PVP is an issue for RF passives. In the future other materials such as fluoropolymers or solution processed oxides with lower dissipation factor can be investigated to improve the performance of printed capacitors. Inductors are less sensitive to the dielectric but both RF inductors and capacitors are highly sensitive to the conductivity and thickness of the metal used. Silver nanoparticle ink has its limitations, showing 1×10^7 S/m conductivity in this work, about 15% of bulk silver. Conductive ink is a fast moving area of research and new types of inks have shown promise for higher conductivities at low temperature. This is early work on printed RF passive devices and with new materials and printing process it has a promising future.

7.1.3 3D inkjet printed passives

Inkjet printing with high throughput industrial print-heads has led to the relatively new field of 3D inkjet printing of acrylic objects. Single print heads are capable of ejecting >2Kg of material per hour, and shows the real potential of inkjet printing as a fast and low cost fabrication method. Using the UV cure polymers common in inkjet 3D printers, a multilayer process is developed with integrated metal. The major challenge is temperature compatibility of a printed metal with the low temperature UV cure

polymer. A novel silver organo-metallic ink is utilized at 80°C providing a conductivity of 1×10^7 S/m. Using crossovers to connect between the layers inductors are demonstrated with quality factors ~7 and capacitors with Q's approaching 20, into the GHz regime. The first fully inkjet printed lumped element RF filter is demonstrated with an insertion loss of 0.8 dB at 1GHz. Another application which demonstrates the true potential of 3D inkjet printing is an antenna, where a complex internal structure is fabricated inside of the substrate. The structure both reduces weight and material while improving antenna performance. An antenna efficiency of 81% and gain of 8 dBi is achieved at 2.4 GHz. This demonstrates the possibilities of creating interesting and high performance RF passives. While the metal conductivity is a concern, the high dielectric loss of the UV cure polymers used today are also limiting. The development of a low loss dielectric that could be rapidly UV cured while having good mechanical properties would be a major milestone for 3D inkjet printed RF passives.

7.2   Future Directions

7.3   Low loss inkjet printed dielectric

The search is on for a suitable low loss dielectric material. Although alumina was developed showing low loss of 0.005 within this thesis. The high processing temperature (400°C) of alumina is undesirable for many applications. The ideal material would be easily inkjet printed, be an excellent insulator, and have a low processing temperature. Although fluoropolymers are among the lowest loss materials known, they are also very hydrophobic (think of non-stick Teflon surfaces) which is undesirable in a multilayer inkjet printing process. Polystyrene may be a good candidate as it has low loss and has

been used commercially for capacitors. It has also been inkjet printed in the detailed study by E. Teken et al. [125].

7.4   Improved inkjet printed conductors

While there has been investigation into nanoparticle inks for more than a decade, they are mostly used in research setting and have not had wide spread commercial success. For RF passives, high conductivity is paramount. Passives become more sensitive to conductivity as a function of frequency due to the skin effect. Essential as the AC field changes more rapidly the magnetic field concentrated at the center of the conductor forces the current to flow mostly at the perimeter of the conductor. High conductivity is therefore key at radio frequencies, and printed conductors have shown promise. The AOC ink developed within this group has been able to double the quality factor of inductors even at a lower temperature. New ink formulation and different sintering techniques such as photo-sintering, or laser sintering which do not damage the underlying substrate are attractive. Inkjet printed RF passives with high conductivity that rival traditional fabrication methods look promising in the near future.

7.5   Unconventional printed RF designs for improved performance

Conventional RF designs have unsurprisingly been built around traditional fabrication methods. Inkjet printing allows for large area and interesting complex geometries to be fabricated. This can open the door to many new designs with improved performance that were unthinkable before. The honeycomb substrate antenna is an example of this. Other designs are possible, that take advantage of printing thin layers of dielectric or complex shapes. A new printed stacked type of hair pin filter is proposed which is

unpublished and under development, in collaboration with Eyad Arabi from our

research group at KAUST. This design takes into advantage the large area coupling

possible with multilayer inkjet printed fabrication. The coupling allows for interesting

ultra-wide bandwidth filter designs which are useful for recently designated ultra-

wideband frequency spectrum. Many other performance enhancing RF designs are likely

possible with the versatile fabrication options that inkjet printing offers.

REFERENCES

[1] C. D. Dimitrakopoulos and D. J. Mascaro, "Organic thin-film transistors: A review of recent advances," *IBM J. Res. Dev.*, vol. 45, no. 1, pp. 11–27, Jan. 2001.

[2] H. Klauk, "Organic thin-film transistors," *Chem. Soc. Rev.*, vol. 39, no. 7, p. 2643, 2010.

[3] Dupont, "Data sheet and processing guide -Teflon Af - amorphous fluoroplastic resin." 2013.

[4] Dupont, "Fluoroplastic Comparison - Typical Properties," *Dupont.com*, 2013. [Online]. Available: www.dupont.com/Teflon_Industrial. [Accessed: 25-Sep-2013].

[5] Y.-Z. Lee, C.-P. Liu, S.-M. Wang, C.-H. Chen, C.-W. Wang, M.-H. Yang, K. Cheng, and J. Chang, "Ink-Jet Printed Passive Electronic Components: Metal-Insulator-Metal Device," in *Pacific Rim Conference on Lasers and Electro-Optics, 2005. CLEO/Pacific Rim 2005*, 2005, pp. 918–919.

[6] Y.-Y. Noh, N. Zhao, M. Caironi, and H. Sirringhaus, "Downscaling of self-aligned, all-printed polymer thin-film transistors," *Nat. Nanotechnol.*, vol. 2, no. 12, pp. 784–789, Nov. 2007.

[7] J. Puigdollers, "Pentacene thin-film transistors with polymeric gate dielectric," *Org. Electron.*, vol. 5, no. 1–3, pp. 67–71, Mar. 2004.

[8] Milena Keleva, "Poly (methyl methacrylate) (PMMA)." Technical University of Gabraovo, 2005.

[9] H.-Y. Tseng, "Scaling of Inkjet-Printed Transistors using Novel Printing Techniques," EECS Department, University of California, Berkeley, 2011.

[10] H.-Y. Tseng and V. Subramanian, "All inkjet printed self-aligned transistors and circuits applications," in *Electron Device Meetings IEDM*, 2009, pp. 1–4.

[11] B. S. Cook, J. Cooper, and M. Tentzeris, "Multi-Layer RF Capacitors on Flexible Substrates Utilizing Inkjet Printed Dielectric Polymers," *IEEE Microw. Wirel. Compon. Lett.*, Jul. 2013.

[12] K. Nomura, H. Ohta, A. Takagi, T. Kamiya, M. Hirano, and H. Hosono, "Room-temperature fabrication of transparent flexible thin-film transistors using amorphous oxide semiconductors," *Nature*, vol. 432, no. 7016, pp. 488–492, Nov. 2004.

[13] E. Fortunato, P. Barquinha, and R. Martins, "Oxide Semiconductor Thin-Film Transistors: A Review of Recent Advances," *Adv. Mater.*, vol. 24, no. 22, pp. 2945–2986, Jun. 2012.

[14] M. D. Stamate, "On the dielectric properties of dc magnetron TiO2 thin films," *Appl. Surf. Sci.*, vol. 218, no. 1–4, pp. 318–323, Sep. 2003.

[15] J. Jang, H. Kang, H. C. N. Chakravarthula, and V. Subramanian, "Fully Inkjet-Printed Transparent Oxide Thin Film Transistors Using a Fugitive Wettability Switch," *Adv. Electron. Mater.*, vol. 1, no. 7, p. n/a–n/a, Jul. 2015.

[16] Emerson and Cuming Microwave Division, "Dielectric Materials Chart." eccosorb, 2012.

[17] H. S. Nalwa, Ed., *Handbook of low and high dielectric constant materials and their applications*. San Diego: Academic Press, 1999.

[18] A. J. Moulson and J. M. Herbert, *Electroceramics: materials, properties, applications*, 2nd ed. West Sussex ; New York: Wiley, 2003.

[19] W. Y. Ching and Y.-N. Xu, "First-Principles Calculation of Electronic, Optical, and Structural Properties of alpha-Al2O3," *J. Am. Ceram. Soc.*, vol. 77, no. 2, pp. 404–411, Feb. 1994.

[20] S.-D. Mo and W. Y. Ching, "Electronic and optical properties of θ − Al 2 O 3 and comparison to α − Al 2 O 3," *Phys. Rev. B*, vol. 57, no. 24, pp. 15219–15228, Jun. 1998.

[21] Hu Hang, "High-K Dielectric MIM Capaictors for Silicon RF and Analog Applications," National University of Singapore, Singapore, 2003.

[22] S. Prasanna, G. Krishnendu, S. Shalini, P. Biji, G. Mohan Rao, S. Jayakumar, and R. Balasundaraprabhu, "Composition, structure and electrical properties of DC reactive

magnetron sputtered Al2O3 thin films," *Mater. Sci. Semicond. Process.*, vol. 16, no. 3, pp. 705–711, Jun. 2013.

[23] J. Antula, "Effect of positive ionic space charge on electrical capacitance and schottky current in thin Al2O3 films," *Thin Solid Films*, vol. 4, no. 4, pp. 281–289, Oct. 1969.

[24] H. Birey, "Dielectric properties of aluminum oxide films," *J. Appl. Phys.*, vol. 49, no. 5, pp. 2898–2904, May 1978.

[25] G. Dittmer, "Electron conduction, electron emission and electroluminescence of MIM sandwich structures with Al2O3 insulating layers," *Thin Solid Films*, vol. 9, no. 2, pp. 141–172, Feb. 1972.

[26] A. Roy Bardhan, P. C. Srivastava, A. Chatterjee, and D. L. Bhattacharya, "Electron transport mechanisms in very thin Al_2O_3 films," *Int. J. Electron.*, vol. 40, no. 4, pp. 313–321, Apr. 1976.

[27] J. Yota, H. Shen, and R. Ramanathan, "Characterization of atomic layer deposition HfO2, Al2O3, and plasma-enhanced chemical vapor deposition Si3N4 as metal–insulator–metal capacitor dielectric for GaAs HBT technology," *J. Vac. Sci. Technol. Vac. Surf. Films*, vol. 31, no. 1, p. 01A134, 2013.

[28] J. Yota, "ALD HfO2 and Al2O3 as MIM Capacitor Dielectric for GaAs HBT Technology," *ECS Trans.*, vol. 53, no. 1, pp. 281–294, May 2013.

[29] Y. L. Tu, H. L. Lin, L. L. Chao, D. Wu, C. S. Tsai, C. Wang, C. F. Huang, C. H. Lin, and J. Sun, "Characterization and comparison of high-k metal-insulator-metal (MiM) capacitors in 0.13 μm Cu BEOL for mixed-mode and RF applications," 2003, pp. 79–80.

[30] J. Zhou, H. Chang, H. Liu, G. Liu, W. Xu, Q. Li, S. Li, Z. He, and H. Li, "MIM capacitors with various Al_2O_3 thicknesses for GaAs RFIC application," *J. Semicond.*, vol. 36, no. 5, p. 054004, May 2015.

[31] J. Murray, "Sputter deposition of thin-film capacitors onto low temperature co-fired ceramic substrates," Missouri University of Science and Technology, 2012.

[32] H. Hu, S.-J. Ding, H. F. Lim, C. Zhu, M. F. Li, S. J. Kim, X. F. Yu, J. H. Chen, Y. F. Yong, B. J. Cho, D. S. H. Chan, S. C. Rustagi, M. B. Yu, C. H. Tung, A. Du, D. My, P. D. Foot, A. Chin, and D.-L. Kwong, "High performance ALD HfO/sub 2/-Al/sub 2/O/sub 3/ laminate MIM capacitors for RF and mixed signal IC applications," in *Electron Devices Meeting, 2003. IEDM '03 Technical Digest. IEEE International*, 2003, pp. 15.6.1–15.6.4.

[33] G. Yip, J. Qiu, W. T. Ng, and Z. H. Lu, "Effect of metal contacts on the electrical characteristics of Al[sub 2]O[sub 3] dielectric thin films," *Appl. Phys. Lett.*, vol. 92, no. 12, p. 122911, 2008.

[34] C. Avis and J. Jang, "High-performance solution processed oxide TFT with aluminum oxide gate dielectric fabricated by a sol–gel method," *J. Mater. Chem.*, vol. 21, no. 29, p. 10649, 2011.

[35] S. H. Kim, I. Kang, Y. G. Kim, H. R. Hwang, Y.-H. Kim, S.-K. Kwon, and J. Jang, "High performance ink-jet printed diketopyrrolopyrrole-based copolymer thin-film transistors using a solution-processed aluminium oxide dielectric on a flexible substrate," *J. Mater. Chem. C*, vol. 1, no. 13, p. 2408, 2013.

[36] P. K. Nayak, M. N. Hedhili, D. Cha, and H. N. Alshareef, "High performance In2O3 thin film transistors using chemically derived aluminum oxide dielectric," *Appl. Phys. Lett.*, vol. 103, no. 3, p. 033518, 2013.

[37] B. Hu, M. Yao, P. Yang, W. Shan, and X. Yao, "Preparation and dielectric properties of dense and amorphous alumina film by sol–gel technology," *Ceram. Int.*, vol. 39, no. 7, pp. 7613–7618, Sep. 2013.

[38] J. Peng, Q. Sun, S. Wang, H.-Q. Wang, and W. Ma, "Low-temperature solution-processed alumina as gate dielectric for reducing the operating-voltage of organic field-effect transistors," *Appl. Phys. Lett.*, vol. 103, no. 6, p. 061603, 2013.

[39] D.-H. Lee, S.-Y. Han, G. S. Herman, and C. Chang, "Inkjet printed high-mobility indium zinc tin oxide thin film transistors," *J. Mater. Chem.*, vol. 19, no. 20, p. 3135, 2009.

[40] H. W. Jang, J. Kim, H. Kim, Y. Yoon, S. Lee, H. Hwang, and J. Kim, "Fabrication of Nonsintered Alumina–Resin Hybrid Films by Inkjet-Printing Technology," *Jpn. J. Appl. Phys.*, vol. 49, no. 7, p. 071501, Jul. 2010.

[41] M. Hwang, J. Kim, H. Kim, Y. Yoon, S. Hyun, J. Kim, S. Lee, and J. Moon, "Inkjet-printing of nonsintered alumina-resin hybrid films and their dielectric properties," *J. Appl. Phys.*, vol. 108, no. 10, p. 102809, 2010.

[42] A. K. Mogalicherla, S. Lee, P. Pfeifer, and R. Dittmeyer, "Drop-on-demand inkjet printing of alumina nanoparticles in rectangular microchannels," *Microfluid. Nanofluidics*, vol. 16, no. 4, pp. 655–666, Apr. 2014.

[43] A. R. Maza, B. Cook, G. Jabbour, and A. Shamim, "Paper-based inkjet-printed ultra-wideband fractal antennas," *IET Microw. Antennas Propag.*, vol. 6, no. 12, p. 1366, Nov. 2012.

[44] B. S. Cook and A. Shamim, "Inkjet Printing of Novel Wideband and High Gain Antennas on Low-Cost Paper Substrate," *IEEE Trans. Antennas Propag.*, vol. 60, no. 9, pp. 4148–4156, Sep. 2012.

[45] D. Redinger, S. Molesa, S. Yin, R. Farschi, and V. Subramanian, "An Ink-Jet-Deposited Passive Component Process for RFID," *IEEE Trans. Electron Devices*, vol. 51, no. 12, pp. 1978–1983, Dec. 2004.

[46] S. Molesa, D. Redinger, D. Huang, and V. Subramanian, "High-Quality inkjet-printed multilevel interconnects and inductive components on plastic for ulra low cost RFID applications," in *Flexible Electronics - Materials and Device Technology*, San Francisco California USA, July, 2003, vol. 769.

[47] B. J. Kang, C. K. Lee, and J. H. Oh, "All-inkjet-printed electrical components and circuit fabrication on a plastic substrate," *Microelectron. Eng.*, vol. 97, pp. 251–254, Sep. 2012.

[48] A. Chiolerio, G. Maccioni, P. Martino, M. Cotto, P. Pandolfi, P. Rivolo, S. Ferrero, and L. Scaltrito, "Inkjet printing and low power laser annealing of silver nanoparticle traces for the realization of low resistivity lines for flexible electronics," *Microelectron. Eng.*, vol. 88, no. 8, pp. 2481–2483, Aug. 2011.

[49] A. B. Menicanin, L. D. Zivanov, M. S. Damnjanovic, and A. M. Maric, "Low-Cost CPW Meander Inductors Utilizing Ink-Jet Printing on Flexible Substrate for High-Frequency Applications," *IEEE Trans. Electron Devices*, vol. 60, no. 2, pp. 827–832, Feb. 2013.

[50] H. Sirringhaus, T. Kawase, R. H. Friend, T. Shimoda, M. Inbasekaran, W. Wu, and E. P. Woo, "High-Resolution Inkjet Printing of All-Polymer Transistor Circuits," *Science*, vol. 290, no. 5499, pp. 2123–2126, Dec. 2000.

[51] T. Kawase, H. Sirringhaus, R. H. Friend, and T. Shimoda, "Inkjet Printed Via-Hole Interconnections and Resistors for All-Polymer Transistor Circuits," *Adv. Mater.*, vol. 13, no. 21, pp. 1601–1605, Nov. 2001.

[52] T. Snyder, M. Andrews, M. Weislogel, P. Moeck, and D. Adams, "3D Systems' Technology Overview and New Applications in Manufacturing," *3D Print. Addit. Manuf.*, vol. 1, no. 3, pp. 169 –176, Sep. 2014.

[53] J.-C. S. Chieh, B. Dick, S. Loui, and J. D. Rockway, "Development of a Ku-Band Corrugated Conical Horn Using 3-D Print Technology," *IEEE Antennas Wirel. Propag. Lett.*, vol. 13, pp. 201–204, 2014.

[54] H. H. Tsang, J. H. Barton, R. C. Rumpf, and C. R. Garcia, "Effects of extreme surface roughness on 3D printed horn antenna," *Electron. Lett.*, vol. 49, no. 12, pp. 734–736, Jun. 2013.

[55] P. Deffenbaugh, J. Goldfarg, X. Chen, and K. Church, "Fully 3D Printed 2.4 GHz Bluetooth/Wi-Fi Antenna," in *46th International Symposium on Microelectronics*, Orlando, 2013, pp. 1–7.

[56] M. Liang, W.-R. Ng, K. Chang, K. Gbele, M. E. Gehm, and H. Xin, "A 3-D Luneburg Lens Antenna Fabricated by Polymer Jetting Rapid Prototyping," *IEEE Trans. Antennas Propag.*, vol. 62, no. 4, pp. 1799–1807, Apr. 2014.

[57] P. Nayeri, M. Liang, R. A. Sabory-Garcia, M. Tuo, F. Yang, M. Gehm, H. Xin, and A. Z. Elsherbeni, "3D Printed Dielectric Reflectarrays: Low-Cost High-Gain Antennas at Sub-Millimeter Waves," *IEEE Trans. Antennas Propag.*, vol. 62, no. 4, pp. 2000–2008, Apr. 2014.

[58] S.-Y. Wu, C. Yang, W. Hsu, and L. Lin, "3D-printed microelectronics for integrated circuitry and passive wireless sensors," *Microsyst. Nanoeng.*, vol. 1, p. 15013, Jul. 2015.

[59] "Data Sheet - Cabot Conductive Ink CCI-300," *Cabot Corp.* [Online]. Available: www.cabot-corp.com. [Accessed: 25-Sep-2013].

[60] E. Geterud, Bergmark, Pontus, and Yang, Jian, "Lightweight Waveguide and Antenna Components Using Plating on Plastics," in *European Conference Antennas and Propagation*, Gothenburg, 2013, pp. 1812–1815.

[61] C. Paquet, R. James, A. J. Kell, O. Mozenson, J. Ferrigno, S. Lafrenière, and P. R. L. Malenfant, "Photosintering and electrical performance of CuO nanoparticle inks," *Org. Electron.*, vol. 15, no. 8, pp. 1836–1842, Aug. 2014.

[62] J. Perelaer, R. Jani, M. Grouchko, A. Kamyshny, S. Magdassi, and U. S. Schubert, "Plasma and Microwave Flash Sintering of a Tailored Silver Nanoparticle Ink, Yielding 60% Bulk Conductivity on Cost-Effective Polymer Foils," *Adv. Mater.*, vol. 24, no. 29, pp. 3993–3998, Aug. 2012.

[63] G. McKerricher, D. Conchouso, B. S. Cook, I. Foulds, and A. Shamim, "Crude oil water-cut sensing with disposable laser ablated and inkjet printed RF microfluidics," presented at the IEEE International Microwave Symposium, Tampa Florida, 2014, pp. 1–3.

[64] S. B. Walker and J. A. Lewis, "Reactive Silver Inks for Patterning High-Conductivity Features at Mild Temperatures," *J. Am. Chem. Soc.*, vol. 134, no. 3, pp. 1419–1421, Jan. 2012.

[65] D. B. Bogy and F. E. Talke, "Experimental and Theoretical Study of Wave Propagation Phenomena in Drop-on-Demand Ink Jet Devices," *IBM J. Res. Dev.*, vol. 28, no. 3, pp. 314–321, May 1984.

[66] D. Wallace, "Inkjet Microdispenser." Microfab Corp., Sep-2015.

[67] H. V. Panchawagh and S. K. Halwawala, "Imaging Models for Robust Single-pass Printing using SAMBA™ Piezo Drop-on-Demand Silicon MEMS (Si-MEMS) Inkjet Printheads," *NIP Digit. Fabr. Conf.*, vol. 2013, no. 1, pp. 206–210, Jan. 2013.

[68] C. Menzel, A. Bibl, and P. Hoisington, *MEMS Solutions for Precision Micro-fluidic Dispensing Application*. Springfield, Va: IS&T, the Society for Imaging Science and Technology, 2004.

[69] G. H. McKinley and M. Renardy, "Wolfgang von Ohnesorge," *Phys. Fluids*, vol. 23, no. 12, p. 127101, 2011.

[70] W. V. Ohnesorge, "Die Bildung von Tropfen an Düsen und die Auflösung flüssiger Strahlen," *ZAMM - J. Appl. Math. Mech. Z. Für Angew. Math. Mech.*, vol. 16, no. 6, pp. 355–358, 1936.

[71] B. Derby, "Inkjet Printing of Functional and Structural Materials: Fluid Property Requirements, Feature Stability, and Resolution," *Annu. Rev. Mater. Res.*, vol. 40, no. 1, pp. 395–414, Jun. 2010.

[72] Fujifilm, "Dimatix Material Printer DMP-2831 - Specification Sheet." Fujifilm Dimatix, 04-Apr-2013.

[73] D. Jang, D. Kim, and J. Moon, "Influence of Fluid Physical Properties on Ink-Jet Printability," *Langmuir*, vol. 25, no. 5, pp. 2629–2635, Mar. 2009.

[74] H. C. Nallan, J. A. Sadie, R. Kitsomboonloha, S. K. Volkman, and V. Subramanian, "Systematic Design of Jettable Nanoparticle-Based Inkjet Inks: Rheology, Acoustics, and Jettability," *Langmuir*, vol. 30, no. 44, pp. 13470–13477, Nov. 2014.

[75] J. M. Andreas, E. A. Hauser, and W. B. Tucker, "BOUNDARY TENSION BY PENDANT DROPS," *J. Phys. Chem.*, vol. 42, no. 8, pp. 1001–1019, Jan. 1937.

[76] F. M. Fowkes, "ATTRACTIVE FORCES AT INTERFACES," *Ind. Eng. Chem.*, vol. 56, no. 12, pp. 40–52, Dec. 1964.

[77] C. Rulison, "KRUSS Application Note 306." KRUSS Corp., 1999.

[78] S. Magdassi, Ed., *The chemistry of inkjet inks*. Singapore ; Hackensack, NJ: World Scientific, 2010.

[79] D. Soltman, B. Smith, S. J. S. Morris, and V. Subramanian, "Inkjet printing of precisely defined features using contact-angle hysteresis," *J. Colloid Interface Sci.*, vol. 400, pp. 135–139, Jun. 2013.

[80] R. D. Deegan, O. Bakajin, T. F. Dupont, G. Huber, S. R. Nagel, and T. A. Witten, "Capillary flow as the cause of ring stains from dried liquid drops," *Nature*, vol. 389, no. 6653, pp. 827–829, Oct. 1997.

[81] H. Hu and R. G. Larson, "Marangoni Effect Reverses Coffee-Ring Depositions," *J. Phys. Chem. B*, vol. 110, no. 14, pp. 7090–7094, Apr. 2006.

[82] R. Dou, T. Wang, Y. Guo, and B. Derby, "Ink-Jet Printing of Zirconia: Coffee Staining and Line Stability," *J. Am. Ceram. Soc.*, vol. 94, no. 11, pp. 3787–3792, Nov. 2011.

[83] J.-L. Lin, Z.-K. Kao, and Y.-C. Liao, "Preserving Precision of Inkjet-Printed Features with Solvents of Different Volatilities," *Langmuir*, vol. 29, no. 36, pp. 11330–11336, Sep. 2013.

[84] D. Soltman and V. Subramanian, "Inkjet-Printed Line Morphologies and Temperature Control of the Coffee Ring Effect," *Langmuir*, vol. 24, no. 5, pp. 2224–2231, Mar. 2008.

[85] S. Magdassi, M. Grouchko, O. Berezin, and A. Kamyshny, "Triggering the Sintering of Silver Nanoparticles at Room Temperature," *ACS Nano*, vol. 4, no. 4, pp. 1943–1948, Apr. 2010.

[86] P. K. Nayak, J. A. Caraveo-Frescas, Z. Wang, M. N. Hedhili, Q. X. Wang, and H. N. Alshareef, "Thin Film Complementary Metal Oxide Semiconductor (CMOS) Device Using a Single-Step Deposition of the Channel Layer," *Sci. Rep.*, vol. 4, Apr. 2014.

[87] M. Hartman, O. Trnka, and O. Šolcová, "Thermal Decomposition of Aluminum Chloride Hexahydrate," *Ind. Eng. Chem. Res.*, vol. 44, no. 17, pp. 6591–6598, Aug. 2005.

[88] C. Zhang, J. Miao, and N. Wang, "Rapid response relative humidity sensor using anodic aluminum oxide film," US8783101 B2, 22-Jul-2014.

[89] T. Islam, L. Kumar, and S. A. Khan, "A novel sol–gel thin film porous alumina based capacitive sensor for measuring trace moisture in the range of 2.5–25 ppm," *Sens. Actuators B Chem.*, vol. 173, pp. 377–384, Oct. 2012.

[90] C. Avis, H. R. Hwang, and J. Jang, "Effect Of Channel Layer Thickness On The Performance Of Indium–Zinc–Tin Oxide Thin Film Transistors Manufactured By Inkjet Printing," *ACS Appl. Mater. Interfaces*, vol. 6, no. 14, pp. 10941–10945, Jul. 2014.

[91] D.-H. Lee, Y.-J. Chang, W. Stickle, and C.-H. Chang, "Functional Porous Tin Oxide Thin Films Fabricated by Inkjet Printing Process." [Online]. Available: http://esl.ecsdl.org. [Accessed: 01-Nov-2015].

[92] P. Melnikov, V. A. Nascimento, I. V. Arkhangelsky, and L. Z. Z. Consolo, "Thermal decomposition mechanism of aluminum nitrate octahydrate and characterization of intermediate products by the technique of computerized modeling," *J. Therm. Anal. Calorim.*, vol. 111, no. 1, pp. 543–548, Jul. 2012.

[93] S. Evans, "Correction for the effects of adventitious carbon overlayers in quantitative XPS analysis," *Surf. Interface Anal.*, vol. 25, no. 12, pp. 924–930, Nov. 1997.

[94] G. C. Smith, "Evaluation of a simple correction for the hydrocarbon contamination layer in quantitative surface analysis by XPS," *J. Electron Spectrosc. Relat. Phenom.*, vol. 148, no. 1, pp. 21–28, Jul. 2005.

[95] Hien Do Ky, "Fabrication and Characterization of Microwave thin film MIM Capacitors," Carleton University, Canada, 1991.

[96] A. Aydemir and T. Akin, "Prevention of sidewall redeposition of etched byproducts in the dry Au etch process," *J. Micromechanics Microengineering*, vol. 22, no. 7, p. 074004, 2012.

[97] Shi-Jin Ding, Hang Hu, Chunxiang Zhu, Sun Jung Kim, Xiongfei Yu, Ming-Fu Li, Byung Jin Cho, D. S. H. Chan, M. B. Yu, S. C. Rustagi, A. Chin, and Dim-Lee Kwong, "RF, DC, and reliability characteristics of ALD HfO/sub 2/-Al/sub 2/O/sub 3/ laminate MIM capacitors for Si RF IC applications," *IEEE Trans. Electron Devices*, vol. 51, no. 6, pp. 886–894, Jun. 2004.

[98] G. McKerricher, J. G. Perez, and A. Shamim, "Fully Inkjet Printed RF Inductors and Capacitors Using Polymer Dielectric and Silver Conductive Ink With Through Vias," *IEEE Trans. Electron Devices*, vol. 62, no. 3, pp. 1002–1009, Mar. 2015.

[99] C. Bowick, J. Blyler, and C. J. Ajluni, *RF circuit design*, 2nd ed. Amsterdam ; Boston, 2008.

[100] H.-Y. Tseng, B. Purushothaman, J. Anthony, and V. Subramanian, "High-speed organic transistors fabricated using a novel hybrid-printing technique," *Org. Electron.*, vol. 12, no. 7, pp. 1120–1125, Jul. 2011.

[101] S. C. Lim, S. H. Kim, J. B. Koo, J. H. Lee, C. H. Ku, Y. S. Yang, and T. Zyung, "Hysteresis of pentacene thin-film transistors and inverters with cross-linked poly(4-vinylphenol) gate dielectrics," *Appl. Phys. Lett.*, vol. 90, no. 17, p. 173512, 2007.

[102] M. Hummelgård, R. Zhang, H.-E. Nilsson, and H. Olin, "Electrical Sintering of Silver Nanoparticle Ink Studied by In-Situ TEM Probing," *PLoS ONE*, vol. 6, no. 2, p. e17209, Feb. 2011.

[103] S. Iijima and P. M. Ajayan, "Substrate and size effects on the coalescence of small particles," *J. Appl. Phys.*, vol. 70, no. 9, p. 5138, Jul. 1991.

[104] T. Falat, J. Felba, A. Moscicki, and J. Borecki, "Nano-silver inkjet printed interconnections through the microvias for flexible electronics," 2011, pp. 473–477.

[105] J. Rogers, *Radio frequency integrated circuit design*. Boston: Artech House, 2003.

[106] X. Z. Xiong and V. F. Fusco, "A comparison study of EM and physical equivalent circuit modeling for MIM CMOS capacitors," *Microw. Opt. Technol. Lett.*, vol. 34, no. 3, pp. 177–181, Aug. 2002.

[107] L. Wang, R.-M. Xu, and B. Yan, "MIM Capacitor Simple Scalable Model Determination for MMIC Applications on GaAs," *Prog. Electromagn. Res.*, vol. 66, pp. 173–178, 2006.

[108] K. Okada and K. Masu, "Modeling of Spiral Inductors," in *Advanced Microwave Circuits and Systems*, V. Zhurbenko, Ed. InTech, 2010.

[109] B. S. Cook, Y. Fang, K. Sangkil, T. Le, B. Goodwin, K. Sandhage, and M. Tentzeris, "Inkjet Catalyst Printing and Electroless Copper Deposisiton for Low-Cost Patterned Microwave Passive Devices on Paper," *Electron. Mater. Lett.*, vol. 0, no. 0, pp. 1–8, Feb. 2013.

[110] Stratays, "Material Saftey Data Sheet -Objet Vero White Plus RGD835." Stratasys, Jul-2014.

[111]   Stratasys, "Polyjet material specifications - Vero white plus." Stratasys, Jul-2014.

[112]   M. Wubbenhorst, C. A. Murray, J. A. Forrest, and J. R. Dutcher, "Dielectric relaxations in ultra-thin films of PMMA: assessing the length scale of cooperativity in the dynamic glass transition," in *11th International Symposium on Electrets, 2002. ISE 11. Proceedings*, 2002, pp. 401–406.

[113]   Y. Dong, X. Li, S. Liu, Q. Zhu, J.-G. Li, and X. Sun, "Facile synthesis of high silver content MOD ink by using silver oxalate precursor for inkjet printing applications," *Thin Solid Films*, vol. 589, pp. 381–387, Aug. 2015.

[114]   C. M. Hong and S. Wagner, "Inkjet printed copper source/drain metallization for amorphous silicon thin-film transistors," *IEEE Electron Device Lett.*, vol. 21, no. 8, pp. 384–386, Aug. 2000.

[115]   J. Perelaer, C. E. Hendriks, A. W. M. de Laat, and U. S. Schubert, "One-step inkjet printing of conductive silver tracks on polymer substrates," *Nanotechnology*, vol. 20, no. 16, p. 165303, Apr. 2009.

[116]   W. Ahmad, D. Budimir, A. Maric, and N. Ivanisevic, "Inkjet printed bandpass filters and filtennas using silver nanoparticle ink on flexible substrate," in *2015 IEEE International Symposium on Antennas and Propagation USNC/URSI National Radio Science Meeting*, 2015, pp. 145–146.

[117]   E. Arabi, G. McKerricher, and A. Shamim, "Comparison of filters: Inkjet printed on PEN substrate versus a laser-etched on LCP substrate," presented at the IEEE European Conference of Antennas and PropagationEuCAP, Rome Italy, 2014, pp. 1226–1229.

[118]   A. Sridhar, J. Reiding, H. Adelaar, F. Achterhoek, D. J. van Dijk, and R. Akkerman, "Inkjet-printing- and electroless-plating- based fabrication of RF circuit structures on high-frequency substrates," *J. Micromechanics Microengineering*, vol. 19, no. 8, p. 085020, Aug. 2009.

[119]   D. Sette, A. Blayo, C. Poulain, and D. Mercier, "Silver nanoparticle inkjet printed 17 GHz filter," in *Microwave Symposium Digest (IMS), 2013 IEEE MTT-S International*, 2013, pp. 1–4.

[120]   C. Sriprachuabwong, C. Srichan, T. Lomas, and A. Tuantranont, "Simple RC low pass filter circuit fabricated by unmodified desktop inkjet printer," in *2010 International Conference on Electrical Engineering/Electronics Computer Telecommunications and Information Technology (ECTI-CON)*, 2010, pp. 929–932.

[121]   S. Butterworth, "On the Theory of Filter Amplifiers," *Exp. Wirel. Wirel. Eng.*, vol. 7, pp. 536–541, 1930.

[122]   B. S. Cook, C. Mariotti, J. R. Cooper, D. Revier, B. K. Tehrani, L. Aluigi, L. Roselli, and M. M. Tentzeris, "Inkjet-printed, vertically-integrated, high-performance inductors and transformers on flexible LCP substrate," 2014, pp. 1–4.

[123]   L. M. Galantucci, F. Lavecchia, and G. Percoco, "Experimental study aiming to enhance the surface finish of fused deposition modeled parts," *CIRP Ann. - Manuf. Technol.*, vol. 58, no. 1, pp. 189–192, Jan. 2009.

[124]   S. I. Latif and L. Shafai, "Pattern Equalization of Circular Patch Antennas Using Different Substrate Permittivities and Ground Plane Sizes," *IEEE Trans. Antennas Propag.*, vol. 59, no. 10, pp. 3502–3511, Oct. 2011.

[125]   E. Tekin, B.-J. de Gans, and U. S. Schubert, "Ink-jet printing of polymers – from single dots to thin film libraries," *J. Mater. Chem.*, vol. 14, no. 17, pp. 2627–2632, Aug. 2004.

APPENDIX 1 – Surface Tension Lookup Table

Look up table of S vs 1/H values directly from Andreas et al, original 1938 paper. For example S of 0.75 would correspond to 1/H of 0.785.

TABLE 1

Arithmetic tabulation of H-S function for pendant drops

$$S = \frac{d_s}{d_e} \qquad S \text{ vs. } 1/H \qquad \gamma = \frac{(\rho_1 - \rho_2)\, g d_e^2}{H}$$

Interpolation is unwarranted

S	0	1	2	3	4	5	6	7	8	9
0.70	0.797	0.795	0.792	0.790	0.787	0.785	0.782	0.780	0.777	0.775
0.71	0.772	0.770	0.767	0.765	0.762	0.759	0.757	0.754	0.752	0.749
0.72	0.747	0.744	0.742	0.739	0.737	0.735	0.732	0.730	0.727	0.725
0.73	0.722	0.720	0.718	0.715	0.713	0.711	0.709	0.706	0.704	0.702
0.74	0.699	0.697	0.695	0.692	0.690	0.688	0.685	0.683	0.681	0.679
0.75	0.676	0.674	0.672	0.670	0.668	0.665	0.663	0.661	0.659	0.657
0.76	0.655	0.652	0.650	0.648	0.646	0.644	0.642	0.640	0.637	0.635
0.77	0.633	0.631	0.629	0.627	0.625	0.623	0.621	0.619	0.617	0.615
0.78	0.613	0.611	0.609	0.607	0.605	0.603	0.601	0.599	0.597	0.595
0.79	0.593	0.591	0.589	0.587	0.585	0.583	0.581	0.579	0.577	0.575
0.80	0.573	0.571	0.570	0.568	0.566	0.564	0.562	0.561	0.559	0.557
0.81	0.555	0.553	0.551	0.550	0.548	0.546	0.544	0.542	0.540	0.539
0.82	0.537	0.535	0.533	0.532	0.530	0.528	0.526	0.524	0.523	0.521
0.83	0.519	0.518	0.516	0.515	0.513	0.511	0.509	0.507	0.506	0.504
0.84	0.502	0.501	0.499	0.498	0.496	0.494	0.493	0.491	0.490	0.488
0.85	0.486	0.485	0.483	0.482	0.480	0.479	0.477	0.476	0.474	0.473
0.86	0.471	0.470	0.468	0.467	0.465	0.464	0.462	0.461	0.459	0.458
0.87	0.457	0.455	0.454	0.452	0.451	0.450	0.448	0.447	0.446	0.444
0.88	0.443	0.441	0.440	0.439	0.437	0.436	0.434	0.433	0.431	0.430
0.89	0.429	0.428	0.426	0.425	0.423	0.422	0.420	0.419	0.418	0.417
0.90	0.415	0.414	0.413	0.411	0.410	0.409	0.408	0.406	0.405	0.404
0.91	0.403	0.401	0.400	0.399	0.398	0.396	0.395	0.394	0.393	0.391
0.92	0.390	0.389	0.388	0.386	0.385	0.384	0.383	0.382	0.381	0.379
0.93	0.378	0.377	0.376	0.375	0.373	0.372	0.371	0.370	0.369	0.368
0.94	0.366	0.365	0.364	0.363	0.362	0.361	0.359	0.358	0.357	0.356
0.95	0.355	0.354	0.353	0.352	0.351	0.350	0.349	0.348	0.346	0.345
0.96	0.344	0.343	0.342	0.341	0.340	0.339	0.338	0.337	0.335	0.334
0.97	0.333	0.332	0.331	0.330	0.329	0.328	0.327	0.326	0.325	0.324
0.98	0.323	0.322	0.321	0.320	0.319	0.318	0.317	0.316	0.315	0.314
0.99	0.313	0.312	0.311	0.310	0.309	0.308	0.307	0.306	0.305	0.304
1.00	0.303									

APPENDIX 2 – Fowkes method (example with PMMA)

The best way to understand Fowkes method is with an example, finding the surface free

energy of PMMA. As stated in the thesis, water, diiodomethane, and Teflon are used

because of their unique properties. Water having a high polar component, and

diiodomethane and Teflon having zero polar components.

Measurements: First step is to take the surface tension measurements of

Diiodomethane and water as described in Section 3.3.1. Next, the contact angle is

measured on Teflon in order to obtain the polar and dispersive forces of each fluid.

(Teflon is the known standard with 18 dynes of dispersive and zero polar energy). So far,

our knowns are tabulated below:

Teflon -Air (Known) γ_{SV}	Water-Air γ_{LV}	Diiodomethane-Air γ_{LV}	Water-Teflon θ_{Teflon}	Diiodomethane-Teflon θ_{Teflon}
18.0 Dyn/cm Dispersive only	72.8 Dyn/cm	50.8 Dyn/cm Dispersive Only	113.7°	79.0°

Now we can find the dispersive and polar components of the liquids using the following

equations from.[15]

$$\gamma_{LV}^{D} = \frac{(\gamma_{LV})^2 (\cos\theta_{Teflon} + 1)^2}{72}$$

$$\gamma_{LV}^{P} = \gamma_{LV} - \gamma_{LV}^{D}$$

Substituting the appropriate values in leads to:

---

[15] This method will work to find polar and dispersive components for any fluid just using the Teflon substrate and contact angle measurments.

Liquid	Contact Angle on Teflon	Dispersive γLV	Polar γLV
Diiodomethane	79	50.82520528	-0.025205284
Water	113.7	26.32743085	46.47256915

Now that the liquids are characterized the contact angle for PMMA (or any substrate) is measured. Which from Chapter 2 we have water at 75.6° and diiodomethane at 53.6°.

First step for Diiodomethane with no polar component the primary Fowkes equation is simplified to one unknown, the dispersive γSV.

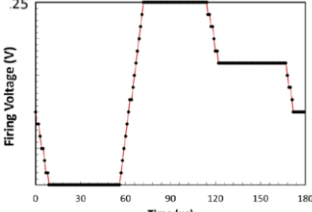$$(\gamma_{SV}^{D})^{\frac{1}{2}} = \frac{\gamma_{LV}(cos\theta + 1)^2}{4}$$

Second step, the water contact measurement can be substituted in the full primary Fowkes equation and solved for the remaining unknown, the polar γSV.

$$(\gamma_{LV}^{D})^{\frac{1}{2}}(\gamma_{SV}^{D})^{\frac{1}{2}} + (\gamma_{LV}^{P})^{\frac{1}{2}}(\gamma_{SV}^{P})^{\frac{1}{2}} = \frac{\gamma_{LV}(cos\,\theta + 1)}{2}$$
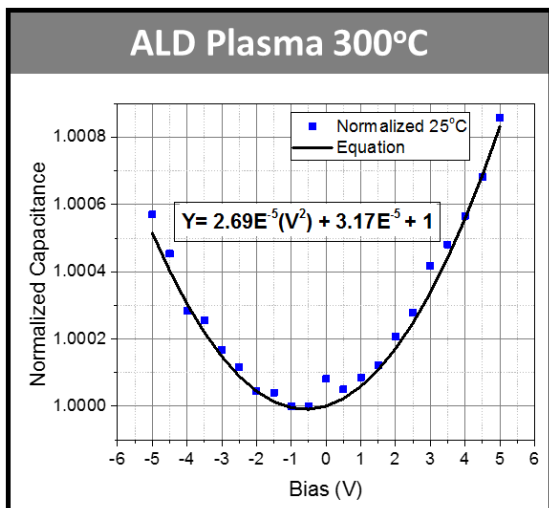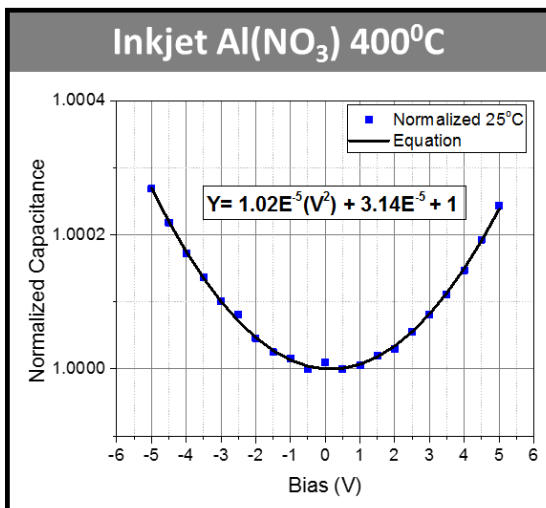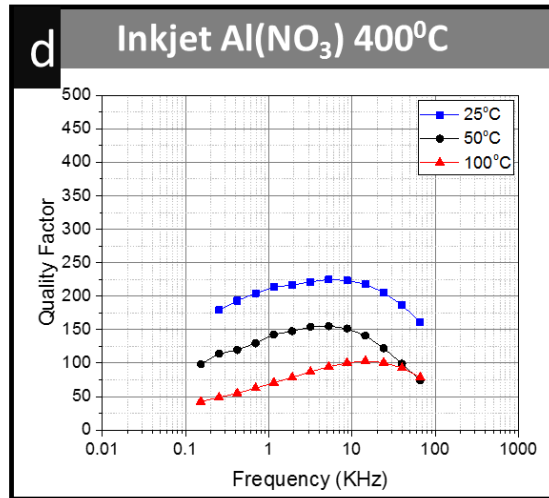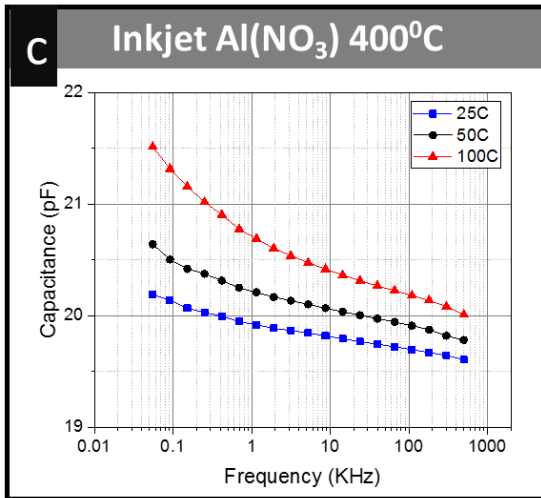
FIRST STEP	Diiodomethane	Dipersive γSV
PMMA	53.6°	32.2 Dyn/cm
SECOND STEP	Water	Polar γSV
PMMA	75.6°	5.7 Dyn/cm
PMMA Dispersive + Polar γSV		37.9 Dyn/cm

Finally we find the PMMA has 32.2 and 5.7 dyn/cm of dispersive and polar components and a total 37.9 Dyn/cm surface free energy.

APPENDIX 3 – Detailed RF MIM Inkjet Printing Fabrication Process

1 Cleaning	**2 Bilayer resist**	**3 Lift Off**
• Start with glass borofloat wafers from (university wafer) <1.5nm Ra • New wafers are cleaning in piranha solution for 10 minutes at 120°C	• Spin LOR7B at 1200 RPM Prebake 180°C. Cool for 2mins on metal, ~1.2 um. • Spin AZ1512 resist 3000 RPM prebake 100°C, ~1.4um. • Exposure UV broadband, no filter 40 mJ//cm^2 • Develop 45 sec AZ MIF 726	• Oxygen plasma for 150 sec at 80°C, 350W • Sputter at 1E^{-7} Torr, 400W Ti 60 sec ~10nm, 400W Au 630 sec • Acetone for 1 hour. Sonicate 2min. MIF 726 strips LOR, and 150 sec 950W O$_2$ plasma.

4 PVP Coating	**5 Sol-Gel Ink**	**6 Printing**
• Dilute 0.5% PVP (Sigma Aldrich 436216), dissolved in 1-hexanol. Spin at 5000 RPM 45 sec. Bake at 200°C hotplate for 10 mins. Cool, then 150 second UV ozone treatment	• Aluminum Nitrate (Sigma Aldrich 06275), dissolved in 50/50 2-ME and Ethanol. Vortex mixed for 30 minutes. Left for minimum 1 hour before use. Solution remains stable for several weeks.	• Dimatix printer with 10pL Cartridge. Cartridge at 30°C, 40°C substrate temp. 55 drop spacing, vacuum is on, 5KHz frequency. Drop mass is 7ng.

7 Printing waveform	**8 Heating**	**9 Amorphous Si (1)**
	• After printing each layer, Hot plate at 70°C 5 min, 90°C 5min, then ramp 200°C to 400°C at 10°C/min for 10mins. UV Ozone for 150seconds. Final layer is printed and the 400°C anneal for 2 hours.	• Dehydration bake, 180°C for 5 min, Spin AZ ECI 3027 at 1750 RPM 40sec, prebake 100° C for 60 sec. ~4um thick • Expose 180mJ/cm^2 and develop 60 sec in AZ developer (for Aluminum). Oxygen plasma 350W 150 sec

10 Amorphous Si (2)	**11 Seed Layer and Electroplate**	**12 Seed Layer & α-Si Etch**
• Deposit Amorphous Si, 47 cycles, at 50°C ~ 1.8um • Acetone 1 hour, Rinse off. Can do light sonication <2min • Oxygen plasma 350W 150sec	• Sputter Deposit 10nm of Ti and 250nm of Au, 400W 300 sec. • Spin photoresist AZ ECI 3027 (same steps as 9.) • Electroplate copper at 25°C with 0.5mA and 0.5V setting until 3.5 um is reached.	• Strip resist in acetone, and oxygen plasma 350W 150 sec. Argon plasma at 100W Fwd 800W (Argon 30sccm) at 10°C platen. 3 minutes. • Then XeF2 etch room temp α-Si for 50 cycles, at 30 sec each.

APPENDIX 4 - Comparison of Sol-Gel Inkjet Alumina and ALD Alumina

a ALD Plasma 300°C

b ALD Plasma 300°C

c Inkjet Al(NO$_3$) 400^{0}C

d Inkjet Al(NO$_3$) 400^{0}C

Inkjet Al(NO$_3$) 400^{0}C

$$Y= 1.02E^{-5}(V^2) + 3.14E^{-5} + 1$$

ALD Plasma 300°C

$$Y= 2.69E^{-5}(V^2) + 3.17E^{-5} + 1$$
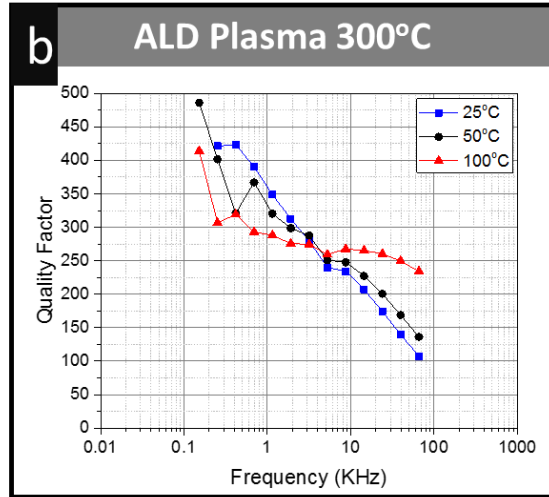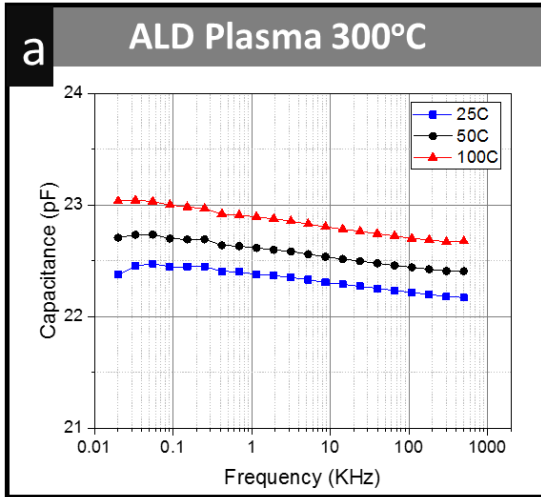
APPENDIX 6 – Silver-Organo-Complex Ink Preparation

In an illustrative experiment, a 2M ethylamine solution in methanol, which was called as

"Complexing Solution #1" was put in a vial. 10 mL of ethanolamine and 10 mL of

deionized (DI) water (1:1 ratio) was mixed in another a vial. Formic acid was then added

to the solution in a drop-wise manner to adjust the solution to pH 10.5. The resulting

solution was called "Complexing Solution #2". In another vial, 1g of silver acetate was

vortex mixed with 2 mL of complexing solution #1, 1.5 mL of complexing solution #2, and

0.5 mL of 2% 2-hydroxyethyl cellulose (M_v ~90,000) (2% 2-HEC in water:methanol) at

room-temperature for 30 seconds, resulting in a light black colored solution. The as-

obtained solution was then kept for twelve hours to allow any particles to settle out,

yielding a clear supernatant, which was decanted and filtered through a 200 nm syringe

filter. This clear and transparent solution that contains approximately ~17 wt% silver,

served as the silver-ethylamine-ethanolamine-formate complex based SOC ink.